Process and materials science aspects for the development of hard coatings for cutting tools

Dipl.-Ing. Thomas Weirather

being a thesis in partial fulfilment of the requirements for the degree of a

Doctor of Montanistic Sciences (Dr. mont.)

at the Montanuniversität Leoben

Leoben, October 2013

This work was done within the Research Studios Austria Surface Engineering and energy-drive, with financial support from the Österreichische Forschungsförderungsgesellschaft and the Bundesministerium für Wirtschaft, Familie und Jugend.

Affidavit

I declare in lieu of oath, that I wrote this thesis and performed the associated research myself, using only literature cited in this volume.

Leoben, October 2013

Thomas Weirather

Acknowledgments

My sincerest gratitude is due to my supervisor Prof. Dr. Christian Mitterer, head of the chair of Functional Materials and Materials Systems. I highly appreciate his confidence in me, his advice, guidance and what I could learn from him during my seven years in his Thin Film Group.

Furthermore, I would like to sincerely thank Prof. Dr. Jozef Keckes for co-supervising this thesis.

I would also like to thank Prof. Dr. Helmut Clemens, head of the Department Physical Metallurgy and Materials testing, for my time at his Department. Special thanks to Hilde, Regina and Angelika for their amicable administrative cooperation as well as Alfons, Bruno, Felix, Gerhard and Silvia for their support.

I want to express my gratitude to Alexander Fian and Bernhard Sartory for the fruitful cooperation, which yielded valuable results for this thesis.

Besides, I want to thank my past and present colleagues in the Thin Film Group, the Substrate Group and the Materials Center Leoben. Special thanks to Anna, Birgit, Boryana, Chris, David, Gerardo, Hannes, Kerstin, Marisa, Martin, Manfred, Michael, Nina, Oli, Paul, Richi, Robert, Rosti, Saty, Soumya, Stephan and Veli for vital discussions, support and especially their friendship.

Representative for my friends at home and in Leoben, I want to express my sincere gratitude to Markus Pohler, who supported me in various matters especially during my twelve years in Leoben.

My deepest thankfulness is due to my family, my parents Irene and Reinhard, my sister Lisa and my grandmother Antonia, for their endless support, their encouragement and their love through a long time quite far away from home. Sadly, I dedicate this thesis to my grandfather Werner, who passed away in the time of its final preparation.

Last but not least, I want to express my sincerest gratefulness to Eugenia, the most important person in my life. I would not have been able to finish this work without her love, her daily support, patience and encouragement. *Я тебя́ люблю́!*

Contents

1. Introduction

Both economical and ecological significance have provoked extensive research and development effort over the last decades to steadily extend the service life of high performance cutting tools at ever increasing cutting speeds and therefore mechanical and thermal loads [1-3]. The application of highly developed tool materials as well as advanced hard and wear resistant coatings is essential to meet the machining industry's challenging demands.

Commonly, tool materials like high-speed steels (HSS) and cemented carbides are employed for machining applications [1,4]. However, advanced production standards recently enabled the market launch of Fe-25%Co-15%Mo, which was described in literature as an auspicious cutting tool material already in the early 1930s [5,6]. Though, the remaining drawback of Fe-25%Co-15%Mo is that only a poor hard coating adhesion is achievable applying conventional deposition processes due to its untypical microstructure.

Reactive magnetron sputtering is a well accepted means for hard coating deposition [7]. Reliable process control [8] and comprehensive knowledge on both sputtering and thin film growth mechanisms [9-12] furthermore enable interface engineering. The combination of plasma-assisted nitriding and coating deposition in duplex processes, as an example, was shown to beneficially affect the coating adhesion as well as the wear performance [13-15].

$Ti_{1-x}Al_xN$ and $Cr_{1-x}Al_xN$ are prominent hard coating materials for cutting tools [1,16,17]. The substitutional incorporation of Al in TiN and CrN yields metastable solid solutions with significantly enhanced mechanical properties, wear and oxidation resistance [18,19]. While $Cr_{1-x}Al_xN$ exhibits a higher oxidation resistance, $Ti_{1-x}Al_xN$ features a higher hardness combined with self-adaptive age-hardening at elevated temperatures due to spinodal decomposition [20-22]. The steadily growing knowledge on the mechanisms behind enables further optimisation of the coating's response to the high mechanical and thermal loads during service. Multilayered coating structures of $Ti_{1-x}Al_xN$ and TiN, as an example, have proven to enhance the mechanical properties and the thermal stability, resulting in increased cutting performance [23-25]. However, investigations on the influence of increased coating deposition temperatures are lacking.

The properties of $Ti_{1-x}Al_xN$ and $Cr_{1-x}Al_xN$ strongly scale with their AlN content, while both have individual deposition process dependent solubility limits [26]. Consequently, it is immensely time and money consuming to study their structure-property evolution over wide compositional ranges, especially using industrial-scale sputtering systems. Applying conventional sputter targets with a fixed composition, numerous deposition runs are required to get a punctual overview of the arising coating performance [19,27-29].

The present thesis demonstrates selected process and materials science aspects for the development of high performance hard coatings for cutting tools. It is shown that the design of a duplex process implementing plasma-assisted nitriding of Fe-25%Co-15%Mo prior to $Ti_{1-x}Al_xN$ coating deposition significantly enhances the obtainable coating adhesion and, consequently, the wear performance. Furthermore, the beneficial effects of increased substrate temperatures during $Ti_{1-x}Al_xN$/TiN multilayer coating deposition on mechanical properties and thermal stability are highlighted and corroborated with cutting tests. Finally, novel triangle-like segmented targets are presented as an auspicious tool for more efficient and economic coating material development.

2. Tool materials

Cutting tools are subjected to notedly heavy loads during service. Consequently, the applied tool materials, typically high-speed steels or cemented carbides [30], need to exhibit outstanding mechanical properties with respect to hardness, toughness and wear resistance [31]. Furthermore, substantial hot hardness and thermal stability are indispensable [32,33], as high temperatures in the range of 300-1300 °C [1,30] arise at the cutting edge during service. Although the application of hard coatings on cutting tools is known to significantly enhance the wear resistance [32], the choice of an adequate tool material is essential for their performance. Therefore, the characteristics of the materials relevant for this thesis are briefly outlined in this chapter.

2.1 High-speed steels

High-speed steels (HSS) are high-alloyed steels with W, Mo, V, Cr and Co as the main alloying elements [33,34]. Their microstructure consists of primary and secondary hardening carbides embedded in a martensitic matrix [35], giving rise to moderate toughness despite the high achievable hardness of up to 65 HRC after tempering [33]. The main drawbacks of HSS are their limited hot hardness and thermal stability, which can mainly be influenced by the Co content [36,37]. Still, due to their significantly higher toughness compared to cemented carbides, HSS are frequently used as tool materials [38]. Applying powder-metallurgical production routes to produce PM-HSS enhances the mechanical properties with hardness values of almost 70 HRC, and the thermal stability can be increased up to ~560 °C [33,39].

2.2 Cemented carbides

Cemented carbides, which are generally produced via powder-metallurgical routes including sintering at 1300-1600 °C, typically exhibit a microstructure of WC grains embedded in a Co binder phase [40]. The addition of TiC, TaC and/or NbC allows for tuning of the mechanical properties and the thermal stability, while the Co content (typically 5-30 wt.%) determines the limited achievable toughness [33]. Apart from that, cemented carbides offer outstanding hardness, strength and wear resistance compared to HSS as well as thermal stability up to ~1300 °C. Cemented carbides are therefore frequently used as cutting inserts, which are clamped on a tool holder of higher toughness [33,40,41].

2.3 Fe-25%Co-15%Mo

Fe-25%Co-15%Mo is a novel powder-metallurgical tool material, which comprises higher toughness compared to cemented carbides with enhanced strength, abrasion resistance and thermal stability compared to HSS [42]. Its carbide-free microstructure is strengthened by primary and secondary intermetallic μ-phase $(Fe,Co)_7Mo_6$ precipitates, which are formed in a Fe-Co martensite matrix during tempering [43]. The precipitation hardening behaviour of Fe-25%Co-15%Mo, which is comparable to that of Al-alloys, was examined in detail by Leitner et al. [44]. Hardness values of up to 70 HRC are achievable, combined with a significantly increased hot hardness compared to HSS [5,42,45,46]. Apart from the outstanding properties of Fe-25%Co-15%Mo, making it a promising candidate for precision tool manufacturing, its main drawback is that the deposition of hard coatings with adequate adhesion is challenging.

3. Coating deposition

Hard coatings are frequently synthesized via physical vapour deposition (PVD) techniques, which comprise three basic steps: (i) Formation of vapour phase, (ii) transport of the vapour to the substrate and (iii) condensation, nucleation and film growth [4,47]. The vapour phase formation is mainly achieved by arc evaporation or sputtering [48]. The latter will be explained in more detail, as it was applied for the coating depositions throughout this thesis.

Sputter deposition is based on the ejection of film forming atoms from the surface of a solid source, i.e. the sputter target, by energy and momentum transfer from impinging ions generated in a plasma [47,49], as illustrated in Fig. 1. Ejection occurs when a surface atom experiences a displacement energy higher than the surface binding energy, typically through collision cascades evolving in the upmost atomic layers of the target [9,50].

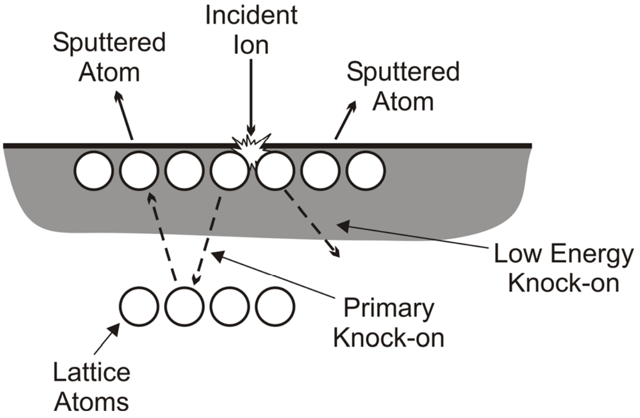

Fig. 1: Illustration of the sputtering process as a consequence of energy and momentum transfer from an incident energetic ion [49].

The sputtering plasma is achieved by applying a negative potential to the cathode with the target mounted on it, while an inert working gas, mostly Ar, is introduced to the deposition chamber under high vacuum conditions [47,49]. For enhanced plasma density and therefore sputter efficiency, magnetron cathodes are commonly applied [49]. Nitrides and oxides, which are typical hard coating materials [33], are usually synthesized via reactive magnetron sputtering. Thereby, a reactive gas (N_2 or O_2) is added to the working gas, resulting in compound formation with the sputtered material [50]. To attract ion bombardment of the growing film for densification and enhanced growth energetics, a low negative bias potential is mostly applied to the substrate holder [10].

The industrial-scale sputter deposition systems applied in this work (CemeCon CC800/9® type ML or MLT, cf. [51] for a schematic) feature four magnetrons operated either in conventional direct current (DC) or in dual pulsed mode [8,47]. The substrates are mounted on a rotating carrousel, where a DC or a mid-frequency pulsed DC bias voltage can be applied. During the utilized deposition processes, substrate pre-cleaning prior to coating deposition is achieved through a heating step and subsequent Ar^+ ion etching, obtained by igniting a plasma with the substrate holder being on a negative potential. The ion etching intensity can be enhanced activating so-called plasma boosters. Smooth plasma-nitriding conditions are achievable by adding N_2 to the working gas Ar, similar as during reactive sputtering in the final coating deposition step [52]. There, the arrangement of the four magnetron cathodes in the deposition chamber combined with the applied substrate rotation enables the deposition of multilayer coatings if sputter targets of different materials or compositions are used.

4. Thin film growth

When vapour phase species, produced by sputtering of the target(s) or introduced as reactive gas, impinge on a substrate surface, they either are reflected or transfer kinetic energy to the substrate lattice to become loosely bonded as adatoms. These adatoms diffuse over the substrate surface until they are desorbed, e.g. by re-sputtering, they reach other adatoms to form a stable nucleus or they attach to already existing nuclei [48,49]. Growth of these nuclei, which preferentially form at low-energy sites like scratches, lattice steps or defects, subsequently yields coalescence with neighbouring nuclei until a continuous thin film evolves [50].

The nucleation stage is of crucial importance to obtain a strong adhesion of the coating to the substrate, which is probably the most important prerequisite for coated cutting tools. The mobility of the adatoms on the substrate surface, which is determined by their kinetic energy, the substrate temperature and the intensity of interactions between the adatoms and the substrate, needs to be sufficiently high that low-energy sites can be reached, yielding a high nucleation density [10,48,50]. Moreover, the interfacial energy between the coating nuclei and the substrate material should generally be low to obtain the required coating adhesion, according to evident energetic considerations [50]. Hultman et al. [12] demonstrated that the adhesion of TiN coatings on HSS is highly influenced by epitaxial relationships between $VC_{0.8}$ in the substrates and the growing film, resulting in coherent low-energy interfaces. Similarly, Vuorinen and Hoel [53] revealed local epitaxial growth of TiC coatings on WC grains in cemented carbide substrates. However, due to its exceptional microstructure [43,44], no comparable epitaxial relations with common hard coating materials can be anticipated.

Thin film growth subsequent to the nucleation phase is differentiated in three basic modes [10,50], as illustrated in Fig. 2: (i) Island or Volmer-Weber growth appears when the film forming atoms are more strongly bound to each other than to the substrate. (ii) Layer-by-layer or Frank-van der Merwe growth occurs when the deposited atoms are more strongly bound to the substrate than to each other. (iii) Mixed layer-island or Stranski-Krastanov growth arises when island growth becomes favourable after the initial development of one or several monolayers.

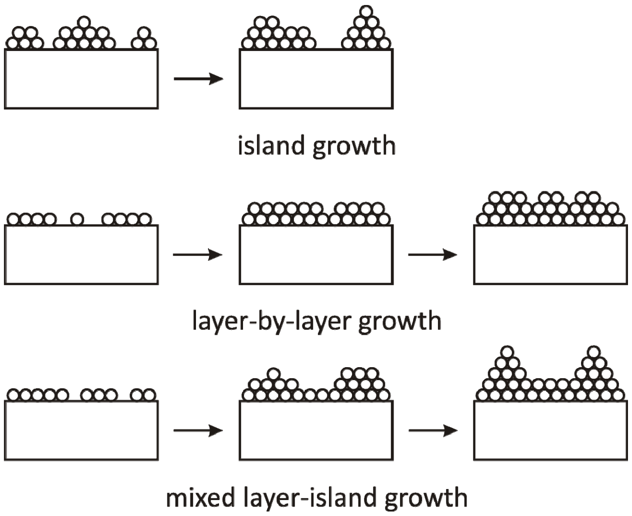

Fig. 2: Schematics of the basic thin film growth modes: Island, layer-by-layer and mixed layer-island growth [50].

The evolving thin film microstructure and therefore the coating properties strongly depend on the adatom mobility. Diffusion is needed to compensate for the so-called shadowing effect, which is caused by the high directionality of the vapour species flux arriving at the substrate [50]. As the diffusivity scales with the melting temperature T_m, it is commonly described in terms of the homologous growth temperature, i.e. T_S/T_m, where T_S denotes the substrate temperature. Accordingly, Movchan and Demchishin proposed the first structure zone model (SZM), in which they linked the microstructure of thick coatings grown by thermal evaporation with T_S/T_m, defining three characteristic zones [54]. Thornton extended this SZM for electron beam evaporated and sputtered metal coatings, additionally considering the Ar pressure in the deposition chamber, which influences the kinetic energy of the impinging vapour species and, therefore, the adatom mobility [55]. Messier modified Thornton’s SZM by replacing the gas pressure with the substrate bias voltage to account for ion irradiation induced growth energetics enhancement [56]. In both Thornton’s and Messier’s SZMs, a transition zone T is introduced between the zones 1 and 2.

Zone 1 is characterized by fibrous crystallites with voided boundaries, dominated by shadowing effects due to insufficient adatom mobility. In zone T, moderate adatom surface diffusion yields a dense-packed microstructure through competitive growth of neighbouring crystallites. Consequently, initially V-shaped crystals develop to a columnar structure with increasing film thickness. The dense zone 2 microstructure arises when surface diffusion becomes dominant, leading to uniform columnar grains. The columns, whose diameters increase with increasing T_S/T_m, typically expand throughout the whole coating thickness. In zone 3, bulk diffusion enables the formation of equiaxed recrystallized grains [11,49,50,57].

Barna and Adamik constructed a SZM for real polycrystalline films, taking the segregation of impurities and co-deposited species into account, which may promote or inhibit basic structure forming phenomena [11]. Furthermore, as illustrated in Fig. 3, Anders recently extended Thornton's SZM to account for higher energetic thin film deposition including the increased ion flux using modern technologies [58]. Accordingly, T_S/T_m was replaced by the generalized temperature T*, which additionally considers the potential energy of arriving particles. The Ar pressure was exchanged to the logarithmically plotted normalized energy E*, describing displacement and heating effects caused by the kinetic energy of impinging species. The net film thickness t* is plotted on the up to now unlabeled third axis to qualitatively indicate coating densification, sputtering or even negative film thickness, which is obtainable by ion etching. In Fig. 3, two inaccessible regions can be identified. On one hand, E* can not be arbitrarily low as the ions need to have a certain energy to reach the substrate surface, and on the other hand, T* can not be arbitrarily low when E* is high.

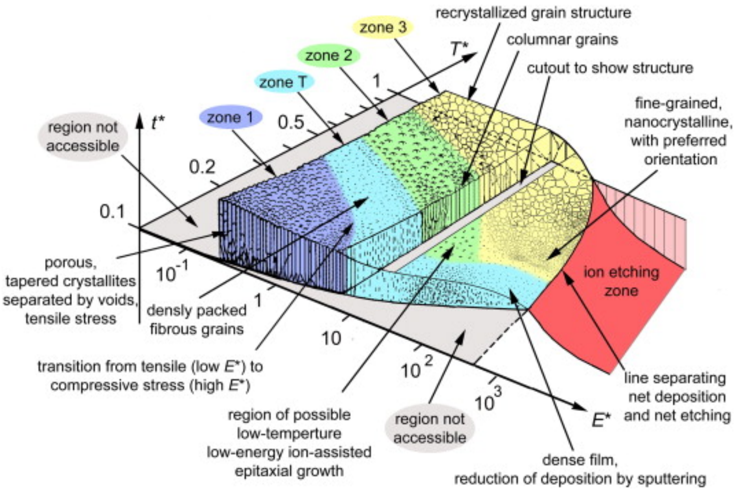

Fig. 3: Structure zone model for energetic thin film growth proposed by Anders [58].

5. Hard coating materials

5.1 $Ti_{1-x}Al_xN$

$Ti_{1-x}Al_xN$ was introduced almost three decades ago as a promising alternative to TiN as hard coating material for cutting tools [59,60]. Although TiN and AlN are practically immiscible in thermodynamical equilibrium, non-equilibrium PVD methods enable the synthesis of metastable supersaturated $Ti_{1-x}Al_xN$ solid solutions of virtually any composition [18,61,62]. The structural development of $Ti_{1-x}Al_xN$ with increasing AlN content x is illustrated in Fig. 4. Based on face-centered cubic (fcc) TiN, fcc $Ti_{1-x}Al_xN$ is formed by substitution of Ti by Al atoms on the metal sublattice, up to an AlN content of $x \approx 0.65$ [26]. After a dual phase transition zone, even higher AlN contents lead to the detrimental formation of its thermodynamically stable wurtzite structure, where the remaining Ti substitutes for Al.

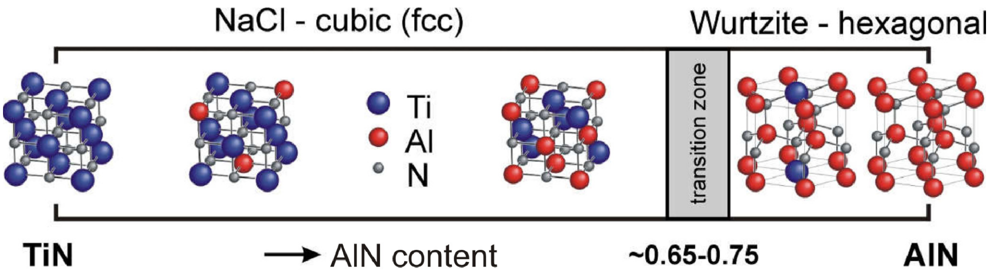

Fig. 4: Structural evolution of $Ti_{1-x}Al_xN$ with increasing AlN content x (adapted from [19]).

The desired properties for high-performance cutting applications are obtained within the single phase fcc regime, where increasing AlN contents yield increased mechanical properties and wear resistance [63]. The latter can in part be attributed to an enhanced oxidation resistance due to the formation of a stable protective Al_2O_3 layer at the coating surface [64]. Furthermore, $Ti_{1-x}Al_xN$ undergoes self-adaptive age-hardening at elevated temperatures (≥ 800 °C), e.g. during tool service, as a consequence of spinodal decomposition into TiN- and AlN-rich domains [22,65,66]. The reason for this can be found in large positive values of the isostructural mixing enthalpy and a negative second derivative of the Gibbs free energy curve [67,68]. However, the resulting coherency strains yield retained and even increased hardness, before the fcc AlN-rich domains transform into wurtzite AlN and the coating properties deteriorate [22,63].

The thermal stability of $Ti_{1-x}Al_xN$ with respect to both spinodal decomposition and wurtzite AlN formation has therefore attracted extensive research over the last decade [63,65,68-70]. As the underlying mechanisms are widely understood [22,66,67,71-74], the aim is to promote the beneficial age-hardening effect due to isostructural decomposition, while suppressing the detrimental wurtzite AlN formation [23].

A well accepted approach to tailor the thermal response of $Ti_{1-x}Al_xN$ is alloying, e.g. with Si, Cr, Zr, Hf or Ta (14-19). Schalk et al. [74] studied the influence of residual stresses and grain size on the spinodal decomposition behaviour. Furthermore, enhanced mechanical properties along with retained formation of wurtzite AlN were demonstrated for multilayered coating structures of $Ti_{1-x}Al_xN$ and TiN [23-25,75,76]. The enhanced mechanical properties in the as-deposited state are a consequence of strengthening due to coherency strains, i.e. the Koehler effect [77,78]. Additionally, the isostructural decomposition at elevated temperatures is facilitated at the abundant internal interfaces [76]. Coherency strains finally hinder the transformation to wurtzite AlN, which is accompanied by a unit cell volume increase of ~20% [79-81]. However, comprehensive investigations on the influence of the substrate temperature, which will be crucial for the evolving coating microstructure according to the SZMs, are lacking. Although substrate materials with auspicious hot hardness are employed (or at least available), coating deposition temperatures are commonly limited in the range of 300-500 °C [23,24,63,66,70,73,75,76].

5.2 $Cr_{1-x}Al_xN$

$Cr_{1-x}Al_xN$ was developed around 1990, inspired by the outstanding properties of $Ti_{1-x}Al_xN$ [20], and became its probably most prominent competitor as hard coating material for cutting tools [16]. This can mainly be attributed to the higher metastable solubility for AlN in fcc $Cr_{1-x}Al_xN$ ($x \approx 0.77$) [26], while the structural evolution with increasing AlN content is qualitatively in accordance with that of $Ti_{1-x}Al_xN$ depicted in Fig. 4 [19]. According to Rovere et al. [72], the increased AlN solubility in the fcc structure can be attributed to the higher valence electron concentration of Cr compared to Ti. As both Cr and Al form stable protective oxide scales at the coating surface, $Cr_{1-x}Al_xN$ exhibits superior oxidation resistance compared to $Ti_{1-x}Al_xN$, [20,82]. However, a drawback of $Cr_{1-x}Al_xN$ can be found in its lower hardness [21]. Moreover, although Willmann et al. [83] observed a slight initial hardness increase in high AlN containing $Cr_{1-x}Al_xN$ at ~700 °C as a result of wurtzite AlN formation, no age-hardening based on isostructural decomposition can be expected. This is due to the facts that $Cr_{1-x}Al_xN$, like CrN, is subjected to dissociative N-loss at elevated temperatures [84,85], and that it has a lower driving force for spinodal decomposition compared to $Ti_{1-x}Al_xN$. Consequently, N-loss occurs before isostructural decomposition processes can initiate, giving rise to nucleation and growth of wurtzite AlN without the intermediate formation of fcc AlN-rich domains [72].

6. Summary and conclusions

Selected process and materials science aspects for the development of advanced hard coatings for cutting tools are highlighted in the present thesis. As a proper hard coating adhesion is crucial for the wear performance, interface engineering was performed to foster local epitaxial growth of $Ti_{1-x}Al_xN$ on Fe-25%Co-15%Mo, which is an auspicious novel tool material. Furthermore, the beneficial influence of increased deposition temperatures on structure, properties, thermal stability and wear resistance of multilayered $Ti_{1-x}Al_xN$/TiN coatings was investigated in detail. Moreover, newly developed triangle-like segmented sputter targets and their high potential to distinctly reduce the workload in coating material development were presented.

Plasma-assisted nitriding during sputter etching of Fe-25%Co-15%Mo yielded the formation of cubic Mo_2N in the topmost few nanometres of the substrate surface, resulting in a significantly increased adhesion strength of the subsequently deposited $Ti_{1-x}Al_xN$ coatings. The coating crystallinity increased with increasing nitriding time, while a change in preferred orientation from (111) to (110) was observed. Tribological tests revealed a high potential of duplex $Ti_{1-x}Al_xN$ coated Fe-25%Co-15%Mo for severe cutting applications especially after shorter nitriding pre-treatments.

Increasing the substrate temperature during sputter deposition of $Ti_{1-x}Al_xN$/TiN multilayer coatings from 375 to 575 °C resulted in a higher coating thickness along with a preferred (111) orientation. In the as-deposited state, the formation of sharper layer interfaces and domain boundaries at the highest substrate temperature yielded enhanced mechanical properties in spite of distinctly rising domain sizes. Vacuum annealing experiments revealed a by 50 °C retarded onset of the detrimental wurtzite AlN formation subsequent to spinodal decomposition. Tribological investigations, where special emphasis was also laid on the hot hardness of the coated powder-metallurgical high-speed steel substrates, indicated significantly increased wear resistance. The superior coating performance was furthermore corroborated in cutting tests, where an enhancement in tool lifetime of about 40% was demonstrated.

The application of triangle-like segmented sputter targets enabled the synthesis of $Cr_{1-x}Al_xN$ coatings with $0.21 \leq x \leq 0.74$ at a high compositional resolution within two deposition runs. The obtained coating compositions were supported with sputtering simulations, and the metastable AlN solubility limit in cubic $Cr_{1-x}Al_xN$ was detected at $x = 0.61$ for the chosen process parameters. Tribological test revealed excellent performance of the $Cr_{1-x}Al_xN$ coatings with low friction down to $\mu \approx 0.4$ and outstanding wear resistance. Consequently, the presented approach was proven as an auspicious tool for efficient coating material development.

As a matter of course, remaining open points for future work can be identified. Based on the results of this thesis, it would be of great interest to combine the enhanced properties of $Ti_{1-x}Al_xN$/TiN multilayer coatings deposited at high substrate temperatures with an exceptional substrate material like Fe-25%Co-15%Mo. A duplex process with relatively short nitriding pre-treatment should be applied, while the substrate temperature during deposition of the multilayered $Ti_{1-x}Al_xN$/TiN coating should further be increased to 600-650 °C. Investigations on the formed substrate-to-coating interface at the atomic scale, e.g. via atom probe tomography, would additionally yield valuable insights for further optimization of the coating system. Additionally, it would be inviting to apply segmented targets to explore hardly known coating materials, like e.g. $Ti_{1-x}Cr_xN$ or $Cr_{1-x}Ta_xN$.

7. References

[1] S. PalDey, S.C. Deevi, Mater. Sci. Eng. A 342 (1-2) (2003) 58.

[2] M. Kathrein, C. Michotte, M. Penoy, P. Polcik, C. Mitterer, Surf. Coat. Technol. 200 (5-6) (2005) 1867.

[3] W. Kalss, A. Reiter, V. Derflinger, C. Gey, J.L. Endrino, Int. J. Refract. Met. Hard Mater. 24 (5) (2006) 399.

[4] R.F. Bunshah, in: R. F. Bunshah (Ed.), *Deposition Technologies for Films and Coatings: Developments and Applications*, Noyes Publications, Park Ridge, NJ, 1982, pp. 1-18.

[5] W. Köster, Arch. Eisenhüttenwes. 1 (1932) 17.

[6] Y.A. Geller, V.V. Afanasyev, *Tool Steels*, Mir Publishers, Moscow, 1978.

[7] P.J. Kelly, R.D. Arnell, Vacuum 56 (3) (2000) 159.

[8] W.D. Sproul, D.J. Christie, D.C. Carter, Thin Solid Films 491 (1-2) (2005) 1.

[9] R. Behrisch, W. Eckstein, *Sputtering by Particle Bombardment: Experiments and Computer Calculations from Threshold to MeV Energies*, Springer, Berlin, 2007.

[10] J.E. Greene, in: D. T. J. Hurle (Ed.), *Handbook of Crystal Growth, Vol. 1*, Elsevier Science Publishers, Amsterdam, 1993, pp. 640-681.

[11] P.B. Barna, M. Adamik, Thin Solid Films 317 (1-2) (1998) 27.

[12] L. Hultman, H.T.G. Hentzell, J.E. Sundgren, B.O. Johansson, U. Helmersson, Thin Solid Films 124 (2) (1985) 163.

[13] M. Zlatanović, T. Gredić, A. Kunosić, N. Backović, N. Whittle, Surf. Coat. Technol. 63 (1-2) (1994) 35.

[14] Y. Sun, T. Bell, Mater. Sci. Eng. A 140 (1991) 419.

[15] M.U. Devi, O.N. Mohanty, Surf. Coat. Technol. 107 (1) (1998) 55.

[16] Y. Makino, K. Nogi, Surf. Coat. Technol. 98 (1-3) (1998) 1008.

[17] P.H. Mayrhofer, D. Music, Th. Reeswinkel, H.G. Fuß, J.M. Schneider, Acta Mater. 56 (11) (2008) 2469.

[18] R. Cremer, M. Witthaut, D. Neuschütz, in: W. D. Cho, H. Y. Sohn (Eds.), *Value-Addition Metallurgy*, The Minerals, Metals & Materials Society, Warrendale, PA, 1998, pp. 249-258.

[19] M. Kawate, A. Kimura, T. Suzuki, J. Vac. Sci. Technol. A 20 (2) (2002) 569.

[20] S. Hofmann, H.A. Jehn, Werkst. Korros. 41 (12) (1990) 756.

[21] L. Chen, Y. Du, S.Q. Wang, J. Li, Int. J. Refract. Met. Hard Mater. 25 (5-6) (2007) 400.

[22] P.H. Mayrhofer, A. Hörling, L. Karlsson, J. Sjölén, T. Larsson, C. Mitterer, L. Hultman, Appl. Phys. Lett. 83 (10) (2003) 2049.

[23] A. Knutsson, M.P. Johansson, L. Karlsson, M. Odén, J. Appl. Phys. 108 (4) (2010) 044312.

[24] A. Knutsson, M.P. Johansson, L. Karlsson, M. Odén, Surf. Coat. Technol. 205 (16) (2011) 4005.

[25] L. Chen, Y. Du, X. Xiong, K.K. Chang, M.J. Wu, Int. J. Refract. Met. Hard Mater. 29 (6) (2011) 681.

[26] A. Sugishima, H. Kajioka, Y. Makino, Surf. Coat. Technol. 97 (1-3) (1997) 590.

[27] Y. Ide, T. Nakamura, K. Kishitake, in: B. Mishra, C. Yamauchi (Eds.), Proceedings of the 2nd International Conference on Processing Materials for Properties, The Minerals, Metals & Materials Society, Warrendale, PA, 2000, pp. 291-296.

[28] A.E. Reiter, V.H. Derflinger, B. Hanselmann, T. Bachmann, B. Sartory, Surf. Coat. Technol. 200 (7) (2005) 2114.

[29] R. Franz, B. Sartory, R. Kaindl, R. Tessadri, A. Reiter, V.H. Derflinger, P. Polcik, C. Mitterer, in: G. Kneringer, P. Rödhammer, H. Wildner (Eds.), Proceedings of the 16th International Plansee Seminar, vol. 2, Plansee Holding AG, Reutte, 2005, pp. 932-945.

[30] K. Holmberg, A. Matthews, *Coatings Tribology: Properties, Mechanisms, Techniques and Applications in Surface Engineering*, 2nd ed., Elsevier, Amsterdam, 2009.

[31] J.G. Nee, *Fundamentals of Tool Design*, Society of Manufacturing Engineers, Dearborn, MI, 1998.

[32] O. Knotek, F. Löffler, G. Krämer, in: R. F. Bunshah (Ed.), *Handbook of Hard Coatings: Deposition Technologies, Properties and Applications*, Noyes Publications, Park Ridge, NJ, 2001, pp. 370-410.

[33] E. Paucksch, S. Holsten, M. Linß, F. Tikal, *Zerspantechnik: Prozesse, Werkzeuge, Technologien*, Vieweg+Teubner, Wiesbaden, 2008.

[34] H.-P. Stüwe, *Einführung in die Werkstoffkunde*, 2nd ed., Bibliographisches Institut, Mannheim, 1991.

[35] H. Leitner, P. Staron, H. Clemens, S. Marsoner, P. Warbichler, Mater. Sci. Eng. A 398 (1-2) (2005) 323.

[36] H.F. Fischmeister, S. Karagöz, H.O. Andrén, Acta Metall. 36 (4) (1988) 817.

[37] S. Karagöz, H.O. Andrén, Z. Metallkd. 83 (6) (1992) 386.

[38] R. Ebner, H. Leitner, F. Jeglitsch, D. Caliskanoglu, in: F. Jeglitsch, R. Ebner, H. Leitner (Eds.), *Tool Steels in the Next Century: Proceedings of the. 5th International Conference on Tooling*, Institut für Metallkunde und Werkstoffprüfung, Montan-universität Leoben, 1999, pp. 3-24.

[39] Böhler Edelstahl GmbH & Co KG, *Böhler S290 Microclean*, http://www.bohler-edelstahl.com/files/S290DE.pdf, September 2013.

[40] W. Schedler, *Hartmetall für den Praktiker: Aufbau, Herstellung, Eigenschaften und industrielle Anwendung einer modernen Werkstoffgruppe*, VDI-Verlag, Düsseldorf, 1988.

[41] H. Tschätsch, J. Dietrich, *Praxis der Zerspantechnik: Verfahren, Werkzeuge, Berechnung*, Vieweg+Teubner, Wiesbaden, 2008.

[42] H. Danninger, F. Rouzbahani, Ch. Harold, H. Ponemayr, M. Daxelmüller, F. Simančík, K. Iždinský, Powder Metall. Progr. 5 (2) (2005) 92.

[43] E. Eidenberger, E. Stergar, H. Leitner, P. Staron, J. Spitaler, C. Ambrosch-Draxl, H. Clemens, Appl. Phys. A: Mater. Sci. Process. 97 (2) (2009) 331.

[44] H. Leitner, M. Schober, H. Clemens, D. Caliskanoglu, F. Danoix, Int. J. Mater. Res. 99 (4) (2008) 367.

[45] H. Danninger, C. Harold, F. Rouzbahani, H. Ponemayr, M. Daxelmüller, F. Simančík, K. Iždinský, Adv. Powder. Metall. Part. Mater., Proceedings of the 2008 World Congress on Powder Metallurgy and Particulate Materials, 2008, pp. 1077-1089.

[46] H. Danninger, Ch. Harold, Ch. Gierl, H. Ponemayr, M. Daxelmüller, F. Simančík, K. Iždinský, Acta Phys. Pol. A 117 (5) (2010) 825.

[47] R.F. Bunshah, in: R. F. Bunshah (Ed.), *Handbook of Hard Coatings: Deposition Technologies, Properties and Applications*, Noyes Publications, Park Ridge, NJ, 2001, pp. 4-76.

[48] R.A. Haefer, *Oberflächen- und Dünnschicht-Technologie, Teil 1: Beschichtungen von Oberflächen*, Springer, Berlin, Heidelberg, 1987.

[49] J.A. Thornton, in: R. F. Bunshah (Ed.), *Deposition Technologies for Films and Coatings: Developments and Applications*, Noyes Publications, Park Ridge, NJ, 1982, pp. 170-243.

[50] M. Ohring, *Materials Science of Thin Films: Deposition and Structure*, 2nd ed., Academic Press, San Diego, CA, 2002.

[51] N. Bagcivan, K. Bobzin, S. Theiß, Thin Solid Films 528 (2013) 180.

[52] B. Rother, J. Vetter, *Plasmabeschichtungsverfahren und Hartstoffschichten*, 1st ed., Deutscher Verlag für Grundstoffindustrie, Leipzig, 1992.

[53] S. Vuorinen, R.H. Hoel, Thin Solid Films 232 (1) (1993) 73.

[54] B.A. Movchan, A.V. Demchishin, Phys. Met. Metall. 28 (4) (1969) 653.

[55] J.A. Thornton, Ann. Rev. Mater. Sci. 7 (1977) 239.

[56] R. Messier, A.P. Giri, R.A. Roy, J. Vac. Sci. Technol. A 2 (2) (1984) 500.

[57] L. Hultman, J.E. Sundgren, in: R. F. Bunshah (Eds.), *Handbook of Hard Coatings: Deposition Technologies, Properties and Applications*, Noyes Publications, Park Ridge, NJ, 2001, pp. 108-180.

[58] A. Anders, Thin Solid Films 518 (15) (2010) 4087.

[59] O. Knotek, M. Böhmer, T. Leyendecker, J. Vac. Sci. Technol. A 4 (6) (1986) 2695.

[60] W.D. Münz, J. Vac. Sci. Technol. A 4 (6) (1986) 2717.

[61] H.A. Jehn, B. Rother, Int. J. Refract. Met. Hard Mater. 14 (1-3) (1996) 87.

[62] P. Spencer, Z. Metallkd. 92 (10) (2001) 1145.

[63] A. Hörling, L. Hultman, M. Odén, J. Sjölén, L. Karlsson, Surf. Coat. Technol. 191 (2-3) (2005) 384.

[64] D. McIntyre, J.E. Greene, G. Håkansson, J.E. Sundgren, W.D. Münz, J. Appl. Phys. 67 (3) (1990) 1542.

[65] A. Hörling, L. Hultman, M. Odén, J. Sjölén, L. Karlsson, J. Vac. Sci. Technol. A 20 (5) (2002) 1815.

[66] R. Rachbauer, S. Massl, E. Stergar, D. Holec, D. Kiener, J. Keckes, J. Patscheider, M. Stiefel, H. Leitner, P.H. Mayrhofer, J. Appl. Phys. 110 (2) (2011) 023515.

[67] P.H. Mayrhofer, F.D. Fischer, H.J. Böhm, C. Mitterer, J.M. Schneider, Acta Mater. 55 (4) (2007) 1441.

[68] I.A. Abrikosov, A. Knutsson, B. Alling, F. Tasnádi, H. Lind, L. Hultman, M. Odén, Materials 4 (9) (2011) 1599.

[69] R. Rachbauer, E. Stergar, S. Massl, M. Moser, P.H. Mayrhofer, Scr. Mater. 61 (7) (2009) 725.

[70] A. Knutsson, J. Ullbrand, L. Rogström, N. Norrby, L.J.S. Johnson, L. Hultman, J. Almer, M.P. Johansson Jöesaar, B. Jansson, M. Odén, J. Appl. Phys. 113 (21) (2013) 213518.

[71] B. Alling, M. Odén, L. Hultman, I.A. Abrikosov, Appl. Phys. Lett. 95 (18) (2009) 181906.

[72] F. Rovere, D. Music, S. Ershov, M. to Baben, H.G. Fuss, P.H. Mayrhofer, J.M. Schneider, J. Phys. D: Appl. Phys. 43 (3) (2010) 035302.

[73] L. Rogström, J. Ullbrand, J. Almer, L. Hultman, B. Jansson, M. Odén, Thin Solid Films 520 (17) (2012) 5542.

[74] N. Schalk, C. Mitterer, J. Keckes, M. Penoy, C. Michotte, Surf. Coat. Technol. 209 (2012) 190.

[75] A. Knutsson, M.P. Johansson, P.O.Å. Persson, L. Hultman, M. Odén, Appl. Phys. Lett. 93 (14) (2008) 143110.

[76] A. Knutsson, I.C. Schramm, K. Asp Grönhagen, F. Mücklich, M. Odén, J. Appl. Phys. 113 (11) (2013) 114305.

[77] J.S. Koehler, Phys. Rev. B 2 (2) (1970) 547.

[78] L. Hultman, C. Engström, M. Odén, Surf. Coat. Technol. 133-134 (2000) 227.

[79] N.E. Christensen, I. Gorczyca, Phys. Rev. B 47 (8) (1993) 4307.

[80] Q. Xia, H. Xia, A.L. Ruoff, J. Appl. Phys. 73 (12) (1993) 8198.

[81] Q. Li, I.W. Kim, S.A. Barnett, L.D. Marks, J. Mater. Res. 17 (5) (2002) 1224.

[82] O. Banakh, P.E. Schmid, R. Sanjinés, F. Lévy, Surf. Coat. Technol. 163-164 (2003) 57.

[83] H. Willmann, P.H. Mayrhofer, L. Hultman, C. Mitterer, J. Mater. Res. 23 (11) (2008) 2880.

[84] P.H. Mayrhofer, F. Rovere, M. Moser, C. Strondl, R. Tietema, Scr. Mater. 57 (3) (2007) 249.

[85] H. Willmann, P.H. Mayrhofer, P.O.Å. Persson, A.E. Reiter, L. Hultman, C. Mitterer, Scr. Mater. 54 (11) (2006) 1847.

8. Publications

8.1 List of included publications

I. Duplex processing for increased adhesion of sputter deposited $Ti_{1-x}Al_xN$ coatings on a Fe-25%Co-15%Mo tool material
T. Weirather, A. Fian, B. Sartory, D. Caliskanoglu, W. Kölker, C. Mitterer
Surface and Coatings Technology 206 (2012) 3601-3606.

II. Increased thermal stability of $Ti_{1-x}Al_xN$/TiN multilayer coatings through high temperature sputter deposition on powder-metallurgical high-speed steels
T. Weirather, K. Chladil, B. Sartory, D. Caliskanoglu, R. Cremer, W. Kölker, C. Mitterer
Submitted for publication.

III. Industrial-scale sputter deposition of $Cr_{1-x}Al_xN$ coatings with $0.21 \leq x \leq 0.74$ from segmented targets
T. Weirather, C. Czettl, P. Polcik, M. Kathrein, C. Mitterer
Surface and Coatings Technology 232 (2013) 303-310.

8.2 Publications related to this thesis

IV. High temperature sputter deposition of $Ti_{1-x}Al_xN$ coatings on powder-metallurgical high-speed steels
T. Weirather, K. Kutschej, D. Caliskanoglu, R. Cremer, W. Kölker, J. Kohlscheen, C. Mitterer
Proceedings of the 8th International Tooling Conference, vol. 2, RWTH Aachen University, Aachen, 2009, pp. 881-889.

V. A comparative study on $Ti_{1-x}Al_xN$ coatings reactively sputtered from compound and from mosaic targets
N. Schalk, T. Weirather, C. Polzer, P. Polcik, C. Mitterer
Surface and Coatings Technology 205 (2011) 4705-4710.

VI. Industrial-scale sputter deposition of $Cr_{1-x}Al_xN$ coatings with various compositions from segmented powder-metallurgical targets
T. Weirather, C. Czettl, P. Polcik, M. Kathrein, C. Mitterer
Proceedings of the 18th International Plansee Seminar, Plansee SE, Reutte, 2013, HM124.

VII. Combinatorial synthesis of hard coatings using co-sputtering from segmented targets
S. Gangopadhyay, T. Weirather, C. Sabitzer, M. Tkadletz, C. Czettl, P. Polcik, M. Kathrein, C. Mitterer
in final preparation.

8.3 My contribution to the included publications

	Conception and planning	Experiments	Analysis and interpretation	Manuscript preparation
Publication I	90%	80%	90%	100%
Publication II	80%	60%	90%	100%
Publication III	80%	80%	95%	100%

Supervision not included!

Publication I

Duplex processing for increased adhesion of sputter deposited $Ti_{1-x}Al_xN$ coatings on a Fe-25%Co-15%Mo tool material

T. Weirather, A. Fian, B. Sartory, D. Caliskanoglu, W. Kölker, C. Mitterer

Surface and Coatings Technology 206 (2012) 3601-3606

Duplex processing for increased adhesion of sputter deposited $Ti_{1-x}Al_xN$ coatings on a Fe-25%Co-15%Mo tool material

T. Weirather[a], A. Fian[b], B. Sartory[c], D. Caliskanoglu[d], W. Kölker[e], C. Mitterer[a]

[a] Department of Physical Metallurgy and Materials Testing, Montanuniversität Leoben, Franz-Josef-Straße 18, 8700 Leoben, Austria

[b] MATERIALS – Institute of Surface Technology and Photonics, Joanneum Research Forschungsgesellschaft mbH, Franz-Pichler-Straße 30, 8160 Weiz, Austria

[c] Materials Center Leoben Forschung GmbH, Roseggerstraße 12, 8700 Leoben, Austria

[d] Böhler Edelstahl GmbH & Co KG, Mariazeller Straße 25, 8605 Kapfenberg, Austria

[e] CemeCon AG, Adenauerstraße 20 A4, 52146 Würselen, Germany

Abstract

Recently, carbide-free alloying systems with yield strength $R_{p0.1}$ up to 4000 MPa and outstanding thermal stability are available, which offer the possibility to elevate coating deposition temperatures up to 600 °C. The present work demonstrates that the limited $Ti_{1-x}Al_xN$ coating adhesion on a Fe-25%Co-15%Mo grade caused by the absence of carbides in the substrates can be significantly improved from HF 4 to HF 2 in the Rockwell adhesion test by plasma-assisted nitriding during sputter etching. X-ray photoelectron spectroscopy measurements reveal that the nitrogen diffusion zone is confined to the first few nanometres of the substrate surface, while mainly Mo-N and partly Fe-N bondings are formed. X-ray diffraction exhibits the formation of cubic Mo_2N in the nitrided layer. The coatings show a single-phase face-centered cubic $Ti_{1-x}Al_xN$ structure tending to a preferred (110) growth orientation with increasing nitriding time. Tribological tests performed at room temperature and 650 °C indicate superior wear performance of duplex $Ti_{1-x}Al_xN$ coated Fe-25%Co-15%Mo.

Keywords: Duplex TiAlN coatings, Fe-Co-Mo tool material, adhesion, XPS, XRD, tribology

1. Introduction

$Ti_{1-x}Al_xN$ hard coatings are typically used for wear protection of high-speed steel (HSS) and cemented carbide cutting tools. As film deposition temperatures are limited by the substrate's thermal stability, they do usually not exceed 500 °C for coating of HSS [1]. In a recent publication [2], it was shown that the availability of powder-metallurgical HSS (PM-HSS) with softening temperatures of up to 560 °C offers the possibility to increase deposition temperatures distinctly beyond the usual ones. In cutting tests, $Ti_{1-x}Al_xN$ coatings deposited on PM-HSS at a substrate temperature of 575 °C showed an increase in wear performance of about 40% compared to those deposited at 420 °C.

Recently, a novel tool material with yield strength $R_{p0.1}$ of up to 4000 MPa and outstanding thermal stability is available, which is based on a completely carbide-free intermetallic alloying concept. Fe-25%Co-15%Mo (wt.%) shows a precipitation hardening behaviour, described in more detail by Leitner et al. [3], comparable to that of Al-alloys. Its microstructure in the relatively soft as-quenched state consists of an Fe-Co martensite with embedded coarse primary µ-phase $(Fe,Co)_7Mo_6$ precipitates. During ageing, nanometre-sized secondary µ-phase precipitations are formed, resulting in a significant hardness increase. Investigations on e.g. mechanical properties and temper resistance of Fe-25%Co-15%Mo performed by Danninger et al. [4] revealed that peak hardness is obtained at aging temperatures of about 600 °C. Furthermore, the thereby arising distortion is almost negligible. These facts make Fe-25%Co-15%Mo a promising material for manufacturing of precision tools, while coating deposition temperatures can even be raised to 600 °C.

According to Hultman et al. [5], TiN coating adhesion on carbidic HSS is highly influenced by local epitaxy between the MC carbides (mainly $VC_{0.8}$) and the growing film. TiN and $VC_{0.8}$ reveal the same crystal structure (NaCl B1), and their misfit in lattice parameter, which is as low as 2%, is accommodated by dislocations. The resulting coherent interfaces exhibit low interfacial energy, promoting coating adhesion.

However, as far as the $(Fe,Co)_7Mo_6$ precipitates in Fe-25%Co-15%Mo reveal an ordered rhomboedric crystallographic structure (Fe_7Mo_6 $D8_5$) [6], no epitaxial relations between the substrate surface and the growing face-centered cubic (fcc) $Ti_{1-x}Al_xN$ film are possible. It is thus expected, that the achievable adhesion strength on Fe-25%Co-15%Mo substrates will be limited.

Over the last 20 years, duplex processes combining plasma-assisted nitriding and hard coating deposition gained more and more scientific interest. The effects of plasma nitriding prior to coating deposition were investigated and compared for several types of steel substrates, like e.g. low alloy steels [7], stainless steels [8,9], hot and cold work steels [10-14] as well as HSS [8,14]. Provided that the applied treatment was suitable for the substrate material chosen, beneficial effects on coating adhesion and tribological performance were observed. Duplex treatments require exact process control to tailor the residual stress state at the substrate to coating interface and to avoid white layer formation [7,9,10,13], i.e. the formation of a compound layer on top of the nitrogen diffusion zone during nitriding. Compounds formed near the substrate surface may decompose during further processing and deteriorate coating adhesion and performance [15-17].

The aim of the present work is therefore to evaluate the effects of a duplex treatment, i.e. plasma-assisted nitriding during sputter etching prior to $Ti_{1-x}Al_xN$ film deposition, on Fe-25%Co-15%Mo with regard to coating adhesion as well as to structural and tribological properties.

2. Experimental details

2.1. Substrate pre-treatment and coating deposition

$Ti_{1-x}Al_xN$ coatings were deposited by reactive pulsed DC magnetron sputtering using an industrial scale facility, type CemeCon CC 800/9® MLT, equipped with four unbalanced magnetrons on which CemeCon Ti-Al targets of type TiAl48 GM (500 × 88 × 10 mm³) were mounted. The substrates were ground and polished Fe-25%Co-15%Mo discs of the size Ø 30 × 10 mm (MC90 Intermet grade supplied by Böhler Edelstahl, Kapfenberg, Austria).

All coating processes conducted in the course of this investigation were based on an in-house standard process for deposition of $Ti_{1-x}Al_xN$ hard coatings on PM-HSS. During this process, heating and Ar^+ ion etching of the substrates are used as cleaning pre-treatments prior to film deposition. The sputter etching cycle can further be divided into two steps. In the first step, called MF etching, the substrates' surfaces are sputter-cleaned by a mid-frequency (MF; 250 kHz, 1.6 µs reversal time) asymmetric bipolar pulsed DC glow discharge, where the substrate carousel serves as the cathode (nominal substrate potential $U_b = -650$ V). In the second step, called booster etching, a highly ionized DC plasma is ignited by plasma boosters and biased towards the substrates ($U_b = -200$ V, 250 kHz, 1.4 µs reversal time) to achieve intense ion bombardment. The overall standard process, serving as reference coating deposition process in the present work, is built up by a heating cycle of 90 min, 15 min of MF etching followed by 45 min of booster etching and a $Ti_{1-x}Al_xN$ coating deposition cycle of 180 min at a chamber temperature of 560 °C. Thereby, the two cathode pairs were dual pulsed (cf. [18]) at 20 kHz and a duty cycle of 50% in constant power mode at 7 kW per target. The asymmetric bipolar pulsed DC bias voltage was set to U_b = -50 V at 350 kHz and 1.0 µs reversal time, corresponding to a duty cycle, i.e. the ratio of the negative fraction to the period, of 65%. The base pressure in the deposition chamber was $< 4 \cdot 10^{-3}$ Pa.

While the heating and the coating cycles were kept constant, both etching steps were modified in order to achieve combined sputter cleaning and plasma-assisted nitriding conditions. Therefore, 40 vol.% nitrogen were added to the working gas argon, while the argon flow retained unchanged. Additionally, the substrate temperature during ion etching was raised to about 510 °C, compared to 470 °C and 370 °C in the MF etching and the booster etching step of the standard process, respectively. While the MF etching time was kept constant at 15 min, the booster etching time (BET) was set to 15, 30, 45 and 60 min.

In order to investigate the nitriding effects on the Fe-25%Co-15%Mo substrates, uncoated but plasma nitrided samples were produced as well. Therefore, BETs of 15 and 60 min were chosen after 15 min of MF etching, respectively. Additional reference investigations were performed on untreated Fe-25%Co-15%Mo samples, which were (like all discs used) mechanically polished with diamond suspension (final grade: 1 µm).

2.2. Substrate surface and coating characterization

Chemical composition of the coatings was determined by energy-dispersive X-ray spectroscopy (EDX) using an Oxford Instruments INCA extension in a Zeiss EVO 50 scanning electron microscope. A CSM Instruments Calotest unit was used for coating thickness measurements via ball cratering. Coating adhesion was characterized by the VDI Rockwell indentation test, whereby damage to the coatings in the vicinity of a Rockwell C indent was assigned to adhesion classes between HF 1 and HF 6 according to DIN report 39 [19], using a Mitutoyo Durotwin DT-10 hardness tester.

X-ray photoelectron spectroscopy (XPS) was applied for detailed investigations on the effects of the plasma-assisted nitriding pre-treatment on the Fe-25%Co-15%Mo substrates using an Omicron Nanotechnology Multiprobe surface analysis system with monochromated Al $K_{\alpha 1}$ radiation. Prior to the measurements, volatile surface contaminants like water, carbon monoxide or hydrocarbons were desorbed by heating up the samples to 350 °C in the ultra-high vacuum chamber. A second series of measurements was done after 25 min of Ar^+ sputtering at 2 keV. XPS measurements were carried out on uncoated but plasma nitrided samples after 15 and 60 min BET, respectively, as well as on an untreated reference Fe-25%Co-15%Mo sample.

Crystallographic investigations on untreated, plasma nitrided and duplex coated samples were performed by X-ray diffraction (XRD) in θ/θ as well as grazing incidence (GIXRD) geometry with Cu K_α radiation in a Bruker-AXS D8 Advance diffractometer equipped with parallel beam optics and an energy-dispersive detector (Sol-X from Bruker-AXS). For GIXRD measurements, beam incidence angles of 2° and 4° were chosen. For some of the recorded patterns, Rietveld refinement was applied using the TOPAS software package (version 4.2; Bruker AXS).

Surface roughness measurements were done on untreated as well as on plasma nitrided samples (15 and 60 min BET). A white light optical 3D profiling system of type Veeco Wyko NT1000 was applied in vertical scanning interferometry mode.

2.3. Tribological investigations

Tribological tests were performed using a CSM Instruments high temperature ball-on-disk tribometer with alumina balls of Ø 6 mm, 5 N normal load, a sliding speed of 0.1 m/s, a sliding distance of 300 m, a radius of the wear track of 5 mm and testing temperatures of 25 °C and 650 °C in ambient air. All room temperature (RT) tests were performed at relative humidities of 37-39%. The wear tracks were investigated by white light optical profilometry, using a Veeco Wyko NT1000 device, to derive the volume of the worn area determined by three-dimensional cross sections at four different positions along the wear track. The wear rates (K) were calculated from the measured wear volumes, the wear track circumference, the normal load and the number of laps.

3. Results and discussion

3.1. Coating composition and adhesion

EDX measurements on the deposited $Ti_{1-x}Al_xN$ coatings with a thickness of 4.2 µm showed nearly stoichiometric composition with 49 at.% N and an Al/(Ti+Al) atomic ratio x of 0.49.

As assumed initially, the adhesion of the $Ti_{1-x}Al_xN$ coatings on unnitrided Fe-25%Co-15%Mo (standard process) is limited with HF 4 in the Rockwell test (Fig. 1 (a)). In the closer vicinity of the Rockwell indent, partial coating spallations are obvious in addition to a network of radial cracks. Plasma-assisted nitriding during the etching cycle yielded significant adhesion improvement. For a BET of 15 min, mainly radial cracks with only small coating spallations at the edge of the conical indent are visible; therefore the coating adhesion was rated to HF 2-3 (Fig. 1 (b)). A BET of 60 min further improves the coating adhesion. Only cracks but no noteworthy coating spallations were observed; however, the Rockwell indent itself looks kind of frayed (Fig. 1 (c)). The adhesion was therefore assigned to HF 2. Identical results were obtained already for 30 and 45 min BET (not included in Fig. 1), the coating adhesion was accordingly assigned to HF 2 as well. The higher adhesion strength measured on the samples with higher BET could be an indicator that the adhesion increases with nitriding time. On the other hand, one should keep in mind that – disregarding the different chamber atmospheres – a BET of 15 min corresponds to a third of the BET of the reference process (45 min). Therefore, the slightly lower coating adhesion after 15 min BET compared to e.g. 60 min BET could also be a result of the short substrate pre-treatment. In general, however, it can be stated that the performed duplex processes are suitable to significantly improve $Ti_{1-x}Al_xN$ coating adhesion on Fe-25%Co-15%Mo.

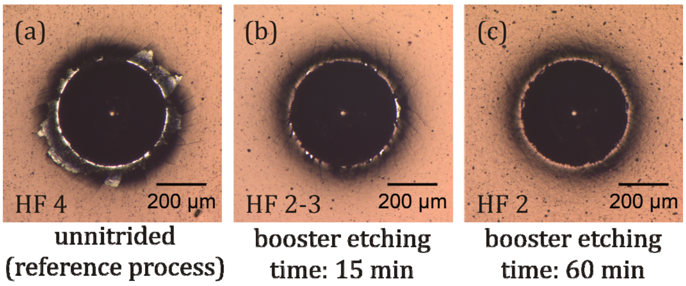

Fig. 1: Results of the Rockwell indentation adhesion tests (images obtained by light optical microscopy): $Ti_{1-x}Al_xN$ deposited on unnitrided Fe-25%Co-15%Mo (a) as well as on nitrided samples with BETs of 15 min (b) and 60 min (c).

3.2. Chemical bonding

Fig. 2 shows all relevant XPS core level spectra, namely Fe2p, Co2p, Mo3d and N1s/Mo3p3/2, of unnitrided Fe-25%Co-15%Mo as well as after nitriding (15 and 60 min BET). The spectra of the nitrided samples do not show any significant differences; therefore it can be assumed that a state of equilibrium is already reached after 15 min BET. Comparing the spectra for unnitrided and both nitrided Fe-25%Co-15%Mo samples, it can be concluded that N provided during ion etching mainly bonds to Mo, partly to Fe and hardly to Co. These results agree well to thermodynamical data denoting that Mo shows the highest affinity to N as Mo_2N has the lowest Gibbs free energy of formation among the expectable nitrides at 510 °C [20-23], which was the chamber temperature during plasma nitriding. In all cases, the peak intensities of the metallic as well as of the oxidic peaks (surface oxidation layer) decrease for the nitrided samples compared to virgin Fe-25%Co-15%Mo. In the Fe2p core level spectra of the nitrided samples (Fig. 2 (a)), left-hand shoulders for Fe-Fe and Fe-N are identifiable around 707 eV binding energy. A quantitative analysis of all elements as well as their chemical states can be performed by peak deconvolution using a Voight profile (instrument-, stoichiometry- and crystallinity-induced Gaussian peak-broadening, core level lifetime-induced Lorentzian broadening [24]). The excellent resolution by using monochromated X-rays allows a quite accurate determination of the N1s peak which is close to the position of the Mo3p3/2 peak. On the other hand, it should be mentioned that the determination of peak contributions of the Fe- and Co-bonds is not very precise due to the large stoichiometry- and lifetime-broadening of the 2p-peaks of transition metals. As a result of the quantification, a fraction of 5 at.% of Mo and 7 at.% of N can be found for both BETs. From these 7 at.% of N approximately 3 at.% can be assigned to Fe-N and 1 at.% to Co-N bonds. Consequently, the Mo:N atomic ratio in the measured volume corresponds to 5:3, which is close to the ideal value for Mo_2N, i.e. 2:1. Therefore, it can be concluded that a reasonable probability for the formation of Mo_2N is given. Peak fitting combined with calculations for the inelastic mean free path [25] of the photoelectrons in Fe-based matter reveal that the nitrided layer has a thickness of approximately 5 nm for both BETs. To be more precise, it has to be noted that this 5 nm layer already includes the residual surface oxidation layer. As indicated in Fig. 2 (c) and (d), the XPS spectra of Mo3d and N1s after Ar^+ sputtering inside the ultra-high vacuum system show neither a significant residual amount of nitrogen nor a chemical shift of Mo3d. The sputter depth after 25 min is in the range of 10 nm which is confirming the considerations above that the nitrided layer is only confined to the first few nanometres of the sample surface. This could be a result of the high Mo content in the substrate material, which is a strong nitride former as mentioned before. Nakata et al. [26] investigated the plasma nitriding behaviour of quasi-binary alloys of low carbon steels and strong nitride formers. Although in a different order of magnitude, they observed that the depth of the nitrided layer decreases distinctly with increasing absolute values of the Gibbs free energy for alloying element nitride formation. Furthermore, the depth of the nitrided layer significantly decreased with increasing concentration of the individual alloying elements. As the Mo content of the substrate material in the present work is distinctly higher than in the cited publication (0.5-1.5 wt.% [26]), the described effects are likely to be significantly more pronounced.

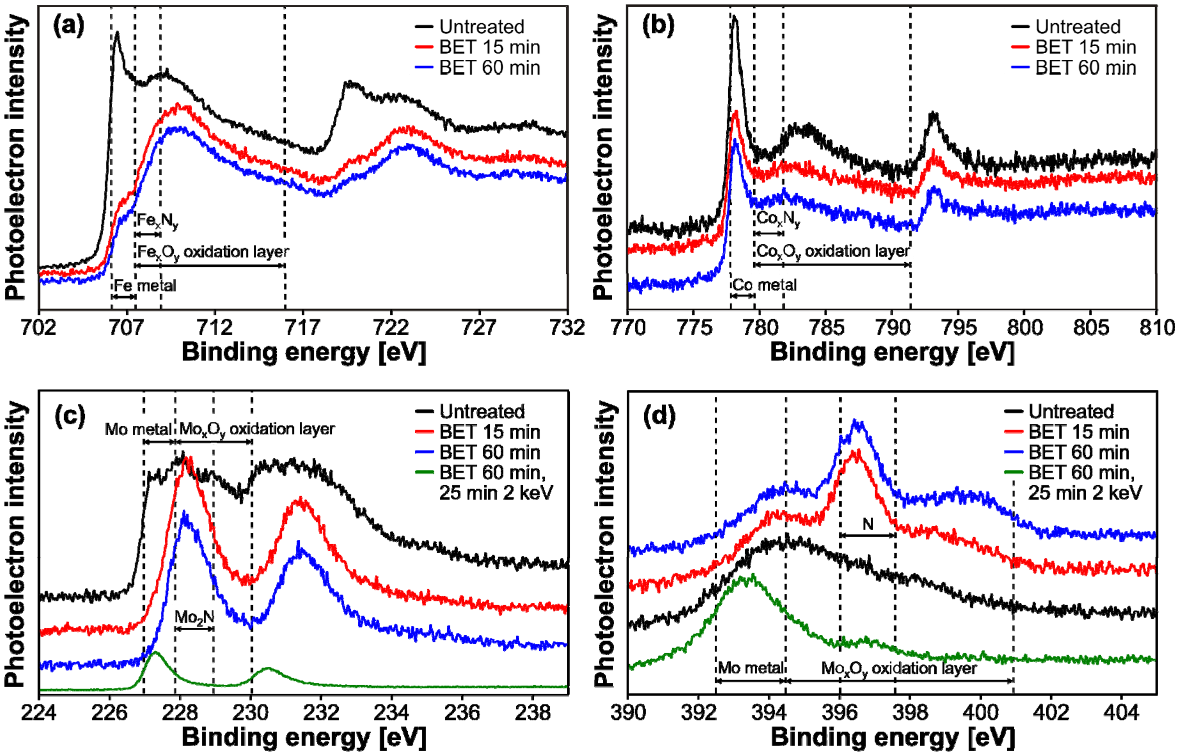

Fig. 2: XPS core level spectra of untreated Fe-25%Co-15%Mo and after plasma nitriding: Fe2p (a), Co2p (b), Mo3d (c) and N1s/Mo3p3/2 (d). In (c) and (d) the XPS spectra after 25 min Ar$^+$ sputtering at 2 keV are included.

3.3. Structural evolution

An overview of the (GI)XRD investigations performed on nitrided (15 and 60 min BET) and unnitrided Fe-25%Co-15%Mo is depicted in Fig. 3. For the nitrided samples, the patterns measured with parallel beam optics in θ/θ and in GI configuration ($\theta = 2°$) are compared as the structural information of the GIXRD diffractogram primarily stems from the surface-near region [27]. As described earlier, the substrate's microstructure consists of primary and secondary μ-phase $(Fe,Co)_7Mo_6$ precipitates embedded in a matrix of Fe-Co martensite. The matrix peaks are indicated with the standard positions for α-Fe [28], while the peaks are slightly shifted to lower diffraction angles. This peak shift can be related to an increased unit cell volume due to martensitic hardening. The μ-phase peaks are indicated by the standard positions for Co_7Mo_6 available from ICDD [28]. Here, a slight peak shift to higher 2θ angles is obvious, which probably corresponds to a compressive stress state of the precipitates. By comparing the patterns of the nitrided sample with 15 min BET measured at constant $\theta = 2°$ and untreated Fe-25%Co-15%Mo, no obvious signs for the formation of Mo_2N are detectable. However, in the pattern of the 60 min BET sample measured in GI mode the formation of cubic (100) oriented Mo_2N [28] cannot be excluded, as a left-hand shoulder on the $(Fe,Co)_7Mo_6$ peak at a diffraction angle of approximately $2\theta = 43.4°$ emerges (see Fig. 3). The high number of overlapping peak positions of Mo_2N and Co_7Mo_6 could be a reason why there is only one position at which a sign for peak formation is observable. The low depth of the nitrided layer as shown by XPS measurements could be a second reason, as a phase growing in a nanometre-thick layer will probably show a predominant orientation.

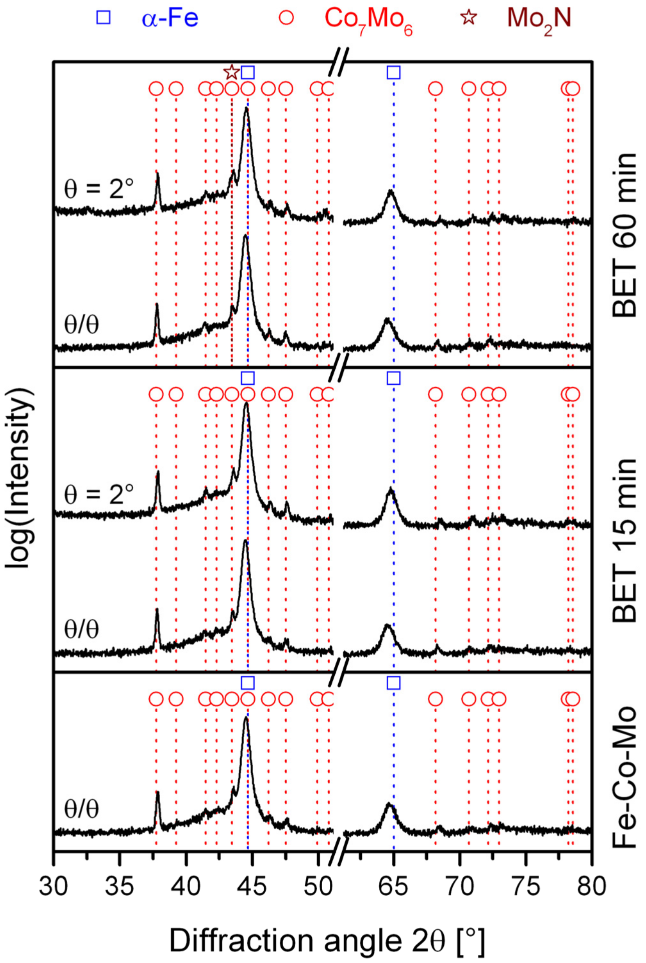

Fig. 3: Summary of the XRD investigations conducted with parallel beam optics in θ/θ and GI configuration (incidence beam angle $\theta = 2°$) on unnitrided and nitrided Fe-25%Co-15%Mo (15 and 60 min BET).

To gain more substantiated information, Rietveld refinement was performed for the GIXRD patterns of both nitrided samples and the reference Fe-25%Co-15%Mo pattern. Although the quantitative results thereof are not relevant as the information depth of the

GIXRD measurements at $\theta = 2°$ is much higher than the thickness of the nitrided layer as discussed in the XPS section, qualitative conclusions may be derived. The obtained results, however, confirm the presence of cubic Mo_2N even in both nitrided samples with increasing phase fraction for 60 min BET compared to 15 min. According to the results of XPS quantification, the nitrogen content and the depth of the nitrided layer do not significantly differ for the different BETs. Therefore, the somewhat higher Mo_2N phase fraction in the 60 min BET sample is most likely due to the progress in crystal growth [29]. As the crystal structure of Mo_2N is fcc-like [30] and the lattice constant is almost the same as for $VC_{0.8}$ reported by Hultman et al. and ICDD [5,28], epitaxial relations between the nitrided substrate surface and the $Ti_{1-x}Al_xN$ coatings would be a conclusive reason for the observed adhesion increase. The slightly more pronounced coating adhesion after 60 min BET (Fig. 1) would consequently arise from the higher Mo_2N fraction according to Rietveld refinement results of the recorded GIXRD data. The lattice mismatch of 0.5%, however, would corroborate the existence of epitaxial relations between the Mo_2N phase in the substrate surface (lattice parameter a = 4.16 Å, [28]) and the growing $Ti_{0.51}Al_{0.49}N$ film (a = 4.18 Å, calculated after [28] according to Vegard's rule).

The calculated lattice parameter for $Ti_{0.51}Al_{0.49}N$ mentioned above was used in Fig. 4 to indicate the (GI)XRD peak positions of the coatings deposited on nitrided Fe-25%Co-15%Mo (15 and 60 min BET) recorded in θ/θ as well as in $\theta = 4°$ configuration. The pattern measured on untreated Fe-25%Co-15%Mo in θ/θ configuration is given as a reference, as the respective scans of the duplex coated samples contain information stemming from the substrates as well, i.e. the matrix peaks and some of the µ-phase peaks. From Fig. 4 it can be concluded that the coatings show single-phase fcc $Ti_{1-x}Al_xN$ structure, where fcc AlN substitutes for a fraction of fcc TiN forming a metastable fcc $Ti_{1-x}Al_xN$ solid solution. However, the $Ti_{1-x}Al_xN$ coating peaks measured on the 60 min BET sample are distinctly sharper than those for 15 min BET. Therefore, it can be concluded that the crystallinity of the coatings grown after the longer nitriding pre-treatment is significantly higher or, vice versa, the coating grain size is smaller after the shorter nitriding step [27]. To explain the mechanism behind this phenomenon would go beyond the focus of this work, but it could be speculated that, according to the discussion of the GIXRD experiments performed on the nitrided samples, the higher crystallinity of the coatings grown on 60 min BET samples are a result of the higher fraction of Mo_2N on the substrate surface leading to a higher area fraction where the initial coating growth is beneficially affected by epitaxial effects. Comparing the θ/θ scans of the duplex coated samples in Fig. 4, a change of preferred orientation from (111) to (110) with increasing

BET is obvious. This effect is known from literature for TiN and $Ti_{1-x}Al_xN$ duplex coating processes performed on tool steel substrates [12,14,31].

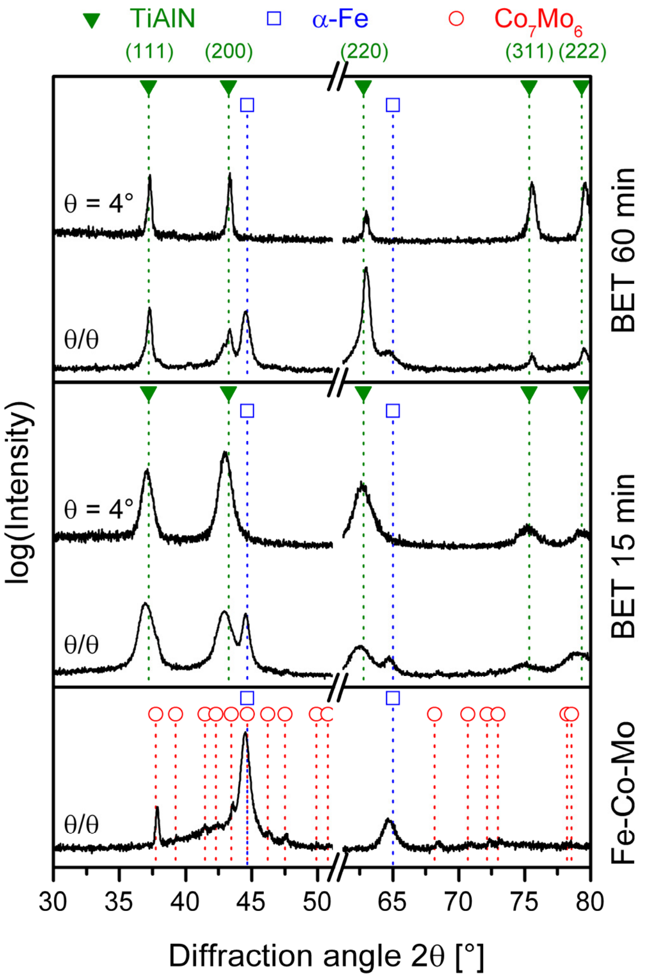

Fig. 4: Summary of the XRD investigations conducted with parallel beam optics in θ/θ and GI configuration (incidence beam angle θ = 4°) on unnitrided and duplex coated Fe-25%Co-15%Mo (15 and 60 min BET).

3.4. Substrate surface roughness and tribology

As shown in Fig. 5, the arithmetic mean surface roughness (R_a) of the substrates decreases distinctly through combined sputter etching and nitriding compared to untreated Fe-25%Co-15%Mo. This can be explained by atomic shot blasting effects, i.e. preferred removal of material from surface asperities by the sputter process. Comparing the R_a values after BETs of 15 and 60 min, a very slight and probably insignificant increase with time is visible. On the other hand, the surface topography seems to become more uniform as the length of the error bars decreases significantly. This is explainable by the longer and therefore more effective sputter etching pre-treatment. It can be concluded, however, that the surface topography after plasma nitriding is smooth while no observable negative influence of the nitriding pre-treatment and the resulting Mo_2N formation was found.

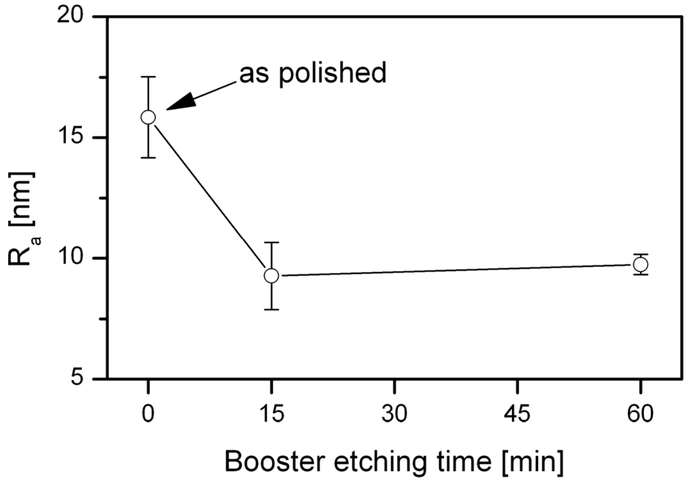

Fig. 5: Evolution of the arithmetic mean substrate surface roughness R_a with BET compared to unnitrided samples.

In order to evaluate the performance of the investigated duplex coatings, tribological tests against alumina balls were performed at RT and 650 °C. The friction curves showed steady-state behaviour after a short running-in period. Therefore, the recorded values of the friction coefficient μ were averaged omitting the first 25 m of the sliding distance. The resulting mean values lie constantly at $\mu \approx 0.9$ at RT and $\mu \approx 0.7$ at 650 °C for all BETs. Profilometric investigations revealed that abrasion is the dominating wear mechanism at RT, while at 650 °C abrasion and oxidational wear are dominating [32]. The calculated wear coefficients K are plotted versus BET in Fig. 6. At RT, K ranges from $7.9 \cdot 10^{-15}$ to $1.1 \cdot 10^{-14}$ m^3/Nm, while values from $0.6 \cdot 10^{-15}$ to $3.2 \cdot 10^{-15}$ m^3/Nm were obtained at 650 °C.

Therefore, the tribological properties are well competitive compared to published data for $Ti_{1-x}Al_xN$ coatings on common tool steels [2,33-37]. At both testing temperatures, a slight increase of K with BET is obvious. The higher wear performance at lower BETs could be explained by enhanced mechanical properties resulting from the lower $Ti_{1-x}Al_xN$ domain size as shown by XRD (see Fig. 4). The lowest wear coefficient at 650 °C was observed after 30 min BET. Here, most probably the best compromise between Mo_2N formation and the resulting adhesion increase and mechanical properties of the coating is reached. However, the results of the tribological tests corroborate the high potential of duplex $Ti_{1-x}Al_xN$ coated Fe-25%Co-15%Mo for severe conditions, e.g. in cutting.

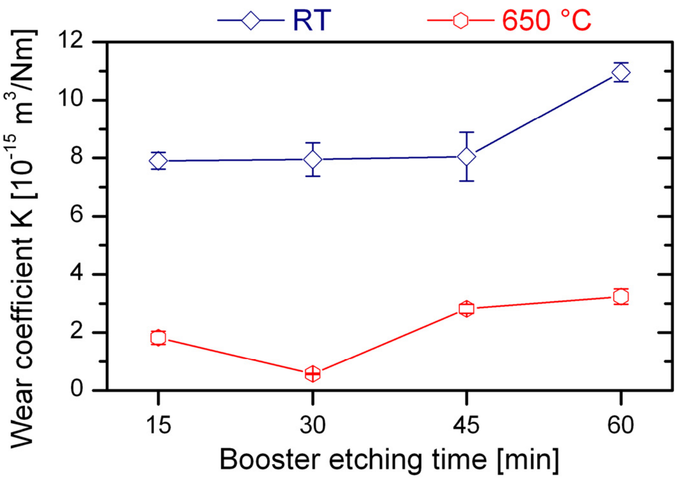

Fig. 6: Calculated wear coefficients of duplex $Ti_{1-x}Al_xN$ coatings deposited after different BETs. Tribological tests were performed against alumina balls at room temperature (RT) and 650 °C.

4. Conclusions

Within this work, duplex processes combining plasma-assisted nitriding during Ar^+ ion etching with varying durations and $Ti_{1-x}Al_xN$ sputter deposition were performed on Fe-25%Co-15%Mo substrates, which is a novel high-strength tool material with outstanding thermal stability. It can be stated that the applied duplex processes yield significantly increased coating adhesion compared to standard processing without nitriding pre-treatment. XPS measurements revealed a state of equilibrium concerning the nitriding effects even after the shortest nitriding pre-treatment, while, with the chosen parameters, the nitrided layer is confined to the topmost few nanometres. Here, N mainly bonds to Mo, and cubic Mo_2N is formed, elucidating the increased coating adhesion strength. The single-phase cubic $Ti_{0.51}Al_{0.49}N$ coatings show a change in preferred orientation from (111) to (110) through plasma nitriding. Furthermore, it was observed that the coating crystallinity increases with nitriding time. Tribological tests emphasize the high potential of duplex $Ti_{1-x}Al_xN$ coated Fe-25%Co-15%Mo especially for shorter nitriding pre-treatments. In conclusion, it can be stated that the investigated duplex treatment makes the $Ti_{1-x}Al_xN$ coated Fe-25%Co-15%Mo grade an auspicious candidate for severe high-speed cutting applications.

Acknowledgements

This work was done within the Research Studio Austria Surface Engineering, with financial support from the Österreichische Forschungsförderungsgesellschaft and the Bundesministerium für Wirtschaft, Familie und Jugend. Furthermore, technical support by Lars Gey, Taha Hamoudi and Walter May, CemeCon AG, Würselen, Germany, is gratefully acknowledged.

References

[1] B. Rother, J. Vetter, Plasmabeschichtungsverfahren und Hartstoffschichten, 1st ed., Deutscher Verlag für Grundstoffindustrie, Leipzig, 1992.

[2] T. Weirather, K. Kutschej, D. Caliskanoglu, R. Cremer, W. Kölker, J. Kohlscheen, C. Mitterer, in: P. Beiss, C. Broeckmann, S. Franke, B. Keysselitz (Eds.), Proceedings of the 8th International Tooling Conference, vol. 2, RWTH Aachen University, Aachen, 2009, pp. 881-889.

[3] H. Leitner, M. Schober, H. Clemens, D. Caliskanoglu, F. Danoix, Int. J. Mater. Res. 99 (2008) 367-374.

[4] H. Danninger, F. Rouzbahani, Ch. Harold, H. Ponemayr, M. Daxelmüller, F. Simančík, K. Iždinský, Powder Metall. Progr. 5 (2005) 92-103.

[5] L. Hultman, H.T.G. Hentzell, J.E. Sundgren, B.O. Johansson, U. Helmersson, Thin Solid Films 124 (1985) 163-170.

[6] E. Eidenberger, E. Stergar, H. Leitner, P. Staron, J. Spitaler, C. Ambrosch-Draxl, H. Clemens, Appl. Phys. A: Mater. Sci. Process. 97 (2009) 331-340.

[7] Y. Sun, T. Bell, Mater. Sci. Eng. A 140 (1991) 419-434.

[8] M. Van Stappen, B. Malliet, L. Stals, L. De Schepper, J.R. Roos, J.P. Celis, Mater. Sci. Eng. A 140 (1991) 554-562.

[9] T. Michler, M. Grischke, K. Bewilogua, H. Dimigen, Thin Solid Films 322 (1998) 206-212.

[10] M.U. Devi, O.N. Mohanty, Surf. Coat. Technol. 107 (1998) 55-64.

[11] M.H. Staia, Y. Pérez-Delgado, C. Sanchez, A. Castro, E. Le Bourhis, E.S. Puchi-Cabrera, Wear 267 (2009) 1452-1461.

[12] T. Gredić, M. Zlatanović, N. Popović, Ž. Bogdanov, Thin Solid Films 228 (1993) 261-266.

[13] S. Ma, Y. Li, K. Xu, Surf. Coat. Technol. 137 (2001) 116-121.

[14] M. Zlatanović, T. Gredić, A. Kunosić, N. Backović, N. Whittle, Surf. Coat. Technol. 63 (1994) 35-41.

[15] S. Abisset, F. Maury, R. Feurer, M. Ducarroir, M. Nadal, M. Andrieux, Thin Solid Films 315 (1998) 179-185.

[16] J. Walkowicz, J. Smolik, K. Miernik, Surf. Coat. Technol. 116-119 (1999) 361-366.

[17] A. Matthews, S. Franklin, K. Holmberg, J. Phys. D: Appl. Phys. 40 (2007) 5463-5475.

[18] W.D. Sproul, D.J. Christie, D.C. Carter, Thin Solid Films 491 (2005) 1-17.

[19] H.-R. Stock, A. Schulz, W. Ensinger, J. Güttler, E. Fromm, D. Müller, W.D. Busch, H. Grützner, in: H. Jehn, G. Reiners, N. Siegel (Eds.), DIN Fachbericht 39, Beuth Verlag, Berlin, 1993.

[20] E.A. Brandes, Smithells Metals Reference Book, 6th ed., Butterworth Publishers, Stoneham, 1983.

[21] Collaboration: Scientific Group Thermodata Europe (SGTE): Thermodynamic Properties of Compounds, Fe_2I_6 to GeI_4. SpringerMaterials - The Landolt-Börnstein Database (http://www.springermaterials.com). doi:10.1007/10551582_18.

[22] Collaboration: Scientific Group Thermodata Europe (SGTE): Thermodynamic Properties of Compounds, CoP to CrI_2. SpringerMaterials - The Landolt-Börnstein Database (http://www.springermaterials.com). doi:10.1007/10551582_7.

[23] Collaboration: Scientific Group Thermodata Europe (SGTE): Thermodynamic Properties of Compounds, Mn_2O_3 to TaN. SpringerMaterials - The Landolt-Börnstein Database (http://www.springermaterials.com). doi:10.1007/10688868_11.

[24] J.C. Fuggle, J.E. Inglesfield (Eds.), Unoccupied Electronic States: Fundamentals for XANES, EELS, IPS and BIS, Springer, Berlin, 1992, pp. 347-351.

[25] D. Briggs, M.P. Seah (Eds.), Practical Surface Analysis, Vol. 1, Auger and X-ray Photoelectron Spectroscopy, 2nd ed., Wiley, Chichester, 1990, pp. 201-255.

[26] K. Nakata, W. Yamauchi, K. Akamatsu, M. Ushio, Surf. Coat. Technol. 174-175 (2003) 1206-1210.

[27] M. Birkholz, P.F. Fewster, C. Genzel, Thin Film Analysis by X-ray Scattering, Wiley-VCH, Weinheim, 2006.

[28] Powder Diffraction File (Card 00-006-0696 for bcc Fe, card 00-029-0489 for rhombohedral Co_7Mo_6, card 00-025-1366 for cub Mo_2N, card 01-089-2719 for fcc VC, card 00-038-1420 for fcc TiN, card 00-025-1495 for fcc AlN), ICDD International Center for Powder Diffraction Data, PDF-2/Release 2007.

[29] G. Gottstein, Physikalische Grundlagen der Materialkunde, 2nd ed., Springer, Berlin, 2001.

[30] N.S. Gajbhiye, R.S. Ningthoujam, Phys. Stat. Sol. (c) 1 (2004) 3449-3454.

[31] T. Gredić, M. Zlatanović, N. Popović, Ž. Bogdanov, Surf. Coat. Technol. 54-55 (1992) 502-507.

[32] K. Holmberg, A. Matthews, Coatings Tribology: Properties, Techniques and Applications in Surface Engineering, Elsevier, Amsterdam, 1994.

[33] N. Schalk, T. Weirather, C. Polzer, P. Polcik, C. Mitterer, Surf. Coat. Technol. 205 (2011) 4705-4710.

[34] K. Kutschej, P.H. Mayrhofer, M. Kathrein, P. Polcik, C. Mitterer, Surf. Coat. Technol. 188-189 (2004) 358-363.

[35] M. Pfeiler, K. Kutschej, M. Penoy, C. Michotte, C. Mitterer, M. Kathrein, Surf. Coat. Technol. 202 (2007) 1050-1054.

[36] M. Pohler, C. Michotte, M. Penoy, C. Mitterer, M. Kathrein, in: L.S. Sigl, P. Rödhammer, H. Wildner (Eds.), Proceedings of the 17th International Plansee Seminar, Vol. 2, P/M Hard Materials, Plansee Group, Reutte, 2009, pp. HM 72.

[37] J.M. Lackner, W. Waldhauser, R. Ebner, J. Keckés, T. Schöberl, Surf. Coat. Technol. 177-178 (2004) 447-452.

Publication II

Increased thermal stability of $Ti_{1-x}Al_xN$/TiN multilayer coatings through high temperature sputter deposition on powder-metallurgical high-speed steels

T. Weirather, K. Chladil, B. Sartory, D. Caliskanoglu, R. Cremer, W. Kölker, C. Mitterer

submitted for publication

Increased thermal stability of $Ti_{1-x}Al_xN$/TiN multilayer coatings through high temperature sputter deposition on powder-metallurgical high-speed steels

T. Weirather[a], K. Chladil[a], B. Sartory[b], D. Caliskanoglu[c], R. Cremer[d],
W. Kölker[d,e], C. Mitterer[a]

[a] Department of Physical Metallurgy and Materials Testing, Montanuniversität Leoben,
Franz-Josef-Straße 18, 8700 Leoben, Austria

[b] Materials Center Leoben Forschung GmbH, Roseggerstraße 12, 8700 Leoben, Austria

[c] Böhler Edelstahl GmbH & Co KG, Mariazeller Straße 25, 8605 Kapfenberg, Austria

[d] CemeCon AG, Adenauerstraße 20 A4, 52146 Würselen, Germany

[e] Fette GmbH, Grabauer Straße 24, 21493 Schwarzenbek, Germany

Abstract

Although spinodal decomposition of metastable cubic $Ti_{1-x}Al_xN$-based coatings and the underlying mechanisms are widely understood, investigations on the influence of high deposition temperatures are lacking. It is thus the aim of this work to elucidate structure, properties, thermal stability and wear performance of $Ti_{1-x}Al_xN$/TiN multilayer coatings sputter deposited on powder-metallurgical high-speed steels at substrate temperatures of up to 575 °C. Sharper domain boundaries and multilayer interfaces yield increased hardness in the as-deposited state, while the detrimental formation of wurtzite AlN during vacuum annealing is retarded by 50 °C according to Rietveld refinement of X-ray diffractograms. Tribological tests at room temperature and up to 650 °C corroborate the high potential of increased coating temperatures, while demonstrating the crucial importance of using a substrate material with adequate hot hardness. Cutting tests verify the high temperature deposition approach showing a tool life increase of ~40%.

Keywords: TiAlN/TiN multilayer coating, deposition temperature, thermal stability, spinodal decomposition, tribology, cutting tests

1. Introduction

Both scientific and industrial significance have yielded extensive research on the thermal stability along with spinodal decomposition of metastable cubic $Ti_{1-x}Al_xN$ (c-$Ti_{1-x}Al_xN$) over the last decade [1-5]. The steadily growing knowledge on the underlying mechanisms [6-12] enables optimisation of the coating's response to distinct thermal and mechanical loads during application e.g. as wear-protective coating on cutting tools [2,8,13]. The objective is to promote the isostructural spinodal decomposition towards cubic TiN (c-TiN) and AlN (c-AlN) due to the resulting age-hardening effect, while the detrimental transformation of metastable c-AlN to its stable wurtzite structure (w-AlN) needs to be suppressed as it deteriorates both mechanical and tribological coating properties [2,6].

A well accepted approach to enhance the thermal stability of $Ti_{1-x}Al_xN$ is alloying, e.g. with Si, Cr, Zr, Hf or Ta [14-19]. Furthermore, multilayered coating structures of $Ti_{1-x}Al_xN$ and TiN have proven to yield enhanced mechanical properties and thermal stability [13,20-23]. However, investigations on the influence of the coating deposition temperature, which plays a crucial role on the evolving $Ti_{1-x}Al_xN$ microstructure according to structure zone models [24,25], are lacking. Commonly, chamber temperatures in the 300-500 °C range are reported [2,5,10,11,13,20,21,23,26]. Therefore, the aim of this work is to investigate structure and properties as well as thermal stability and tribological performance arising from sputter deposition of multilayered $Ti_{1-x}Al_xN$/TiN coatings at temperatures of up to 575 °C. Consequently, the use of powder-metallurgical high-speed steel (PM-HSS) substrates with substantial hot hardness was crucial, as will be demonstrated. Transmission electron microscopy (TEM), X-ray diffraction (XRD) in the as-deposited state and after vacuum annealing combined with Rietveld refinement, nanoindentation, tribological tests at room temperature (RT), 560 and 650 °C as well as cutting tests were performed to elucidate the benefits of high substrate temperatures during industrial-scale sputter deposition of $Ti_{1-x}Al_xN$/TiN multilayer coatings on PM-HSS substrates.

2. Experimental details

2.1 Coating deposition

The investigated coatings were deposited by reactive direct current (DC) magnetron sputtering using an industrial-scale CemeCon CC 800/9® ML facility. Three of its four unbalanced magnetrons (500 × 88 mm²) were equipped with Ti-Al mosaic targets of type TiAl48 GM (described in more detail in [27]), while a pure Ti target was mounted on the fourth one. The substrates were ground and polished discs of the size Ø 30 × 10 mm made of PM-HSS grades Böhler S390PM (HS10-2-5-8 type) and S290PM (HS14-2.5-5-11 type), quenched and tempered to a hardness of 67 ± 1 HRC, and rectangular Si (100) samples of 0.4 mm thickness. Furthermore, S290PM end mills were coated for cutting tests. Two-fold rotation was applied for the PM-HSS discs and Si, while the end mills were coated under three-fold rotation. As a consequence of both substrate rotation and target configuration [28,29], which implies differing sputter emission distributions from the Ti-Al targets and the Ti target [30,31], the formation of a multilayer structure as obtained by Chen et al. [22] can be anticipated. The substrate temperatures during coating deposition were varied from 375 to 575 °C in five deposition runs and measured by positive temperature coefficient resistors at lower temperatures and by a pyrometer at higher temperatures. In order to achieve the desired temperature variation during deposition, the heating power of the plant's inbuilt heaters was varied, while the settings for the heating and the plasma etching steps prior to the coating step remained unchanged. The magnetrons were operated in constant power mode with 9500 W for the Ti-Al targets and 4000 W for the Ti target. The DC bias voltage during deposition was set to -90 V. The noble gas flows (Ar and Kr) were kept constant, while the N_2 flow was regulated to achieve a predetermined total pressure of 0.57 Pa. The base pressure in the deposition chamber was $\leq 4 \cdot 10^{-3}$ Pa.

2.2 Substrate and coating characterization

A Rockwell HRC hardness tester type emco-test M4R-075 was used to measure the PM-HSS substrate hardness in quenched and tempered state and after being coated at the five different deposition temperatures as well as the coating adhesion. For the latter, the VDI Rockwell indentation test was used, whereupon damage to the coatings in the vicinity of a Rockwell C indent is assigned to adhesion classes between HF 1 and HF 6 according to DIN report 39 [32]. The overall chemical composition of the coatings was determined by energy-dispersive X-ray spectroscopy (EDX) using an Oxford Instruments INCA extension in a Zeiss EVO 50 scanning electron microscope (SEM). The thickness of the coatings was measured via ball cratering with a CSM Instruments Calotest unit.

Crystallographic investigations on as-deposited coatings were performed by X-ray diffraction (XRD) in Bragg-Brentano as well as grazing incidence (GIXRD) geometry in a Siemens D500 diffractometer with Cu K_{α} radiation. For GIXRD measurements, a beam incidence angle of 4° was chosen. Furthermore, investigations on uncoated PM-HSS discs were performed in Bragg-Brentano configuration using the same device. Transmission electron microscopy (TEM) was conducted on coatings deposited onto Si substrates at 375 and 575 °C using a Philips CM20 microscope operating at 200 kV. Energy-filtered TEM (EFTEM) in imaging mode was performed for Ti mapping using a Gatan Imaging Filter. A focused ion beam (FIB) lift-out technique was chosen for the TEM sample preparation, using a FEI Nova 200 NanoLab Dual Beam SEM/FIB microscope.

Coating hardness and Young's modulus were determined with a UMIS (Ultra Micro Indentation System, Fischer-Cripps Laboratories) nanoindenter equipped with a Berkovich tip. The load-displacement data of the conducted plateau tests was analyzed according to the Oliver and Pharr method [33], including area functions determined experimentally using a silica standard of known elastic modulus to account for unavoidable microscopic indenter shape imperfections. Residual stress measurements using the substrate curvature method [34,35] were performed on coated Si platelets, measuring the sample curvature with two parallel laser beams.

2.3 Annealing experiments

A HTM Reetz furnace was used for isothermal vacuum annealing of coated Si samples in the range of 800-950 °C in 50 °C steps for 10 min. All annealing treatments were performed with a base pressure of $< 5\cdot10^{-4}$ Pa and virgin specimen. The heating rate was 20 $K\cdot min^{-1}$, and an isothermal step of 30 min at 250 °C was implemented to remove volatile contaminants. After annealing, the samples were furnace cooled. The thermally induced microstructural changes were investigated via GIXRD at a beam incidence angle of 2° using Cu K_α radiation in a Bruker-AXS D8 Advance diffractometer equipped with parallel beam optics and an energy-dispersive detector (Sol-X from Bruker-AXS). Rietveld refinement of the diffractograms recorded in the angular range of $32° \leq 2\theta \leq 46°$ was subsequently applied using the TOPAS software package (version 4.2; Bruker-AXS) to gain quantitative information on the evolution of the constituent phase fractions, the respective mean crystallite sizes (the mean sizes of the diffracting domains, to be more precise) and the corresponding average lattice constants.

2.4 Tribological investigations

Tribological tests were performed using a CSM Instruments high temperature ball-on-disk tribometer with alumina balls of Ø 6 mm, 5 N normal load, a sliding speed of 0.1 $m\cdot s^{-1}$, a sliding distance of 500 m, a wear track radius of 5 mm and testing temperatures of 25, 560 and 650 °C. All tests were performed in ambient atmosphere at relative humidities of

25 ± 5 %. The wear tracks were investigated by white light optical profilometry, using a Veeco Wyko NT1000 device in vertical scanning interferometry mode, to derive the volume of the worn area determined by three-dimensional cross-sections at four different positions along the wear track. The wear rates (K) were calculated from the measured wear volumes, the wear track circumference, the normal load and the number of laps. Cutting tests were conducted on cold work steel 40CrMnMoS8-6 (DIN 1.2312, tensile strength: 1000 MPa) with a Deckel Maho milling facility. End mills with Ø 16 mm made of S290PM with four flutes, a cutting speed of 100 $m \cdot min^{-1}$, a rotation speed of 1990 min^{-1}, a feed per tooth of 0.08 mm, a feed rate of 636 $mm \cdot min^{-1}$, a width of cut of 1 mm, a depth of cut of 16 mm and a cutting distance of 70 m were used under dry conditions.

Unless otherwise noted, all investigations were done on both coated S390PM and S290PM samples. Measurement of coating hardness and Young's modulus was done on coated S290PM samples because of their higher hot hardness and thermal stability (cf. section 3.1), to avoid possible influences due to softening of the PM-HSS substrates especially after coating deposition at 575 °C.

3. Results and discussion

3.1 Thermal stability of the PM-HSS substrates

The substrate temperatures T_S determined during the five deposition runs were 375, 420, 470, 530 and 575 °C, where the latter two were measured by means of a pyrometer. The Böhler PM-HSS grades S390PM and S290PM exhibit remarkably high softening temperatures of ~530 and ~560 °C, respectively [36,37]. The difference in thermal stability can be attributed to their different alloy compositions, as summarized in Table 1. On the one hand, the S290PM exhibits a higher Co content, resulting in more pronounced solid solution strengthening of the matrix, as well as finer dispersed secondary hardening carbides and a reduced coarsening rate of these precipitates during overtempering [38,39]. On the other hand, the higher amounts especially of W and C in S290PM lead to a higher fraction of these secondary hardening carbides to be precipitated during tempering. HRC measurements in the as-coated state showed hardness values of 66 HRC for S390PM and 67 HRC for S290PM in the T_S range from 375 to 530 °C, respectively. After coating at the highest deposition temperature (575 °C), a slight drop in hardness of 2 HRC for S390PM and 1 HRC for S290PM was observed.

Table 1: Nominal compositions (given in wt.%) of the used PM-HSS substrates [36,37]

	C	Si	Mn	Cr	Mo	V	W	Co
S390PM	1.64	0.60	0.30	4.80	2.00	4.80	10.40	8.00
S290PM	2.00	0.50	0.30	3.80	2.50	5.10	14.30	11.00

3.2 Characterization of the as-deposited coatings

3.2.1 Coating adhesion, composition and thickness

All deposited coatings showed excellent adhesion on the PM-HSS substrates with HF 1 in the VDI Rockwell indentation test, irrespective of the substrate temperature. The overall chemical composition of the coatings as determined by EDX was also unaffected by T_S. With 48 at.% N, the coatings reached nearly stoichiometric composition, while the Al/(Ti+Al) atomic ratio was 0.61. The coating thickness shows a clear trend to higher values with increasing deposition temperature. The smallest value of 4.6 µm was measured after deposition at 420 °C, whereas 5.6 µm were reached at 575 °C. This rise in coating thickness could be a result of an increased sputter rate due to a less pronounced nitride mode in sputtering [40] at higher chamber temperatures. There, the N_2 flow at a substrate temperature of $T_S = 575$ °C was by 4.4% lower compared to $T_S = 375$ °C, as it was regulated to achieve a predetermined total pressure at constant noble gas flows (cf. section 2.1).

3.2.2 Coating microstructure

The XRD investigations show that the coatings crystallized in the face-centred cubic (fcc) structure for all deposition temperatures. No signs for the formation of the thermodynamically stable w-AlN [41] in addition to the metastable c-$Ti_{1-x}Al_xN$ solid solution, where c-AlN substitutes for a fraction of c-TiN [42], could be observed. In Fig. 1, the GIXRD patterns for the coatings deposited on S290PM are summarized. The standard positions for c-TiN and c-AlN [41] are marked by dashed lines. Besides a slight asymmetry of the peaks, no indication for the presence of TiN layers in the coatings can be found, which is in agreement with Chen et al. [22]. This can probably be attributed to the expectable higher thickness of the $Ti_{1-x}Al_xN$ layers compared to significantly thinner TiN layers, due to the lower sputtering power mentioned in section 2.1. Furthermore, slight intermixing between the layers due to energetic ion bombardment might occur [43], slightly contributing to the impediment of spinodal decomposition (see below) in addition to limited growth and diffusion conditions according to [1]. However, the diffractograms in Fig. 1 reveal an overall (111) peak width decrease with increasing T_S, corresponding to an increasing mean size of the diffracting domains [44]. Furthermore, the coatings tend to a preferred (111) orientation, while it gets clearly predominant especially at the highest substrate temperature of 575 °C where the (200) peak nearly disappears. It should be noted here that in the asymmetric GIXRD configuration, diffraction occurs on lattice planes which are not parallel to the sample surface [44]. Therefore, no direct conclusions on the coating texture can be drawn from GIXRD. Still, the same trends were also observed for XRD measurements performed in the symmetric Bragg-Brentano geometry (not shown here).

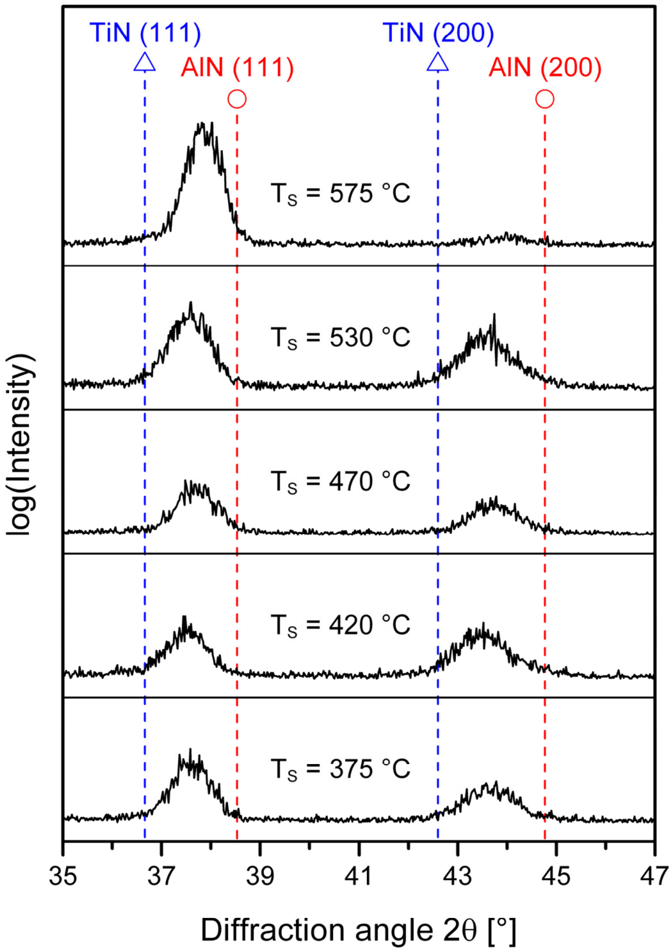

Fig. 1: GIXRD patterns of the as-deposited $Ti_{1-x}Al_xN$/TiN coatings on S290PM for different substrate temperatures T_S.

According to Chen et al. [45], the preferred (111) orientation obtained at $T_S = 575$ °C might result from the slightly lower N_2 flow mentioned in section 3.2.1. Moreover, the change in preferred orientation could also contribute to the increase in coating thickness with T_S. The adsorption energy of Ti on TiN (111) is three times higher compared to TiN (100) [46]. Consequently, the re-sputtering probability for Ti atoms from (111) oriented TiN grains should be lower than from (100) ones [47]. However, it is obvious that the

(111) peak of the coating deposited at 575 °C in Fig. 1 is slightly shifted towards higher diffraction angles. This is probably attributed to an altered macroscopic strain state [44] as the composition was constant for all substrate temperatures (cf. section 3.2.1). No significant influence of the two different PM-HSS substrates on the crystallographic properties of the films was detected as they exhibit similar microstructures, differing just in the quantitative phase fractions as mentioned earlier. Furthermore, XRD measurements indicated no noteworthy influence of the high deposition temperatures on the substrate materials.

To go into more detail, TEM investigations were performed on the $Ti_{1-x}Al_xN$/TiN multilayer coatings deposited on Si substrates at the lowest (375 °C) and the highest substrate temperature (575 °C). TEM bright-field cross-section images of the lamellae with the Si substrate visible at the left side are presented in Fig. 2. Both coatings show dense columnar zone T structures [24,25]. However, distinct differences in the microstructural evolution during coating growth are obvious. The coating deposited at 375 °C (Fig. 2 (a)) shows typical features of a pronounced initial competitive growth over the first ~500 nm, followed by another ~1.5 µm in which the growth competition proceeds in a less pronounced manner with V-shaped columns occasionally overgrowing each other. Thereafter, the coating microstructure becomes more regular with columns of more or less cylindrical shape. A multilayered $Ti_{1-x}Al_xN$/TiN coating structure can be identified, where the darker thin layers in the bright-field image correspond to the deposit stemming from the Ti target (i.e. more or less pure TiN). In general, the column boundaries are hardly visible, and the speckled contrast throughout the coating as well as within the columns indicates a mixed coating texture, which is in good agreement with the XRD results discussed before. Fig. 2 (b) shows the TEM micrograph of the lamella sampled from the coating deposited at 575 °C. Here, the initial competitive growth stage seems to be overcome already after ~200 nm. Thereafter, a V-shaped structure rapidly evolves in pronounced parallel, nearly cylindrical columns, which are growing steadily throughout the whole coating thickness. In contrast to Fig. 2 (a), the column boundaries are clearly identifiable, the column diameter is distinctly higher, and the multilayered structure appears much more defined. Moreover, the multilayer stack shows increased layer periods, fostering the observed increase in coating thickness with increasing T_S (cf. section 3.2.1). The much more homogeneous contrast distribution in Fig. 2 (b) indicates a preferred coating orientation, which again is in perfect agreement with the XRD results as discussed initially.

(a) T_s = 375 °C

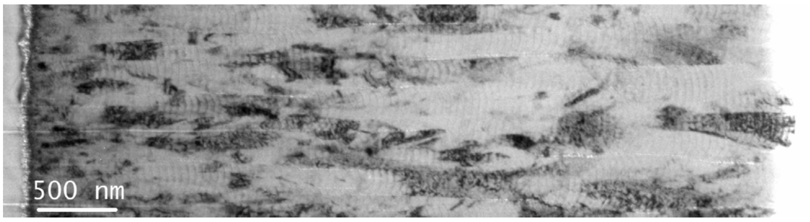

(b) T_s = 575 °C

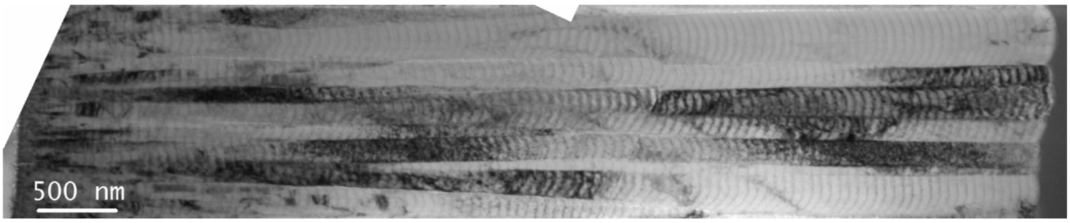

Fig. 2: Bright-field TEM cross-sections of the $Ti_{1-x}Al_xN$/TiN multilayer coatings deposited on Si substrates (left side) at substrate temperatures of (a) T_S = 375 °C and (b) T_S = 575 °C. The images were produced by stitching of neighbouring micrographs.

Fig. 3 shows EFTEM images of the same samples recorded with respect to the Ti $L_{2,3}$ edge (455.5 eV [48]) in the upper third of the coatings, i.e. the steady-state coating growth regime, at higher magnification. The microstructure of the coating deposited at 375 °C (Fig. 3 (a)) reveals columns which are slightly tilted with respect to each other, and their boundaries are kind of blurred. The multilayer structure can be identified with the bright layers corresponding to TiN. The coating deposited at 575 °C is shown in Fig. 3 (b), where it is obvious that the microstructure is characterized by thicker parallel columns with distinctly sharper boundaries. Additionally, the multilayer structure is built up by well defined layers with higher layer periods compared to T_S = 375 °C as already observed in Fig. 2. It could be speculated that the sharper layer interfaces cause an increased capability of the TiN layers to introduce in-plane tensile coherency stresses in the $Ti_{1-x}Al_xN$ layers, resulting in a slight decrease of the lattice parameter in growth direction, which would be in agreement with the observed (111) peak shift in combination with the slight asymmetry as observed in the GIXRD pattern for T_S = 575 °C (cf. Fig. 1). An additional contribution could stem from a slightly increased Al content on the metal sublattice of the $Ti_{1-x}Al_xN$ layers concomitant with the development of more immaculate TiN layers as a consequence of the high T_S and therefore enhanced growth and diffusion conditions. The observation of surface-initiated spinodal decomposition during ultra-high vacuum $Ti_{1-x}Al_xN$ growth in the temperature range of $540 \leq T_S \leq 560$ °C by Adibi et al. [49] would point towards this assumption. However, avoiding speculations, it can be stated that the coating deposited at T_S = 575 °C shows a more homogeneous microstructure with thicker parallel columns, sharper column boundaries and a well defined $Ti_{1-x}Al_xN$/TiN multilayer stack of higher layer periods compared to T_S = 375 °C.

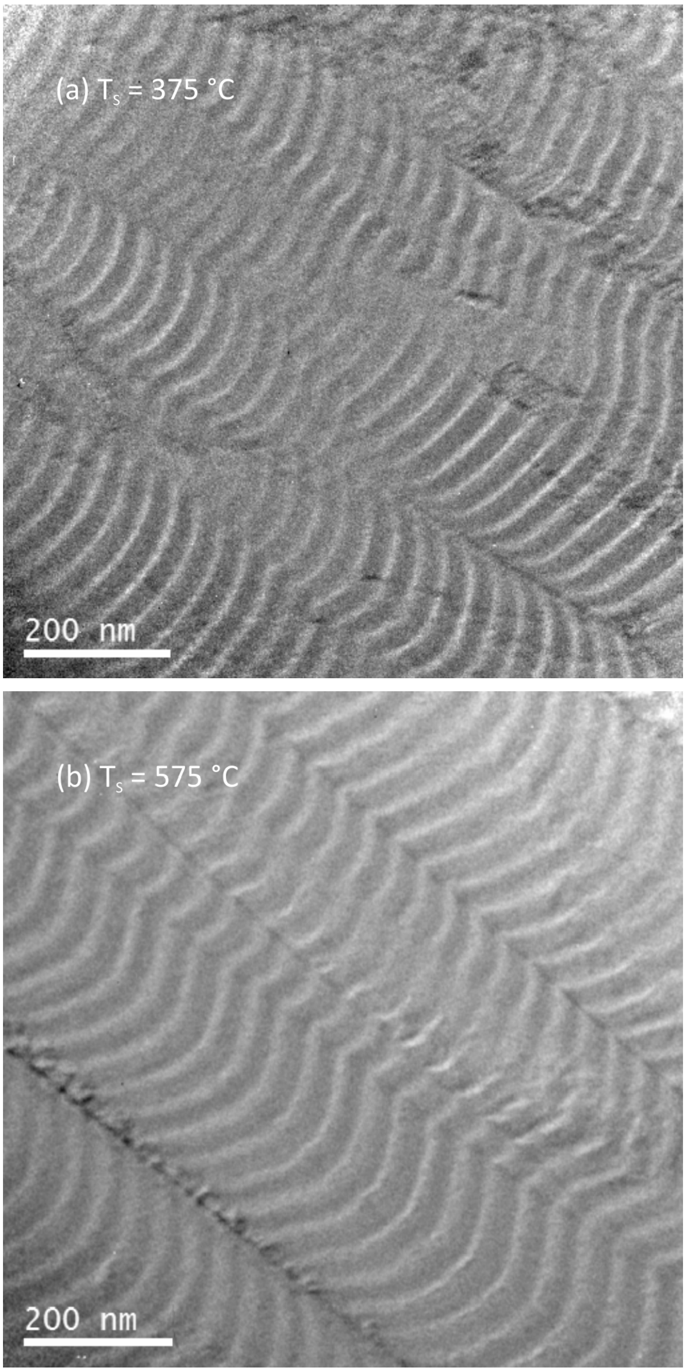

Fig. 3: EFTEM Ti mapping images of the $Ti_{1-x}Al_xN$/TiN multilayer coatings deposited on Si substrates at (a) T_S = 375 °C and (b) T_S = 575 °C.

3.2.3 Mechanical properties

The influence of increasing substrate temperatures on hardness and Young's modulus of the coatings is summarized in Fig. 4. The hardness slightly decreases from ~31 GPa in the range of 375-470 °C to ~30 GPa for T_S = 530 °C. At the highest substrate temperature of 575 °C, the hardness significantly increases to ~33.5 GPa. The Young's modulus evolution shows a similar behaviour, but the increase is already observable for T_S = 530 °C. The initial decrease in hardness and Young's modulus can most probably be attributed to the increase in domain size and bilayer period of the coatings as discussed in section 3.2.2 according to the Hall-Petch relation [50-52]. On the contrary, to obtain the highest hardness and Young's modulus for the coating deposited at the highest substrate temperature and therefore with the highest domain size is in clear contradiction to the Hall-Petch relation. Consequently, another strengthening mechanism overcoming the effect of coarsening domains must occur. It was shown in section 3.2.2, that the $Ti_{1-x}Al_xN$/TiN multilayer coatings deposited at 575 °C reveal both sharper column boundaries and sharper interfaces between the individual $Ti_{1-x}Al_xN$ and TiN layers in the multilayer structure. Therefore, although all investigated multilayer coatings are strengthened due to the Koehler effect [53,54], it will be significantly more pronounced for T_S = 575 °C, causing the increased mechanical properties illustrated in Fig. 4 despite increasing domain sizes. The indication for increased interfacial coherency strains in this coating as discussed in the previous section would further corroborate this implication.

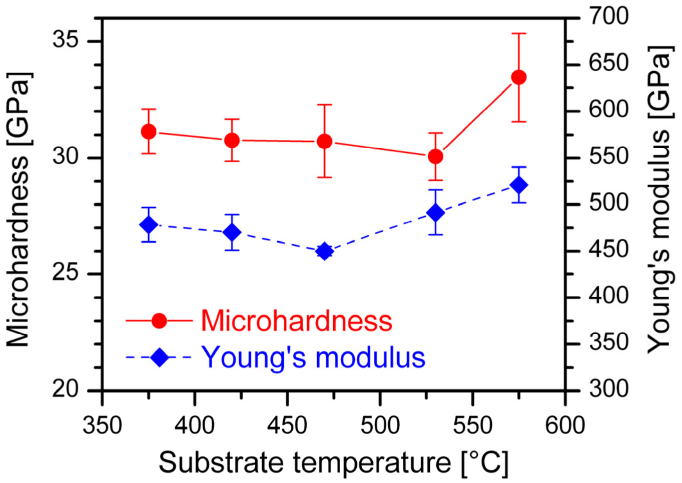

Fig. 4: Hardness and Young's modulus evolution of the as-deposited $Ti_{1-x}Al_xN$/TiN multilayer coatings on S290PM as a function of T_S.

Biaxial stress measurements showed minor tensile residual stresses in the $Ti_{1-x}Al_xN$/TiN multilayer coatings deposited on Si (100) ranging from about 100 MPa at the lowest to about 400 MPa at the highest deposition temperature. According to Daniel et al. [55,56], it may be assumed that these stress values mainly comprise an intrinsic and a thermal portion. Therefore, the thermal contribution stemming from the difference in thermal expansion coefficients α of the Si substrate and the coating material can be substituted for the thermal misfit stresses for coated PM-HSS substrates (assuming identical coating growth conditions) to get a rough estimate of the overall biaxial stresses of the $Ti_{1-x}Al_xN$/TiN coatings deposited on PM-HSS. Applying $\alpha_{Si} = 2.6 \cdot 10^{-6}\ K^{-1}$ [56], $\alpha_{S290PM} = 11 \cdot 10^{-6}\ K^{-1}$ [37] and assuming $\alpha_{coating} = 7.5 \cdot 10^{-6}\ K^{-1}$ [57] yields compressive residual stresses in the coatings on S290PM with about -1.8 GPa (T_S = 375 °C) and -2.9 GPa (T_S = 575 °C). It should be clearly pointed out here that $\alpha_{coating}$ will be influenced by the observed differences in coating microstructure (e.g. domain size and defect density). Nevertheless, it can be concluded that the coatings deposited on PM-HSS will significantly tend to compressive residual stresses, which will increase with T_S.

3.3 Thermal stability of the coatings

To gain information on the influence of T_S on the thermal stability of the metastable fcc $Ti_{1-x}Al_xN$/TiN coating material, Rietveld refinement was conducted on GIXRD patterns of as-deposited and vacuum annealed coatings on Si substrates. As an entire discussion of the Rietveld refinement results with respect to both five substrate temperatures T_S and five annealing conditions (as-deposited state and four annealing temperatures T_a) would burst the frame of this paper, the scope was mainly constrained to the evolutions of the constituent phase fractions as a function of T_a for different T_S, as summarized in Fig. 5. Furthermore, the mean lattice parameter development of these phases, which will surely be influenced by not further investigated lattice strains, is discussed. At this point it has to be clearly pointed out that in the present context the term *phase* is not equivalent with its original materials science meaning, implying e.g. a homogeneous and constant chemical composition [52]. In addition to microscopic growth-induced compositional fluctuations [3,10,26,49], the phases reported here reveal slight differences in the as-deposited lattice parameters and therefore potentially in the chemical composition, and they will furthermore undergo compositional changes during annealing due to diffusion processes in course of their spinodal decomposition [1,6,10]. However, in addition to the quantitative phase fractions and their lattice parameter evolution, a few values of the phases' average crystallite sizes (mainly of the as-deposited coatings) are also given. Comprehensive investigations on the thermally induced domain size and microstrain evolution of metastable cubic $Ti_{1-x}Al_xN$ coatings, both monolithic and multilayered with TiN, in course of their spinodal decomposition can be found in literature, e.g. [10-12,20,21,58], but it can be stated that the observed trends in crystallite size evolution in the present work are in reasonable qualitative agreement with the phenomena discussed in these references. However, as summarized at the left-hand side of the phase fraction diagrams in Fig. 5, the diffractograms of the as-deposited (a.d.) coatings could accurately be Rietveld refined for all substrate temperatures by introducing two cubic phases (space group 225 (Fm-3m) [41]). One (~59-68 wt.%) is more TiN-rich regarding the mean lattice parameter with an average diffracting domain size of ~15-20 nm, while the other (~32-41 wt.%) is more AlN-rich with larger domains of ~30-60 nm. Generally, the highest domain sizes, corresponding to the upper limits of the given ranges, were obtained for the T_S = 575 °C coating, which is in good agreement with the observations discussed in section 3.2.2.

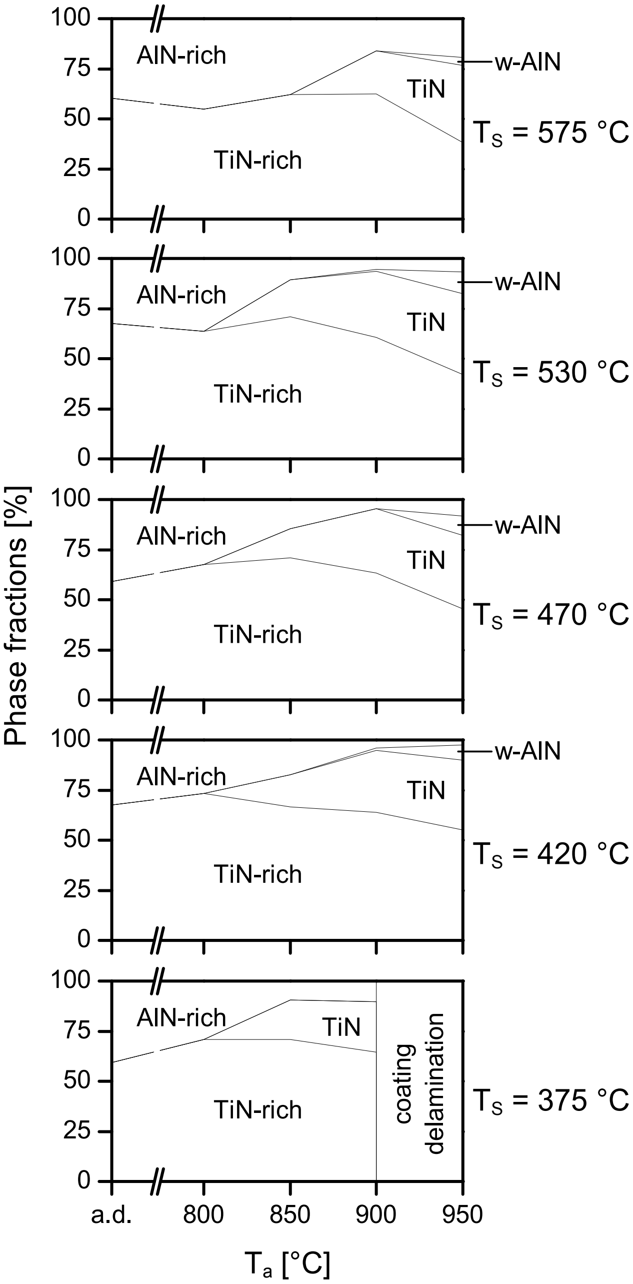

Fig. 5: Phase fraction diagrams of the $Ti_{1-x}Al_xN$/TiN coatings deposited on Si at different T_S as a function of the vacuum annealing temperature T_a (a.d.: as-deposited state) derived via Rietveld refinement of GIXRD data.

The TiN-rich phase revealed lattice constants of 4.10-4.14 Å, which is significantly lower compared to the reference value of 4.24 Å for pure TiN [41]. Also the AlN-rich phase exhibited low mean lattice parameters of 4.08-4.11 Å in the as-deposited state. The slight tensile residual in-plane stresses observed in section 3.2.3 could in part explain the relatively low lattice constants obtained from GIXRD measurements [44]. Vacuum annealing of the coatings at $T_a = 800$ °C for 10 min yielded slight changes in the quantitative fractions of the two phases (cf. Fig. 5). Furthermore, the average lattice constants slightly tend to decrease especially for the TiN-rich phase, most probably as a consequence of recovery processes [6]. In the coating deposited at $T_S = 470$ °C, the presence of more or less pure c-AlN is likely as the lattice parameter obtained for the AlN-rich phase exactly matches the reference value of 4.06 Å [41], while for the other coatings values of 4.07-4.11 Å were obtained. Consequently, first indications for spinodal decomposition are observable after vacuum annealing at 800 °C, in perfect agreement with literature [4,21,23]. For accurate Rietveld refinement of the diffractograms measured on coatings annealed at $T_a = 850$ °C, however, a third cubic (Fm-3m) phase needed to be introduced, indicating distinct progress in spinodal decomposition, except for the coating deposited at $T_S = 575$ °C. With lattice parameters of 4.22-4.23 Å, it seems justified to ascribe this third structure to more or less pure TiN [41]. As depicted in Fig. 5, the microstructure of the coating deposited at $T_S = 575$ °C consists of ~62 wt.% TiN-rich and ~38 wt.% AlN-rich domains, while in all other coatings ~15-20 wt.% of nanocrystalline (~4-5 nm) TiN domains emerge. These domains seem to develop at the expense of the AlN-rich crystallites (~9-17 wt.% remaining) in this T_a region, while the TiN-rich structure remains dominant with ~67-71 wt.%. Low lattice parameters were obtained for the coating deposited at $T_S = 575$ °C, where the AlN-rich phase can probably be attributed to c-AlN with 4.04 Å, which is even lower compared to [41]. The AlN-rich phase in the lower T_S coatings exhibits lattice constants of 4.08-4.09 Å. Consequently, the presence of rather pure c-AlN is expectable as well, while its coexistence with TiN would explain increased lattice constants due to coherency strains. After annealing at $T_a = 900$ °C, also the coating deposited at $T_S = 575$ °C exhibited 22 wt.% of nanocrystalline TiN growing at the expense of the AlN-rich phase, which decreases in fraction to 16 wt.%. In the coatings deposited at lower T_S, the amount of TiN increases to 25-33 wt.%, but in this case mostly at the expense of the TiN-rich phase. This seems plausible as the remaining 4-10 wt.% of AlN-rich phase can be regarded as c-AlN for $T_a \geq 850$ °C as discussed before. Furthermore, small fractions (~1 wt.%) of w-AlN (space group 186 (P63mc) [41]) were determined for $T_S = 420$ °C and $T_S = 530$ °C. In general, the TiN-rich phase is dominant with 61-64 wt.% for all coatings. The TiN phase exhibits lattice constants of 4.18-4.19 Å, while all other cubic lattice parameters are in the range of 4.07-4.09 Å. In course of the annealing treatment at $T_a = 950$ °C, the coating deposited at $T_S = 375$ °C delaminated from the Si substrate and was therefore not investigated. The coating delamination can be ascribed to the formation of excessive compressive stresses in the coating upon heating to 950 °C (i.e. 575 °C beyond T_S) as a result of the thermal mismatch between the coating and the substrate (cf. section 3.2.3) [59,60] and, moreover, the expectable formation of a distinct fraction of w-AlN with a ~20% higher unit cell volume compared to c-AlN [2,6,60-63]. However, the other coatings exhibit ~38-55 wt.% of the TiN-rich phase, while its fraction decreases with increasing T_S, and ~35-40 wt.% of TiN. For the coatings deposited at 420 °C ≤ T_S ≤ 530 °C, the AlN-rich phase fraction is low with ~2-8 wt.%, complemented by ~8-11 wt.% of w-AlN. The coating deposited at $T_S = 575$ °C reveals the highest content of remaining AlN-rich phase with ~20 wt.%, a TiN fraction increasing to ~38 wt.% at the expense of the TiN-rich phase (~38 wt.% remaining) and, most remarkable, the lowest w-AlN content of ~4 wt.%.

The mean lattice parameter derived from XRD peak fitting was shown to be a suitable indicator for the progress in isostructural spinodal decomposition of $Ti_{1-x}Al_xN$, as it shows a minimum where spinodal decomposition peaks [10,12]. As Rietveld refinement of the $Ti_{1-x}Al_xN$/TiN multilayer GIXRD patterns in this work yielded peak contributions of up to three cubic phases, the maximum lattice constant difference (MLCD) between these cubic constituents (i.e. between the AlN-rich and the TiN-rich phases in the two-phase regions in Fig. 5 or between the AlN-rich phase and TiN at higher T_a) in the individual as-deposited and annealed coatings depicted in Fig. 5 was calculated. For a clear visualisation of the evolving spinodal decomposition, these values were converted to a contour plot as a function of both substrate temperature T_S and annealing temperature T_a as shown in Fig. 6. The as-deposited (a.d.) coatings exhibit MLCDs of nearly 0.03 Å. The coating deposited at $T_S = 470$ °C attracts attention as necessary data binning uncovers that it is the only one exhibiting a MLCD slightly beyond 0.03 Å, while the lowest MLCD is obtained for $T_S = 575$ °C. Annealing at 800 °C yields MLCDs decreasing to about 0.02 Å for the coatings deposited at 375 °C ≤ T_S ≤ 530 °C, most probably due to defect annihilation and recovery processes [59] in combination with initial spinodal decomposition [7,10,21,23]. The lowest MLCD (slightly below 0.02 Å) was obtained for the $T_S = 375$ °C coating, as depicted in Fig. 6. The MLCD of the coating deposited at $T_S = 575$ °C, however, seems rather unaffected and even slightly increases compared to the as-deposited state (see the slight slope of the contour line near $T_a = 800$ °C in Fig. 6). Increasing T_a to 850 °C yields drastically increasing MLCDs with values of 0.14-0.15 Å for the coatings deposited at 375 °C ≤ T_S ≤ 530 °C due to the emergence of TiN (cf. Fig. 5). The MLCD of the coating deposited at $T_S = 575$ °C now decreases compared to its as-deposited state and

T_a = 800 °C, with 0.02 Å being significantly lower compared to the other coatings. After annealing at T_a = 900 °C, the coatings deposited at $T_S \leq 530$ °C reveal slightly decreasing MLCDs of about 0.11 Å. The significant MLCD increase due to the emergence of TiN as depicted in Fig. 5 can now also be observed for the coating deposited at T_S = 575 °C. The resultant MLCD peak value (0.12 Å) is distinctly lower compared to the other coatings, which is clearly observable in Fig. 6. After annealing at T_a = 950 °C, the MLCDs of the coatings deposited at 420 °C ≤ T_S ≤ 530 °C further relax to 0.08-0.09 Å, which can be attributed to the formation of a distinct amount of w-AlN. For the coating deposited at T_S = 575 °C, where only a minute amount of w-AlN was detected, a retarded response to thermal processing is obvious again with a MLCD remaining at nearly 0.11 Å.

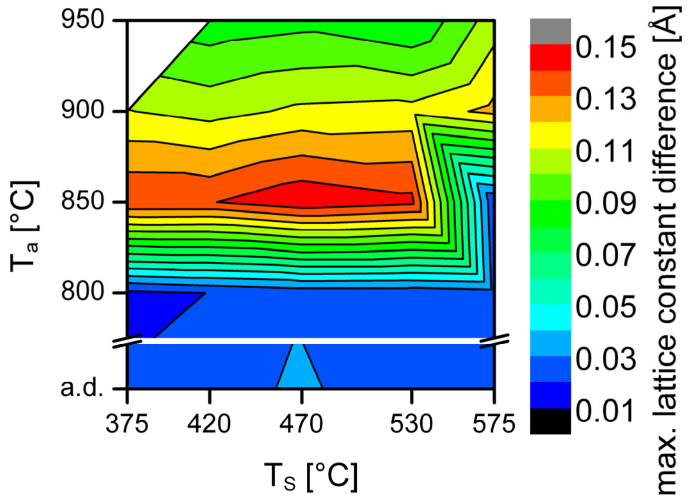

Fig. 6: Contour plot of the maximum lattice constant differences of the cubic constituents in the $Ti_{1-x}Al_xN$/TiN multilayer coatings on Si substrates as a function of T_S and T_a (a.d.: as-deposited state) determined by Rietveld refinement of GIXRD data.

Therefore, according to the phase fraction diagrams presented in Fig. 5 and the MLCD evolution summarized in Fig. 6, it can be stated that increasing T_S yield improved thermal stability, while the coating deposited at the lowest T_S (375 °C) even failed during the annealing treatment. The $Ti_{1-x}Al_xN$/TiN multilayer coating deposited at T_S = 575 °C, on the other hand, exhibits the highest thermal stability, as both the isostructural spinodal decomposition and the subsequent formation of w-AlN are delayed by ~50 °C compared to lower T_S. This can on one hand be explained by an increased resistance against defect annihilation and recovery with increasing T_S [59,64], which typically initiates ahead of spinodal decomposition [6,11,12,21,65]. On the other hand, also the observed increase in the as-deposited domain sizes will contribute. Spinodal decomposition in $Ti_{1-x}Al_xN$ as well as the subsequent w-AlN formation initiate at domain boundaries and interfaces [10,12,23,58,66]. Therefore, although a lower amount of these high diffusivity paths in the coating deposited at T_S = 575 °C delays the spinodal decomposition with its beneficial age-hardening effect [6], the detrimental w-AlN formation is retarded as well. Furthermore, although indications for the afore development of the AlN-rich phase to more or less pure c-AlN were partly observed, it is noteworthy that the formation of TiN evidently plays a crucial role in course of the isostructural decomposition of the $Ti_{1-x}Al_xN$/TiN multilayer coatings under investigation. Commonly, the emergence of c-AlN domains embedded in a TiN-rich matrix was observed [1,2,4,6,10,20]. Though, spinodal decomposition of monolithic c-$Ti_{1-x}Al_xN$ via TiN formation was also reported in Refs. [9,12], where the investigated coatings were synthesized under similar growth conditions using industrial-scale sputtering systems. Rovere et al. [9] observed asymmetric XRD peak broadening to the TiN-rich side after annealing of powdered coating material. Schalk et al. [12] reported the formation of more volume consuming TiN during spinodal decomposition of $Ti_{1-x}Al_xN$ coatings under tensile residual stresses in the as-deposited state on Si substrates. For the coatings investigated here, it can be assumed that the tensile stresses in $Ti_{1-x}Al_xN$ at the interfaces to TiN in the multilayer structure foster TiN formation [23] in addition to the slight tensile residual stresses in the as-deposited state (cf. section 3.2.3) for the same reason. However, the MLCD maxima for different T_S in Fig. 6, which understandably coincide with the emergence of TiN in Fig. 5, and therefore the summits in spinodal decomposition occur at T_a = 850 °C ($T_S \leq$ 530 °C) or are retarded to T_a = 900 °C (T_S = 575 °C), agreeing well with literature [7,12,21,23]. Summarizing the conducted thermal stability investigations, it can be stated that the substrate temperature during coating deposition is a considerably important parameter for tailoring the thermal response of multilayered $Ti_{1-x}Al_xN$/TiN coatings (and certainly of monolithic $Ti_{1-x}Al_xN$ as well).

3.4 Tribological performance

Tribological tests further corroborated the beneficial effect of increased deposition temperatures on the wear resistance of $Ti_{1-x}Al_xN$/TiN multilayer coatings. The tribological investigations were performed on coatings deposited on PM-HSS samples, which are assumed to exhibit distinct compressive residual stresses in the as-deposited state as calculated in section 3.2.3. According to Alling et al. [8], these stresses could further enhance the performance of the $Ti_{1-x}Al_xN$/TiN multilayer coatings at elevated testing temperatures, in addition to the already promising thermal stability of the coatings deposited on Si substrates demonstrated in section 3.3. Still, there is an additional deciding factor for the wear performance of coated HSS samples, namely the hot hardness of the substrate material. As mentioned before, the PM-HSS grades S390PM and S290PM exhibit softening temperatures of ~530 °C and ~560 °C, respectively [36,37]. Consequently, the S390PM softens more distinctively than the S290PM during coating at 575 °C, which was confirmed by hardness measurements. Additional softening of the substrates is expected to arise from tribological testing at 560 °C and 650 °C. Matthews et al. [67] found six factors to limit the load bearing capacity of coated surfaces: Coating fracture, coating debonding, substrate elastic deformation, substrate plastic deformation, substrate fracture and ploughing friction. Accordingly, the substrate's response to the applied tribological load has an important influence on the wear performance, which could be corroborated in the present work.

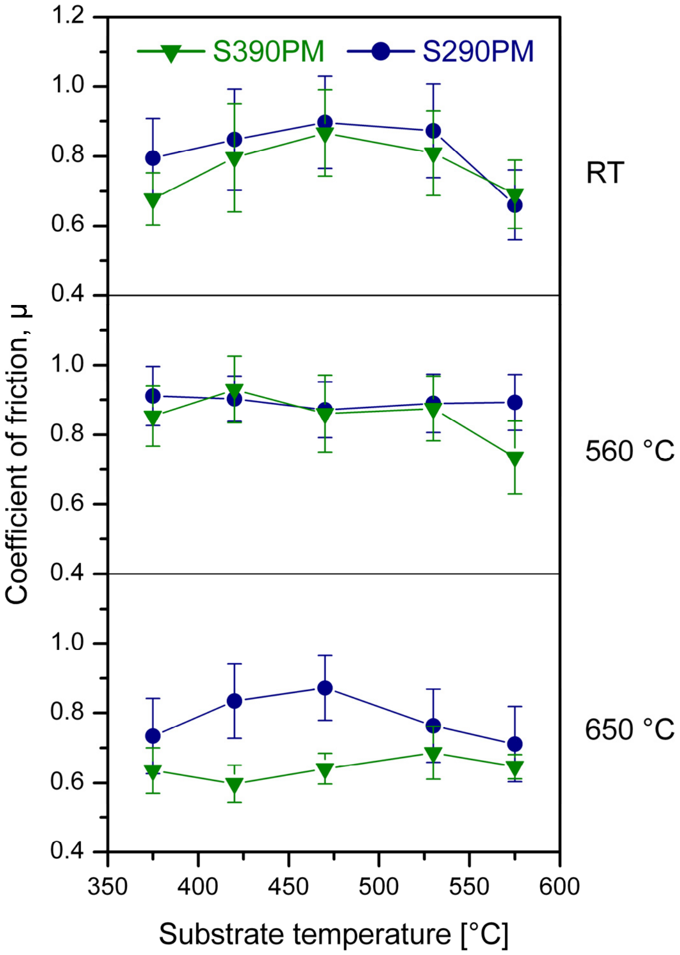

Fig. 7: Mean friction coefficients of the $Ti_{1-x}Al_xN/TiN$ multilayer coatings on S390PM and S290PM tested against alumina balls at room temperature (RT), 560 °C and 650 °C as a function of T_S.

The measured friction curves show steady-state behaviour after a short running-in period of about 20-40 m. Therefore, the first 50 m of the sliding distance were omitted for the calculation of the arithmetic mean and the standard deviation of the friction coefficient µ for each friction curve. To visualize expectable influences of the hot hardness of the substrate materials on the tribological properties of the coating systems, these values were plotted versus T_S for all testing temperatures in Fig. 7. In addition, Fig. 8 gives a representative overview of two-dimensional wear track cross-sections to illustrate the wear performance as well as the occurring wear mechanisms.

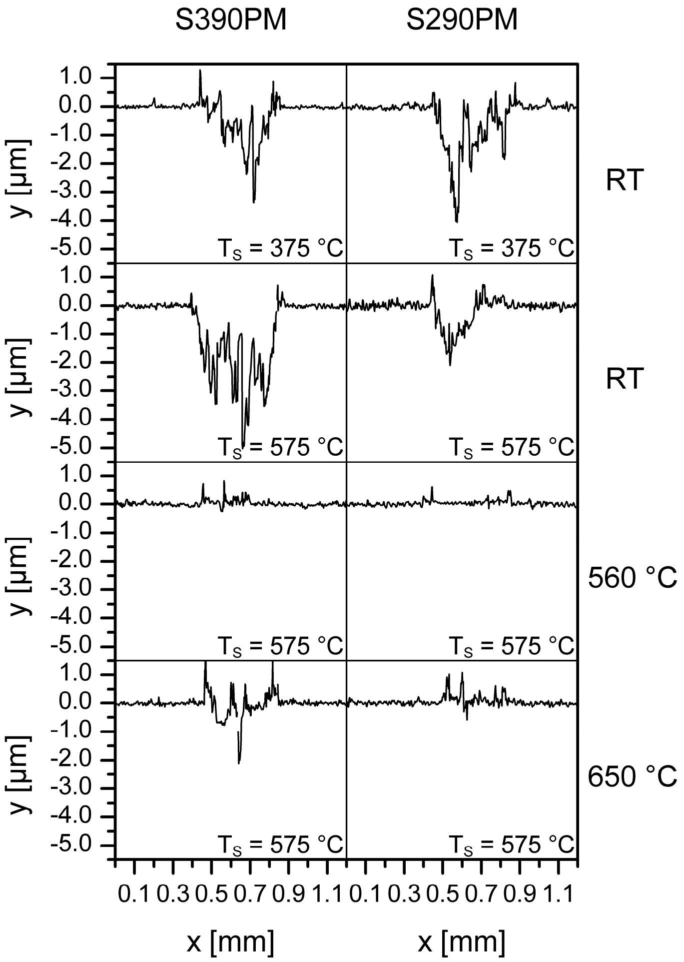

Fig. 8: Two-dimensional profiles of the investigated wear tracks in the $Ti_{1-x}Al_xN/TiN$ multilayer coatings deposited on S390PM (left column) and S290PM (right column) at $T_S = 375$ °C (first row) and $T_S = 575$ °C (second to fourth row) from tribological tests against alumina balls at RT, 560 °C and 650 °C.

At RT, µ is in the range of ~0.8-0.9 for all coating systems with $T_S \leq 530$ °C, except for the coating deposited on S390PM at $T_S = 375$ °C. Apart from that, the lowest values of $\mu \leq 0.7$ were measured on the $Ti_{1-x}Al_xN/TiN$ coatings deposited at $T_S = 575$ °C. Regarding the coating deposited on S290PM, the low µ comes along with an increased wear resistance. A wear rate decrease from $K = 6.5 \cdot 10^{-15}$ m^3/Nm for $T_S = 375$ °C to $K = 5.7 \cdot 10^{-15}$ m^3/Nm was obtained. According to Fig. 8, the dominating wear mechanism at RT is abrasion. Therefore, it can be speculated that the enhanced mechanical properties achieved at $T_S = 575$ °C (cf. Fig. 4) yield the increased wear resistance of the $Ti_{1-x}Al_xN/TiN$ coating deposited on S290PM, which could also explain the low friction coefficient of this sample. Higher wear resistance and consequently minor formation of wear debris results in less pronounced energy loss in relative motion and, therefore, in a lower friction coefficient [68]. However, the opposite trend can be detected for the $Ti_{1-x}Al_xN$ coatings on S390PM, which can be attributed to the already mentioned slight decrease in substrate hardness during deposition (cf. section 3.1), resulting in more pronounced deformation of the substrate under tribological load. Although this higher elastic substrate deformation yields a similarly low μ as for the coating on S290PM, more tribological load has to be carried by the film, resulting in a wear rate increase from $K = 3.9 \cdot 10^{-15}$ m^3/Nm for the lowest to $K = 5.8 \cdot 10^{-15}$ m^3/Nm for the highest T_S.

Tribological tests at 560 °C yielded friction coefficients of ~0.9, except for the coating deposited on S390PM at 575 °C, where $\mu \approx 0.7$ (see Fig. 7). It can be deduced from Fig. 8 that adhesion and to a lesser extent abrasion are the dominating wear mechanisms at 560 °C. The coating deposited on S290PM at 575 °C exhibits hardly observable transfer material and abrasion grooves ($K = 2.2 \cdot 10^{-16}$ m^3/Nm), while the coating on S390PM shows somewhat more distinct traces of adhesion and abrasion ($K = 3.0 \cdot 10^{-16}$ m^3/Nm). This difference can be attributed to the lower thermal stability of the S390PM substrates, resulting in a drop in hardness during deposition as well as during tribological testing and, consequently, in increased wear. Deformation of the S390PM substrate under tribological load would again be a reasonable explanation for the obtained low friction coefficient. The lowest wear rate of $1.7 \cdot 10^{-16}$ m^3/Nm was obtained on S390PM coated at $T_S = 375$ °C. However, the beneficial effect of the highest T_S on the coating properties is affirmed by the wear rates measured on coated S290PM samples, which decrease from $3.2 \cdot 10^{-16}$ m^3/Nm at $T_S = 375$ °C to $2.2 \cdot 10^{-16}$ m^3/Nm at $T_S = 575$ °C.

At 650 °C, friction coefficients of $\mu \approx 0.6$-0.7 were obtained for coated S390PM specimen, while the coated S290PM samples exhibit $\mu \approx 0.7$-0.9 (see Fig. 7). As obvious in Fig. 8, adhesion and abrasion are again the dominating wear mechanisms, but they are more pronounced compared to 560 °C. The rise in abrasive wear can on the one hand be attributed to oxidation and wear debris formation resulting in three-body abrasion [67]. On the other hand, the high testing temperature leads to recognizable softening of the S290PM as well as considerable overaging of the S390PM substrates, which results in a decreased tribological load bearing capacity as mentioned before. Accordingly, while wear rates of the coated S290PM samples still decrease significantly from $6.2 \cdot 10^{-16}$ m^3/Nm ($T_S = 375$ °C) to $3.5 \cdot 10^{-16}$ m^3/Nm ($T_S = 575$ °C), the wear rates measured on S390PM coated at 375 °C and 575 °C are nearly identical and distinctly higher with $1.1 \cdot 10^{-15}$ m^3/Nm and $1.2 \cdot 10^{-15}$ m^3/Nm, respectively. The friction coefficients point towards the influence of the overaged substrate materials as well. Although at 650 °C the amount of wear debris in the tribological contact is unambiguously higher than at 560 °C (Fig. 8), the measured friction coefficients are lower especially for the coated S390PM samples. This could again be an indicator for elastic deformation of the overaged substrate materials under tribological load, resulting in decreased energy loss in the tribological contact and, therefore, in decreased friction. Obviously, the substrate's hot hardness seems to be a major factor for the wear resistance of the coating systems, which can especially be seen for the $Ti_{1-x}Al_xN$/TiN multilayer coated S390PM.

To illustrate the influence of elevated deposition temperatures combined with substrate materials of different thermal stability on the wear resistance of the coating systems, the wear rates determined in tribological tests at different testing temperatures are presented in Fig. 9 for the coatings deposited at the lowest (375 °C) and the highest T_S (575 °C). Note the different scales used for RT and elevated testing temperatures. The wear coefficients at RT show relatively high scattering, which can probably be related to distinct wear debris formation through abrasion, which was found to be the dominating wear mechanism at RT (cf. Fig. 8). However, the enhanced mechanical properties and thermal stability of the $Ti_{1-x}Al_xN$/TiN multilayer coatings deposited on S290PM at T_S = 575 °C obviously yield increased wear resistance compared to T_S = 375 °C. On the other hand, the lower hot hardness of the S390PM substrates yields increased wear rates at T_S = 575 °C in spite of the promising coating properties, as elastic deformation of the weakened substrate material reduces the tribological load bearing capacity of the coating system. Similar trends can be observed for the tribological tests performed at 560 °C. At the highest testing temperature of 650 °C, however, the S390PM substrate gets sufficiently overaged that the consequent substrate deformation dominates the wear performance. Consequently, the wear rates obtained for the lowest and the highest T_S are almost equal and quite high. Contrarily, the less overaged S290PM substrate still provides enough support for the $Ti_{1-x}Al_xN$/TiN multilayer coating, so that the enhanced coating properties obtained at T_S = 575 °C dominate, yielding a significantly lower wear rate compared to T_S = 375 °C.

Summarizing the conducted tribological tests, it can be stated that the enhanced mechanical properties and thermal stability of the $Ti_{1-x}Al_xN$/TiN multilayer coatings deposited at T_S = 575 °C yield distinctly improved wear performance. However, an adequate hot hardness of the substrate material is an essential prerequisite.

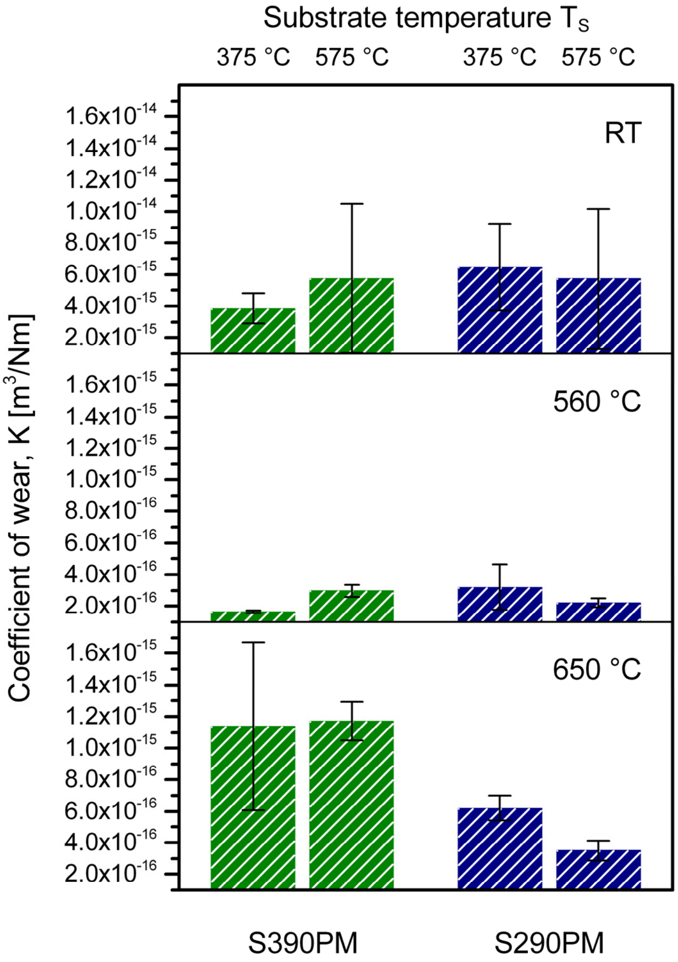

Fig. 9: Wear coefficients of the $Ti_{1-x}Al_xN/TiN$ multilayer coatings deposited on S390PM and S290PM at $T_S = 375$ °C and $T_S = 575$ °C measured after tribological testing against alumina balls at room temperature (RT), 560 °C and 650 °C. Note the different scales used for RT and elevated testing temperatures.

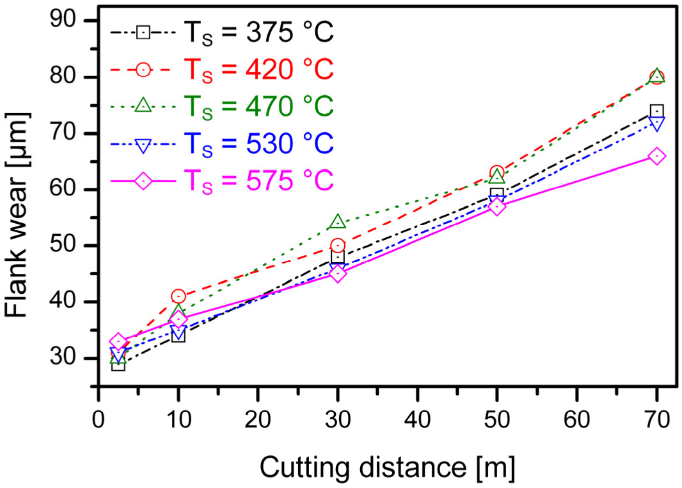

Fig. 10: Summary of the cutting tests conducted on cold work steel 1.2312 with S290PM end mills coated with $Ti_{1-x}Al_xN/TiN$ multilayer films at different T_S.

The conducted cutting tests further corroborate the positive influence of increased T_S on the wear performance of $Ti_{1-x}Al_xN/TiN$ multilayer coatings as summarized in Fig. 10. Coated S290PM end mills exhibited enhanced flank wear resistance especially in the second half of the cutting distance. Surprisingly, tools coated at 375 °C show better wear resistance than the samples coated at 420 °C and 470 °C, respectively. However, most noteworthy, compared to the results for T_S = 420 °C, the end mills coated at 575 °C show an increase in cutting distance of about 40%.

4. Conclusions

Elevated deposition temperatures yielded a beneficial effect on the mechanical properties of sputtered $Ti_{1-x}Al_xN/TiN$ multilayer coatings deposited on PM-HSS and Si substrates in spite of a distinct rise in domain sizes observed for the highest substrate temperature, which is due to the development of sharper domain boundaries and multilayer interfaces. Both increasing resistance against defect annihilation during annealing and rising domain sizes enhance the thermal stability regarding spinodal decomposition of metastable fcc $Ti_{1-x}Al_xN$. Consequently, the $Ti_{1-x}Al_xN/TiN$ multilayer coating deposited at the highest substrate temperature exhibits the highest hardness in the as-deposited state and a by 50 °C retarded onset of the detrimental wurtzite AlN formation subsequent to the isostructural phase separation. Provided that the PM-HSS substrate material exhibits sufficient hot hardness and thus mechanical support, these enhanced coating properties yield superior wear performance in both laboratory-scale tribological investigations and industrially relevant cutting tests, where an enhancement in tool lifetime of about 40% was demonstrated.

Acknowledgements

This work was done within the Research Studio Austria energy-drive, with financial support from the Österreichische Forschungsförderungsgesellschaft and the Bundesministerium für Wirtschaft, Familie und Jugend. The authors gratefully acknowledge valuable discussions on TEM with Dr. B. Rashkova and on tribological phenomena with Dr. G.A. Fontalvo.

References

[1] A. Hörling, L. Hultman, M. Odén, J. Sjölén, L. Karlsson, J. Vac. Sci. Technol. A 20 (5) (2002) 1815.

[2] A. Hörling, L. Hultman, M. Odén, J. Sjölén, L. Karlsson, Surf. Coat. Technol. 191 (2-3) (2005) 384.

[3] R. Rachbauer, E. Stergar, S. Massl, M. Moser, P.H. Mayrhofer, Scr. Mater. 61 (7) (2009) 725.

[4] I.A. Abrikosov, A. Knutsson, B. Alling, F. Tasnádi, H. Lind, L. Hultman, M. Odén, Materials 4 (9) (2011) 1599.

[5] A. Knutsson, J. Ullbrand, L. Rogström, N. Norrby, L.J.S. Johnson, L. Hultman, J. Almer, M.P. Johansson Jöesaar, B. Jansson, M. Odén, J. Appl. Phys. 113 (21) (2013) 213518.

[6] P.H. Mayrhofer, A. Hörling, L. Karlsson, J. Sjölén, T. Larsson, C. Mitterer, L. Hultman, Appl. Phys. Lett. 83 (10) (2003) 2049.

[7] P.H. Mayrhofer, F.D. Fischer, H.J. Böhm, C. Mitterer, J.M. Schneider, Acta Mater. 55 (4) (2007) 1441.

[8] B. Alling, M. Odén, L. Hultman, I.A. Abrikosov, Appl. Phys. Lett. 95 (18) (2009) 181906.

[9] F. Rovere, D. Music, S. Ershov, M. to Baben, H.G. Fuss, P.H. Mayrhofer, J.M. Schneider, J. Phys. D: Appl. Phys. 43 (3) (2010) 035302.

[10] R. Rachbauer, S. Massl, E. Stergar, D. Holec, D. Kiener, J. Keckes, J. Patscheider, M. Stiefel, H. Leitner, P.H. Mayrhofer, J. Appl. Phys. 110 (2) (2011) 023515.

[11] L. Rogström, J. Ullbrand, J. Almer, L. Hultman, B. Jansson, M. Odén, Thin Solid Films 520 (17) (2012) 5542.

[12] N. Schalk, C. Mitterer, J. Keckes, M. Penoy, C. Michotte, Surf. Coat. Technol. 209 (2012) 190.

[13] A. Knutsson, M.P. Johansson, L. Karlsson, M. Odén, Surf. Coat. Technol. 205 (16) (2011) 4005.

[14] L. Chen, S.Q. Wang, Y. Du, S.Z. Zhou, T. Gang, J.C. Fen, K.K. Chang, Y.W. Li, X. Xiong, Surf. Coat. Technol. 205 (2) (2010) 582.

[15] H. Lind, R. Forsén, B. Alling, N. Ghafoor, F. Tasndi, M.P. Johansson, I.A. Abrikosov, M. Odén, Appl. Phys. Lett. 99 (9) (2011) 091903.

[16] L. Chen, D. Holec, Y. Du, P.H. Mayrhofer, Thin Solid Films 519 (16) (2011) 5503.

[17] R. Rachbauer, A. Blutmager, D. Holec, P.H. Mayrhofer, Surf. Coat. Technol. 206 (10) (2012) 2667.

[18] R. Rachbauer, D. Holec, P.H. Mayrhofer, Surf. Coat. Technol. 211 (2012) 98.

[19] D. Holec, L. Zhou, R. Rachbauer, P.H. Mayrhofer, J. Appl. Phys. 113 (11) (2013) 113510.

[20] A. Knutsson, M.P. Johansson, P.O.Å. Persson, L. Hultman, M. Odén, Appl. Phys. Lett. 93 (14) (2008) 143110.

[21] A. Knutsson, M.P. Johansson, L. Karlsson, M. Odén, J. Appl. Phys. 108 (4) (2010) 044312.

[22] L. Chen, Y. Du, X. Xiong, K.K. Chang, M.J. Wu, Int. J. Refract. Met. Hard Mater. 29 (6) (2011) 681.

[23] A. Knutsson, I.C. Schramm, K. Asp Grönhagen, F. Mücklich, M. Odén, J. Appl. Phys. 113 (11) (2013) 114305.

[24] J.A. Thornton, Ann. Rev. Mater. Sci. 7 (1977) 239.

[25] P.B. Barna, M. Adamik, Thin Solid Films 317 (1-2) (1998) 27.

[26] L.J.S. Johnson, M. Thuvander, K. Stiller, M. Odén, L. Hultman, Thin Solid Films 520 (13) (2012) 4362.

[27] N. Schalk, T. Weirather, C. Polzer, P. Polcik, C. Mitterer, Surf. Coat. Technol. 205 (19) (2011) 4705.

[28] H. Jensen, J. Sobota, G. Sorensen, J. Vac. Sci. Technol. A 15 (3) (1997) 941.

[29] J. Neidhardt, M. O'Sullivan, A.E. Reiter, W. Rechberger, W. Grogger, C. Mitterer, Surf. Coat. Technol. 201 (6) (2006) 2553.

[30] J. Neidhardt, S. Mráz, J.M. Schneider, E. Strub, W. Bohne, B. Liedke, W. Möller, C. Mitterer, J. Appl. Phys. 104 (6) (2008) 063304.

[31] T. Weirather, C. Czettl, P. Polcik, M. Kathrein, C. Mitterer, Surf. Coat. Technol. 232 (2013) 303.

[32] H.-R. Stock, A. Schulz, W. Ensinger, J. Güttler, E. Fromm, D. Müller, W.D. Busch, H. Grützner, in: H. Jehn, G. Reiners, N. Siegel (Eds.), DIN Fachbericht 39, Beuth Verlag, Berlin, 1993, pp. 210-234.

[33] W.C. Oliver, G.M. Pharr, J. Mater. Res. 7 (6) (1992) 1564.

[34] G.G. Stoney, Proc. R. Soc. London A 82 (553) (1909) 172.

[35] W.D. Nix, Metall. Trans. A 20 (11) (1989) 2217.

[36] Böhler Edelstahl GmbH & Co KG, Böhler S390 Microclean, http://www.bohler-edelstahl.com/files/S390DE.pdf, August 2013.

[37] Böhler Edelstahl GmbH & Co KG, Böhler S290 Microclean, http://www.bohler-edelstahl.com/files/S290DE.pdf, August 2013.

[38] H.F. Fischmeister, S. Karagöz, H.O. Andrén, Acta Metall. 36 (4) (1988) 817.

[39] S. Karagöz, H.O. Andrén, Z. Metallkd. 83 (6) (1992) 386.

[40] D. Güttler, B. Abendroth, R. Grötzschel, W. Möller, D. Depla, Appl. Phys. Lett. 85 (25) (2004) 6134.

[41] ICDD International Center for Powder Diffraction Data, Powder Diffraction File (Card 00-038-1420 for c-TiN, Card 00-046-1200 for c-AlN, Card 00-025-1133 for w-AlN), PDF-2/Release 2007.

[42] P.H. Mayrhofer, C. Mitterer, H. Clemens, Adv. Eng. Mater. 7 (12) (2005) 1071.

[43] H. Meidia, A.G. Cullis, C. Schönjahn, W.D. Münz, J.M. Rodenburg, Surf. Coat. Technol. 151-152 (2002) 209.

[44] M. Birkholz, P.F. Fewster, C. Genzel, Thin Film Analysis by X-ray Scattering, Wiley-VCH, Weinheim, 2006.

[45] L. Chen, M. Moser, Y. Du, P.H. Mayrhofer, Thin Solid Films 517 (24) (2009) 6635.

[46] D. Gall, S. Kodambaka, M.A. Wall, I. Petrov, J.E. Greene, J. Appl. Phys. 93 (11) (2003) 9086.

[47] P.H. Mayrhofer, M. Geier, C. Löcker, L. Chen, Int. J. Mater. Res. 100 (8) (2009) 1052.

[48] D.R. Lide, CRC Handbook of Chemistry and Physics, 85th ed., CRC Press, Boca Raton, FL, 2004.

[49] F. Adibi, I. Petrov, L. Hultman, U. Wahlström, T. Shimizu, D. McIntyre, J.E. Greene, J.E. Sundgren, J. Appl. Phys. 69 (9) (1991) 6437.

[50] E.O. Hall, Proc. Phys. Soc. London Sect. B 64 (9) (1951) 747.

[51] N.J. Petch, J. Iron Steel Inst. 174 (1953) 25.

[52] W.D. Callister, Materials Science and Engineering: An Introduction, 6th ed., John Wiley & Sons, New York, 2003.

[53] J.S. Koehler, Phys. Rev. B 2 (2) (1970) 547.

[54] L. Hultman, C. Engström, M. Odén, Surf. Coat. Technol. 133-134 (2000) 227.

[55] R. Daniel, D. Holec, M. Bartosik, J. Keckes, C. Mitterer, Acta Mater. 59 (17) (2011) 6631.

[56] R. Daniel, K.J. Martinschitz, J. Keckes, C. Mitterer, Acta Mater. 58 (7) (2010) 2621.

[57] D.Y. Wang, C.L. Chang, K.W. Wong, Y.W. Li, W.Y. Ho, Surf. Coat. Technol. 120-121 (1999) 388.

[58] M. Odén, L. Rogström, A. Knutsson, M.R. Terner, P. Hedström, J. Almer, J. Ilavsky, Appl. Phys. Lett. 94 (5) (2009) 053114.

[59] C. Mitterer, P.H. Mayrhofer, J. Musil, Vacuum 71 (1-2) (2003) 279.

[60] P.H. Mayrhofer, C. Mitterer, L. Hultman, H. Clemens, Prog. Mater. Sci. 51 (8) (2006).

[61] N.E. Christensen, I. Gorczyca, Phys. Rev. B 47 (8) (1993) 4307.

[62] Q. Xia, H. Xia, A.L. Ruoff, J. Appl. Phys. 73 (12) (1993) 8198.

[63] Q. Li, I.W. Kim, S.A. Barnett, L.D. Marks, J. Mater. Res. 17 (5) (2002) 1224.

[64] L. Hultman, Vacuum 57 (1) (2000) 1.

[65] R. Forsén, M. Johansson, M. Odén, N. Ghafoor, J. Vac. Sci. Technol. A 30 (6) (2012) 061506.

[66] D.J. Seol, S.Y. Hu, Y.L. Li, J. Shen, K.H. Oh, L.Q. Chen, Acta Mater. 51 (17) (2003) 5173.

[67] A. Matthews, S. Franklin, K. Holmberg, J. Phys. D: Appl. Phys. 40 (18) (2007) 5463.

[68] N.P. Suh, H.-C. Sin, Wear 69 (1) (1981) 91.

Publication III

Industrial-scale sputter deposition of $Cr_{1-x}Al_xN$ coatings with $0.21 \leq x \leq 0.74$ from segmented targets

T. Weirather, C. Czettl, P. Polcik, M. Kathrein, C. Mitterer

Surface and Coatings Technology 232 (2013) 303-310

Industrial-scale sputter deposition of $Cr_{1-x}Al_xN$ coatings with $0.21 \le x \le 0.74$ from segmented targets

T. Weirather[a], C. Czettl[b], P. Polcik[c], M. Kathrein[b], C. Mitterer[a]

[a] Department of Physical Metallurgy and Materials Testing, Montanuniversität Leoben,
Franz-Josef-Straße 18, 8700 Leoben, Austria

[b] CERATIZIT Austria GmbH, Metallwerk-Plansee-Straße 71, 6600 Reutte, Austria

[c] PLANSEE Composite Materials GmbH, Siebenbürgerstraße 23, 86983 Lechbruck am See,
Germany

Abstract

This study introduces novel triangle-like segmented targets for industrial-scale sputtering systems, which enable to distinctly reduce the workload in economic coating material development. Al, Cr and Cr/Al 50/50 target segments were assembled pairwise to synthesize $Cr_{1-x}Al_xN$ hard coatings in the range of $0.21 \le x \le 0.74$ at a high compositional resolution within two deposition runs. The obtained coating compositions are supported with TRIM simulations showing distinct differences in the sputtering characteristics of Al and Cr. X-ray diffraction reveals a solubility limit of $x = 0.61$ in cubic $Cr_{1-x}Al_xN$. The evolution of structural and mechanical properties with composition is discussed in detail. The high potential and industrial relevance of the coatings with a maximum hardness of 25.2 GPa is corroborated by excellent tribological properties with low friction values down to 0.4 and wear coefficients down to $1.8 \cdot 10^{-16}$ m^3/Nm.

Keywords: Magnetron sputtering, segmented targets, CrAlN coatings, XRD, nano-indentation, tribology

1. Introduction

Coating material development is both time and money consuming. Already for binary hard coatings like CrN synthesized via physical vapour deposition (PVD) techniques like reactive magnetron sputtering, several deposition runs need to be performed to evaluate the effects of e.g. varying plasma characteristics at different reactive gas partial pressures [1]. With the invention of ternary transition metal aluminium nitrides [2], the workload in coating material development further increased drastically, as the beneficial properties of these coatings strongly depend on the AlN content in the metastable solid solutions [3-5]. Furthermore, different transition metal nitrides exhibit different solubility limits for AlN [6], where the face-centered cubic (fcc) crystal structure desired for wear resistant PVD hard coatings changes to the thermodynamically stable hexagonal wurtzite structure [7] via an intermediate transition region where both structures occur. However, to study the structure-property evolution of these ternary hard coatings over wide compositional ranges requires numerous deposition runs with several sputter targets (or arc-evaporation cathodes) if conventional ones with a fixed composition are used [4,5,7,8]. Although the target material input was shown to be reducible by using co-sputtering from either different combinations of pure metal and mosaic targets [9] or from different pure metal targets with varying power or current supply ratios [6,10-13], still several deposition runs are required to get a punctual overview of the property evolution with changing compositions. To reduce this huge effort especially for industrial-scale sputtering systems, a novel approach using triangle-like segmented targets is presented within this work. As $Cr_{1-x}Al_xN$ was chosen to be the model coating material, pure Cr and Al and Cr/Al 50/50 (at.%) target segments were developed to evaluate their potential in synthesizing coatings over wide compositional ranges at high resolution depending on the vertical substrate position. The resulting $Cr_{1-x}Al_xN$ coating compositions are discussed in detail, and special emphasis is laid on the investigation of the resulting structural, mechanical and tribological properties with respect to published results on conventional $Cr_{1-x}Al_xN$ hard coatings.

2. Experimental details

2.1 Coating deposition

The investigated coatings were deposited by reactive pulsed DC magnetron sputtering using an industrial-scale CemeCon CC800/9® MLT facility equipped with four unbalanced magnetrons [9]. On one of the two pairs of dual pulsed magnetrons, TiAl targets ($500 \times 88 \times 10$ mm³) with an Al content of 60 at.% were mounted. The second pair of magnetrons was adapted with magnetic shunts to reduce the magnetron race track appropriately for a target size of 200×88 mm² and equipped with pairs of triangle-like target segments as shown in Fig. 1. Two different combinations of segmented targets with an effective size of $200 \times 88 \times 6$ mm³ were used. Pure Al segments were either assembled with pure Cr or Cr/Al targets with an Al content of 50 at.% to cover broad ranges of AlN contents in the respective deposition runs depending on the vertical substrate position. All targets used were produced via powder metallurgical routes. The substrates were ground and polished cemented carbide discs (Ø 30×4 mm³) and cutting inserts in SNUN 120412 geometry ($12.7 \times 12.7 \times 4.8$ mm³) according to DIN ISO 1832 [14], consisting of 69.9% WC, 9.5% Co, 8.6% TiC, 10.8% TaC and 1.2% NbC (wt.%). Additionally, (100) oriented Si platelets with a thickness of 0.38 mm were coated. All substrates were ultrasonically pre-cleaned in acetone and ethanol for 10 min, respectively.

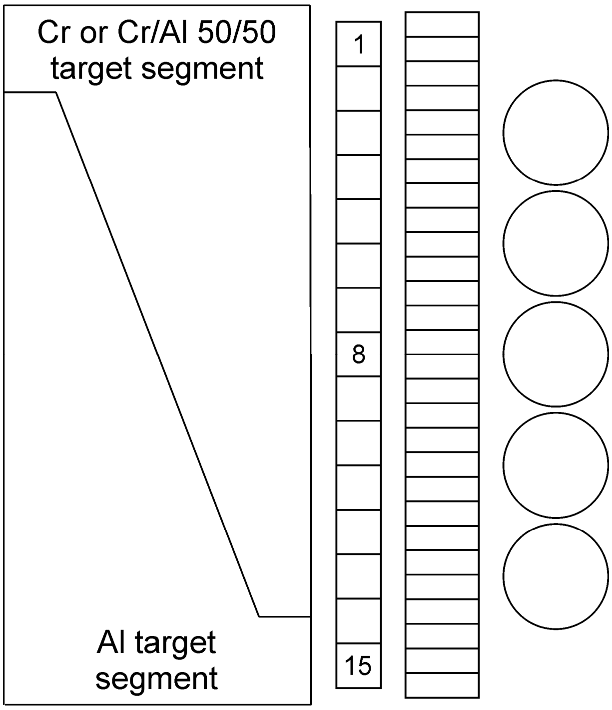

Fig. 1: Schematic of the segmented targets (200×88 mm²) used for deposition of the $Cr_{1-x}Al_xN$ top layers and the substrates (from left to right: 15 cemented carbide cutting inserts in SNUN geometry, 28 Si platelets, 5 cemented carbide discs) at their respective vertical positions. For the SNUN inserts, the numbering of the substrate positions is indicated.

During the applied coating deposition process with a base pressure of $< 4 \cdot 10^{-3}$ Pa, the substrates were further cleaned by heating (90 min) and Ar^+ ion etching (15 min mid-frequency etching, 45 min booster etching; cf. [15] for details). Subsequently, a TiAlN base layer was deposited from the TiAl targets, followed by the deposition of a $Cr_{1-x}Al_xN$ top layer from the segmented targets. During coating deposition, the chamber temperature was 525 °C and the pressure was held constant at 0.65 Pa via N_2 flow regulation at a constant Ar flow of 150 sccm. This yielded a N_2 fraction in the atmosphere of about 55 vol.%. The asymmetric bipolar bias voltage was set to -60 V with a pulse frequency of 350 kHz and a reversal time of 1 µs, corresponding to a duty cycle of 65%. Both magnetron pairs were dual pulsed at 20 kHz and a duty cycle of 50% in power controlled mode. The TiAl targets were supplied with 5 kW for 5 h to deposit the TiAlN base layer. In the subsequent 3.5 h, the segmented targets (pure Al combined with either pure Cr or Cr/Al 50/50) were operated with 1.1 kW for the deposition of the $Cr_{1-x}Al_xN$ top layer. Throughout the whole process, the substrate carousel was operated in twofold rotation. The target-to-substrate distance was 8.3-8.6 cm (substrates parallel to and facing the segmented targets) depending on the thickness of the substrates and the substrate holders.

2.2 Coating characterization

Chemical composition of the coatings was determined on all SNUN samples by energy-dispersive X-ray spectroscopy (EDX) using an Oxford Instruments INCA extension in a Zeiss EVO 50 scanning electron microscope (SEM). The acceleration voltage was set to 7 kV, and implemented standards were used for calibration. A CSM Instruments Calotest unit was used for coating thickness measurements via ball cratering on the Si samples. Coating adhesion on the cemented carbide discs was characterized by the VDI Rockwell indentation test, whereby damage to the coatings in the vicinity of a Rockwell C indent was assigned to adhesion classes between HF 1 and HF 6 according to DIN report 39 [16], using a Mitutoyo Durotwin DT-10 hardness tester.

Crystallographic investigations were performed on SNUN samples by grazing incidence X-ray diffraction (GIXRD) at a beam incidence angle of 2° with Cu K_α radiation in a Bruker-AXS D8 Advance diffractometer equipped with parallel beam optics and an energy-dispersive detector (Sol-X from Bruker-AXS). It should be noted here that in the asymmetric GIXRD configuration, diffraction occurs on lattice planes which are not parallel to the sample surface [17]. Therefore, information on the crystallographic orientation of the diffracting domains can not directly be derived from the measured diffractograms.

2.3 Mechanical properties

The compositional evolution of hardness and Young's modulus of the $Cr_{1-x}Al_xN$ top layer was determined on coated Si samples using an UMIS (Ultra Micro Indentation System, Fischer-Cripps Laboratories) nanoindenter equipped with a Berkovich tip. The maximum loads used in the plateau tests were chosen purposively to avoid influences of the underlying TiAlN base layer by keeping the indentation depth below 10% of the respective $Cr_{1-x}Al_xN$ top layer thickness. The load-displacement data was analyzed according to the Oliver and Pharr method [18], including experimental area functions determined using a silica standard of known elastic modulus to account for unavoidable microscopic indenter shape imperfections. Residual stress measurements of the coatings (intrinsically including the TiAlN base layers) were performed on coated Si samples using two parallel laser beams to measure the substrate curvature and applying the simplified Stoney equation [19,20].

2.4 Tribological investigations

Tribological tests were performed on the coated cemented carbide discs using a CSM Instruments ball-on-disc tribometer with alumina balls of Ø 6 mm, 5 N normal load, a sliding speed of 0.1 m/s, a sliding distance of 300 m and a radius of the wear track of 7 mm at room temperature in ambient air with relative humidities of 22-46%. The wear tracks were investigated by white light optical profilometry, using a Veeco Wyko NT1000 device in vertical scanning interferometry mode, to derive the volume of the worn area determined by three-dimensional cross-sections at four different positions along the wear track. The wear rates (K) were calculated from the measured wear volumes, the wear track circumference, the normal load and the number of laps.

3. Results and discussion

3.1 Compositional evolution

The EDX measurements were focused on the $Cr_{1-x}Al_xN$ top layers and their compositional evolution over the vertical substrate position. Concerning the TiAlN base layer, investigations on single layer coatings deposited in the same industrial-scale system can be found elsewhere [21,22]. The investigated $Cr_{1-x}Al_xN$ top layers showed a stoichiometric composition with ~50 at.% N content irrespective of the substrate position and the target segment configuration. The Al and Cr contents on the metal sublattice of $Cr_{1-x}Al_xN$

deposited from pure Al and Cr target segments are summarized in Fig. 2 as a function of the SNUN substrate position (cf. Fig. 1). A virtually linear behaviour can be observed with Al contents in the range of 21-46 at.% at a high compositional resolution.

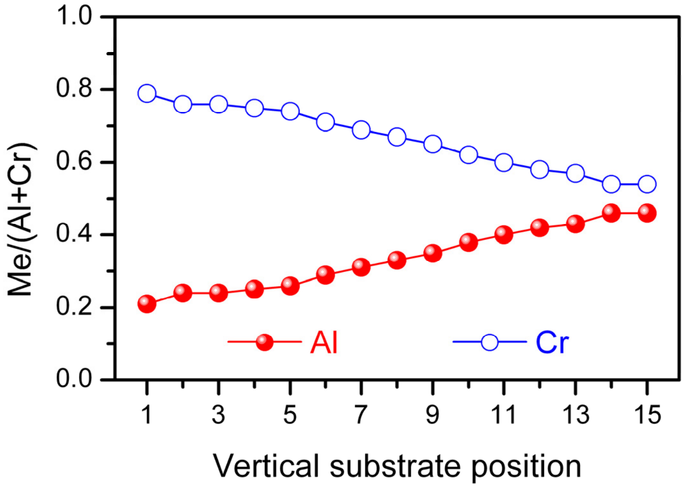

Fig. 2: Al and Cr contents on the metal sublattice of the $Cr_{1-x}Al_xN$ coatings deposited from pure Al and Cr target segments.

This seems to be surprisingly low as – regarding to the design of the segmented targets as shown in Fig. 1 – one could at first sight expect compositions of roughly $0 \leq x \leq 1$. One possible Al content damping factor is its stronger poisoning tendency compared to that of Cr with absolute formation energy values of 319 kJ/mol for AlN compared to 123 kJ/mol and 115 kJ/mol for CrN and Cr_2N (at room temperature) [23], respectively. As mentioned earlier, the N_2 fraction in the deposition chamber atmosphere was about 55 vol.%. Therefore, poisoning of the Al target segments resulting in a reduced sputter rate could yield lower Al contents in the coatings. A further explanatory factor can be found in the higher sputter yield Y of Cr compared to Al [24,25], but still the "reduction" of the maximum AlN content in the $Cr_{1-x}Al_xN$ coatings below 50 mol% is not satisfactorily explained keeping in mind the target design shown in Fig. 1. As sputtering is a very complex process [26,27], sputtered particle fluxes are not sufficiently described by a single number like the sputter yield, i.e. the average number of emitted atoms per incident ion. Neidhardt et al. [28] showed how the stoichiometry of TiB_x coatings is influenced by distinct process parameters and corroborated their experimental findings with Monte Carlo simulations. For instance, TRIM calculations [29] were performed to compare the angular emission distributions for sputtering of single element Ti and B targets with Ar^+ ions, showing significant differences. Sanchette et al. [30] investigated the sputtering behaviour of circular Al-Cr and Al-Ti targets in different segment configurations and schematically illustrated the different sputtering characteristics of Cr, Al and Ti (cf. Fig. 3 in [30]) to explain the obtained coating compositions along the radial substrate position. Al and Cr thereafter do not only exhibit different sputter yields, but also the angular distributions differ significantly with a much broader distribution for Cr. Thus, to go into more detail, TRIM simulations similar to those in Ref. [28] were conducted. 99,999 Ar^+ ions impinging perpendicularly on Al and Cr targets (supposing sputtering in metallic mode) with 500 eV, which approximately corresponds to the difference of the observed cathode voltages and the estimated plasma potential, were chosen for surface sputtering calculations. The output data on the emitted particles was subsequently analyzed and converted to comparative plots of the normalized sputter emission fluxes of Al and Cr as a function of the emission angle θ in Fig. 3. An ideal cosine distribution in terms of

$$Y(\Theta) \propto \cos^n \Theta \tag{1}$$

according to [31] with n = 1 is included as guideline in the logarithmic illustration.

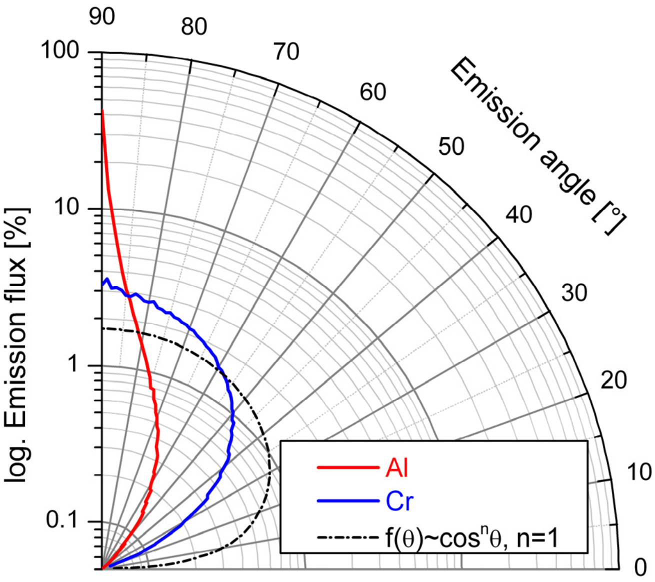

Fig. 3: Normalized angular distributions of Al and Cr particles sputtered by Ar^+ impinging at 500 eV as simulated by TRIM in comparison to an ideal cosine distribution [31].

Although both Al and Cr show over-cosine behaviour, it is clearly more pronounced for Al as its emission flux is mainly directed along the target surface normal. As Fig. 3 shows normalized emission distributions, also the overall sputter yield values have to be taken into account. For Ar^+ impact, the simulations yield a Cr sputter yield of 1.39, whereas it is only half of that for Al with 0.68 (Table 1). Therefore, it can be stated that the observed Al deficiency on the metal sublattice of the $Cr_{1-x}Al_xN$ coatings is rather a Cr enrichment caused by the higher sputter yield of Cr in combination with its significantly broader angular sputter emission distribution compared to Al. At the upmost substrate position as shown in Fig. 1, the maximum achievable AlN content x in the $Cr_{1-x}Al_xN$ coatings is thus limited, i.e. to x = 0.46, due to interference of the Al flux with Cr originating from lower target regions. At the lowest substrate position, on the other hand, the Cr flux is supplemented by Al stemming from higher target regions. However, this interference is by far less pronounced due to the narrower emission distribution of Al as shown in Fig. 3 and its lower sputter yield (Table 1), resulting in a minimum AlN content of x = 0.21 in the $Cr_{1-x}Al_xN$ top layers.

It was mentioned before that the reactive volume fraction in the process gas was quite high. Therefore, probably arising effects on the sputtering behaviour should be taken into account. Although in the present state-of-the-art model for reactive sputtering proposed by Depla et al. [32] only sputtering by Ar^+ ions is taken into account, it is recommended to include reactive ions in case of process conditions like those chosen in the present work. Thus, the simulations presented above were repeated with N_2^+ and N^+ projectiles. As shown in Figs. 4 and 5, the influence of the respective bombarding species on the normalized angular emission distributions of Al and Cr is negligible. Especially Cr shows almost identical distributions for all three projectiles. However, the overall sputter yield values vary for the different species as summarized in Table 1. N_2^+ projectiles lower the Cr yield by approximately 17%, whereas Al shows an insignificant increase of 3%. N^+ bombardment yields no significant further change for Cr, while the sputter yield of Al is increased distinctly to 1.18. However, the fraction of N^+ impinging on the targets will be small compared to Ar^+ and N_2^+ [33]. Therefore, although the reactive gas influences the sputter yield to some extent, the qualitative conclusions drawn from the simulations summarized in Fig. 3 on the obtained coating compositions remain valid.

Table 1: Sputter yields of Al and Cr as simulated by TRIM for different projectiles impinging at 500 eV

projectile	Al	Cr
Ar^+	0.68	1.39
N_2^+	0.70	1.16
N^+	1.18	1.14

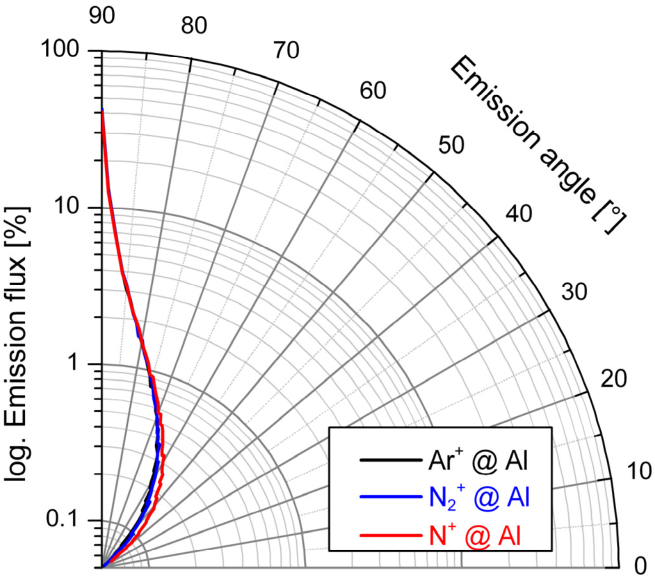

Fig. 4: Normalized angular distributions of sputtered Al particles as simulated by TRIM for impinging Ar^+, N_2^+ and N^+ at 500 eV.

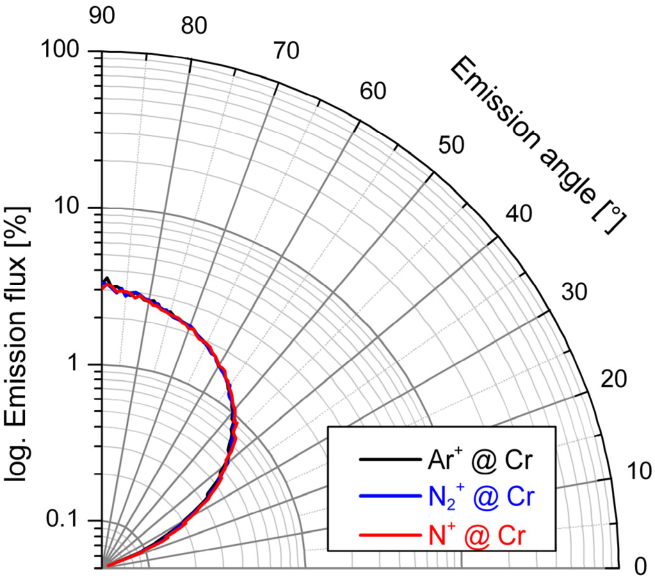

Fig. 5: Normalized angular distributions of sputtered Cr particles as simulated by TRIM for impinging Ar^+, N_2^+ and N^+ at 500 eV.

The transport phase of the sputtered particles shall just briefly be discussed in a qualitative manner. The number of collisions between the atoms travelling from the target to the substrate and the gas species in the chamber atmosphere increases exponentially with the product of the gas pressure and the target-to-substrate-distance [34,35]. Stated differently, this pressure-distance product exponentially increases the number of particles being thermalized at the expense of the ballistic flux arriving at the substrate. The coatings investigated in this work were deposited at 5.4-5.6 Pa·cm (depending on the substrate thickness and the substrate holder). Therefore, only a minor fraction of the sputtered atoms will be thermalized [34]. However, as a few collisions will occur, the angular distribution shown in Fig. 3 will be altered. Due to the low atomic mass of Al, it will be deflected with high scattering angles (60-65° according to [35]). Consequently, the Al flux will be altered in a way that mainly the Al/Cr flux ratio arriving at the substrate will decrease [34]. The influence of the broadened Al flux will be insignificant for the growing $Cr_{1-x}Al_xN$ coating as mainly the deposition rate at the chamber walls will increase. However, the scattering angle is known to decrease with increasing atomic mass [34]. Therefore, the effect of collisions will be less pronounced for the heavier Cr. The lower scattering angle (about 40° according to [35]) will slightly reduce the effective sputter yield for Cr, but apart from that the qualitative discussions concerning the Cr enrichment in the growing $Cr_{1-x}Al_xN$ films are reconfirmed. However, it can be summarized that the obtained coating compositions can well be qualitatively corroborated with TRIM simulations for the deposition run with elemental target segments.

For the Cr/Al 50/50 and Al target segment combination, again a linear increase of the Al content in the range of 60-74 at.% was observed (Fig. 6). Therefore, the compositional resolution as a function of the vertical substrate position for this deposition run is even increased. However, akin to the results of the first deposition run discussed above, the question arises why the obtained compositional range is that much narrower than the roughly expectable $0.5 \leq x \leq 1$. Since static TRIM calculations are not suitable for sputtering of compound targets due to dynamic changes in the surface composition caused e.g. by preferential sputtering [36], only qualitative conclusions can be drawn from Fig. 3 for this case. Nevertheless, it seems feasible to attribute the obtained coating compositions and their narrower range to the above-mentioned reasons. The surface of the Cr/Al 50/50 target segments will quickly be depleted in Cr due to its higher sputter yield, probably resulting in a compound sputter yield dominated by that of Al. The growth rate values for reactive sputtering from pure Cr and Cr/Al 50/50 targets (5 Å/s and 2Å/s, respectively) reported by Barshilia et al. [37] corroborate this assumption. Therefore, the sputtered Cr particles will again exhibit a wider angular distribution, interfering with the more directional atom flux coming from the Al segment. Therefore, at the upmost substrate position as shown in Fig. 1, the maximum achievable AlN content x in the $Cr_{1-x}Al_xN$ coatings will be limited, i.e. to $x = 0.74$ for the present target configuration and deposition parameters. With $x = 0.60$, the lowest AlN content achieved seems evident, as the flux coming from the Cr/Al 50/50 target will be complemented with Al coming from the pure Al segment. In this case, the interference is less pronounced because of the flux' narrow angular distribution, as depicted in Fig. 3. However, summarizing the EDX results, it can be stated that the use of triangle-like segmented targets is a suitable approach to cover broad compositional ranges at high resolution within one single deposition run.

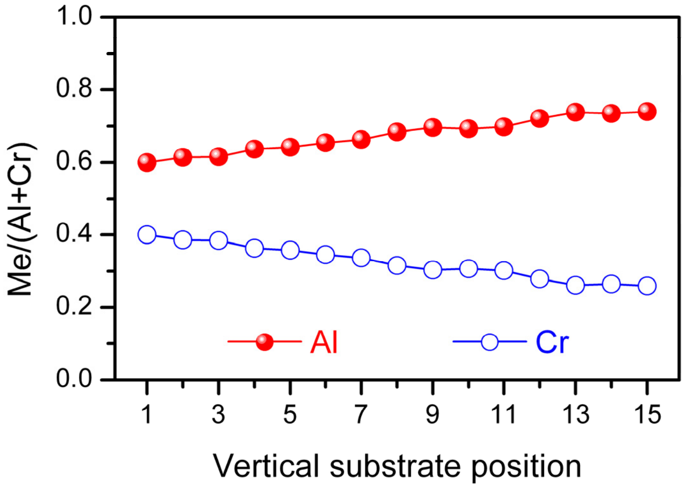

Fig. 6: Al and Cr contents on the metal sublattice of the $Cr_{1-x}Al_xN$ coatings deposited from Al and Cr/Al 50/50 target segments.

All further results in this work are shown as a function of the measured AlN mole fractions in the $Cr_{1-x}Al_xN$ coatings as shown in Figs. 2 and 6 for the coated SNUN cutting inserts. For measurements performed on Si (100) samples and on cemented carbide discs, linear interpolation was used for conversion as the number of coated samples varied for the different types of substrates as depicted in Fig. 1. It should be mentioned here that the $Cr_{1-x}Al_xN$ top layers on cemented carbide discs used for the tribological investigations show a slight compositional gradient because of their 30 mm diameter. However, this gradient is low with a maximum absolute AlN content variation of about 1.8 mol% over the area investigated in the tribological tests.

3.2 Coating thickness and adhesion

The coating thickness measurements are summarized in Fig. 7. Note that different scales are used before and after the break in the abscissa of Fig. 7 and all further figures in this work for better readability. The thickness of the TiAlN base layer was about 1.9 µm for all substrate positions. For the $Cr_{1-x}Al_xN$ top layers, however, slight thickness variations over the AlN content x are observable. For both investigated deposition runs, boundary effects are visible as the substrates were mounted along the whole length of the segmented targets, i.e. 200 mm. Additionally, it is obvious that the thickness of the $Cr_{1-x}Al_xN$ top layer decreases with increasing Al content, which can again be attributed to the lower sputter yield of Al compared to that of Cr, probably also dominating the compound sputter yield of the Cr/Al 50/50 targets as supposed earlier. Consequently, the $Cr_{1-x}Al_xN$ thickness values are ranging from 0.9 to 1.4 µm, yielding a total coating thickness of 2.6-3.5 µm.

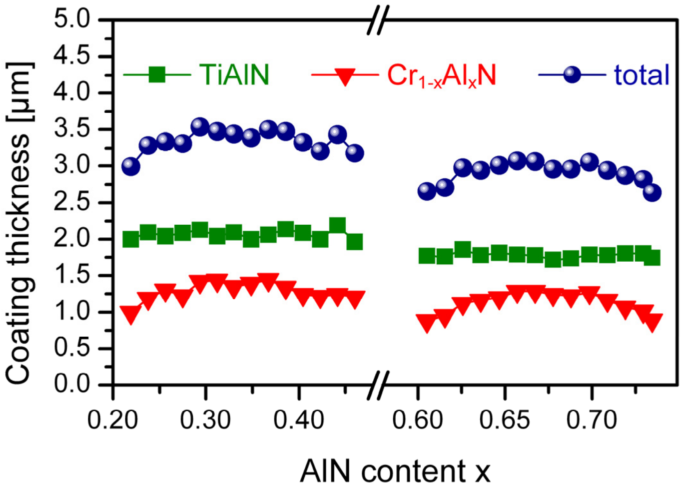

Fig. 7: Results of the coating thickness measurements for the TiAlN base layers, the $Cr_{1-x}Al_xN$ top layers and the total coating thickness as a function of the AlN content x in $Cr_{1-x}Al_xN$ as determined by EDX measurements. Note that different scales are used before and after the break in the abscissa.

The adhesion of the coatings with $0.21 \le x \le 0.46$ in the $Cr_{1-x}Al_xN$ top layer corresponds to HF 2-3 in the Rockwell test. The coatings with higher Al content in the top layer showed a slightly worse adhesion.

3.3 Structural evolution

Representative GIXRD patterns for different AlN mole fractions x in the $Cr_{1-x}Al_xN$ top layers are summarized in Fig. 8. Although the structural information of the diffractograms recorded with an grazing incidence angle of $\alpha = 2°$ mainly stems from the surface-near region [17], some of the strongest cemented carbide substrate peaks (mainly WC) are visible in all patterns. Therefore, the respective standard positions are indicated in addition to the relevant positions for the coatings [38]. In most of the diffractograms, a substrate peak is visible below $2\theta = 41.5°$, which is slightly shifted to lower angles compared to the indicated standard position, i.e. the (200) diffraction peak of fcc TiC [38]. This can be attributed to an increased unit cell volume due to substitution of Ti by bigger Ta and Nb atoms in a mixed carbide phase. Regarding the coatings deposited from pure Al and Cr segments ($x = 0.21$ and $x = 0.46$), it is obvious that both the TiAlN base layer and the $Cr_{1-x}Al_xN$ top layers show single phase cubic (c) structures without any evidence for the thermodynamically stable wurtzite (w) AlN. The bilayer configuration of the coatings yields a superposition of the respective peaks for c-TiAlN and c-$Cr_{1-x}Al_xN$ neighbouring each other due to similar lattice constants. However, the $Cr_{1-x}Al_xN$ portion of the peaks is shifted towards the c-AlN standard position with increasing AlN mole fraction x because of the resulting decrease of the lattice constant due to the substitution of Cr by smaller Al [38]. The patterns for higher Al contents in the $Cr_{1-x}Al_xN$ top layer generally show broader peaks according to a decreasing average size of the diffracting domains [17], which was also observed earlier [6,13]. Barshilia et al. [37] reported a lower crystallite size in CrAlN coatings in comparison with pure CrN. They attributed this phenomenon to increased ion bombardment using Cr/Al 50/50 targets as they observed a 21.3% higher ion current compared to the deposition of CrN. In the present study, the substrate ion current using the Cr/Al 50/50 and Al target segment combination was by 17.5% higher than with pure Cr and Al segments. This phenomenon can be ascribed to the higher ion induced secondary electron emission coefficient γ_{se} of Al compared to Cr, which can be calculated from the empirical formula $\gamma_{se} \approx 0.016\cdot(\varepsilon_{iz}-2\varepsilon_{\phi})$ [39], where ε_{iz} denotes the ionization potential of the impinging ion and ε_{ϕ} the work function of the bombarded material. Applying the respective data from [40] yields an about 10% higher γ_{se} for Al than for Cr for all bombarding species (Ar^+, N_2^+ and N^+) relevant in this work. Therefore, it can be assumed that the ion bombardment intensity increases with increasing AlN content in the coatings, leading to the observed trend of decreasing domain sizes. However, the metastable solubility limit for AlN in c-$Cr_{1-x}Al_xN$ is reached at $x = 0.61$ as there is no evidence for the presence of w-AlN, whereas in the pattern for $x = 0.62$ the (102) peak of w-AlN slightly arises at about $2\theta = 49.8°$. This is relatively low compared to the generally accepted maximum solubility limit of $x = 0.77$ for c-$Cr_{1-x}Al_xN$ [6], but still in good agreement with experimental results published earlier [7,10,13]. According to Chen et al., a possible explanation for the lowered AlN solubility limit can be found in the high N_2 fraction in the process gas [41]. Furthermore, the pulsing parameters are known to strongly affect the microstructure of the resulting coatings [42,43]. However, in the diffractogram for $x = 0.69$, $Cr_{1-x}Al_xN$ shows a more pronounced dual phase structure. Here, although the (002) standard position of w-AlN at about $2\theta = 36.0°$ is superimposed with reflections from the substrate and the fcc coating material, a distinct peak arises. At the highest Al content of $x = 0.74$, the $Cr_{1-x}Al_xN$ top layer is still in the dual phase regime as, although the fraction of w-AlN is further increased, the presence of c-$Cr_{1-x}Al_xN$ is obvious. Summarizing the performed GIXRD investigations, it can be stated that the domain size in the c-$Cr_{1-x}Al_xN$ top layers decreases with increasing AlN content, and the metastable solubility limit for AlN at the given coating process parameters is $x = 0.61$.

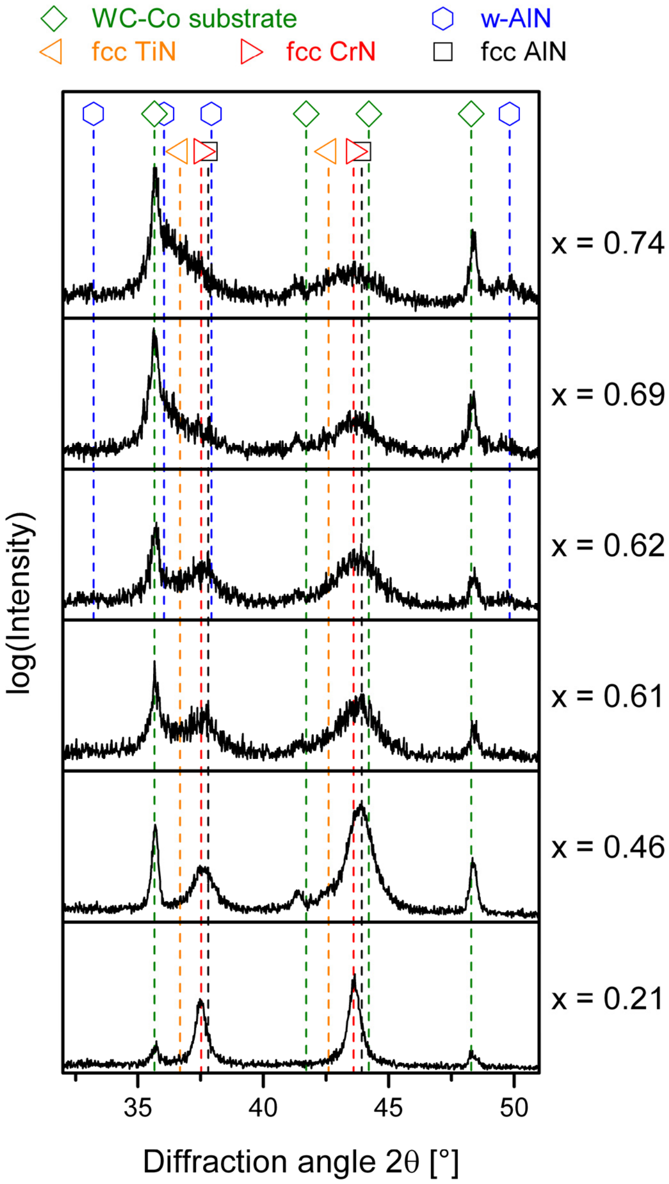

Fig. 8: Representative GIXRD patterns of $Cr_{1-x}Al_xN$ top layers with different AlN contents x on TiAlN base layers deposited on cemented carbide substrates.

3.4 Mechanical properties

Fig. 9 shows the evolutions of hardness, Young's modulus and the resulting hardness to Young's modulus ratio H/E of the $Cr_{1-x}Al_xN$ top layers. As expected, the hardness increases with increasing AlN content from 19.7 GPa for x = 0.22 to a maximum value of 25.2 GPa for x = 0.37, which is in perfect agreement with Park et al. [44]. Around x = 0.4, the hardness slightly decreases again to values in the range of 22.6-24.1 GPa. A similar behaviour was observed by Ding and Zeng, who deposited $Cr_{1-x}Al_xN$ coatings with different compositions by co-sputtering from elemental Cr and Al targets [11]. The more significant decrease in hardness for x = 0.44 and x = 0.46 is probably attributed to a combination of two effects. The boundary effect also discussed with regard to the observed coating thickness evolution leads to a lower atom flux to the substrates, although it is not very pronounced in this case with regard to Fig. 7. On the other hand, the ion flux is higher for sputtering of Al compared to Cr, as discussed before. It is clearly visible in Fig. 1 that the samples arranged at the bottom of the substrate holder are just facing the pure Al target segments. Consequently, the ion flux is distinctly increased in this region. This yields a high ion-to-atom flux ratio and probably an excessive ion bombardment resulting in high defect densities and therefore deteriorated coating properties [11,45], such as the observed hardness drop down to 15.9 GPa. Although the nominal substrate bias voltage of -60 V applied in the present work was not immoderately high compared to published data on the influence of ion irradiation during film growth [45-48], it should be considered that a direct comparison is difficult as no universal parameter describing the irradiation effects on coating growth is established up to now. Furthermore, the atom fluxes in the works cited above are typically thermalized to exclude the influence of the kinetic energies of the depositing metal species, while in the present work the majority of the Al and Cr atoms arriving at the substrates are ballistic (cf. section 3.1). However, not taking the differences in the absolute values of the applied bias voltages into account, comparisons with results of Petrov et al. [45] seem justified. In their review, the effects of ion irradiation on coating growth were either investigated through variations in the kinetic energy of the bombarding ions at ion-to-atom ratios of ≤ 1, or by increasing the ion-to-atom arrival ratio up to 10 at low kinetic energies of up to 20 eV. While increasing the ion flux was shown to be an effective tool for microstructure modifications, high kinetic energies of the impinging ions yield a high number of incorporated defects. However, the growth conditions in the present work were probably somewhere in between. Unfortunately, the data necessary for an exact quantification of the kinetic energies and ion-to-atom flux ratios for the different coating compositions are not accessible for the applied industrial pulsed DC sputtering system using substrate rotation, but the kinetic energy of impinging ions will surely be beyond 20 eV, and the ion-to-atom flux ratios will be distinctly beyond unity. Therefore, it could be argued that for the coatings grown on substrates facing the pure Al target segments, some critical ion bombardment intensity for the respective kinetic energy is reached, yielding significant defect formation. Typically, high defect densities yield high compressive stresses, which should in turn increase the hardness of the material. At this point, it has to be kept in mind that the applied substrate bias was bipolarily pulsed with a relatively long positive voltage fraction of 35%. According to Grasser et al. [49], the electron bombardment of the growing film during the positive substrate potential fraction efficiently yields defect annihilation. Therefore, it seems plausible that the distinct hardness drop for the $Cr_{1-x}Al_xN$ top layers with $x = 0.44$ and $x = 0.46$ is a consequence of material imperfections continuously caused by alternating defect formation through excessive ion bombardment and defect annihilation. This hypothesis would coincide with Lin et al. [43] suggesting relatively small substrate bias voltages of -50 V or below for pulsed magnetron sputtering of $Cr_{1-x}Al_xN$. However, for the coatings sputtered from the Cr/Al 50/50 target segment combination, there seems to be a slight trend to increasing hardness from 21.7 GPa up to 23.6 GPa in the range of $0.60 \leq x \leq 0.68$. According to the GIXRD results, this compositional region is characterized by fine-grained c-$Cr_{1-x}Al_xN$ with small amounts of embedded w-AlN in the dual phase structure. Obviously, this yields a slight precipitation hardening effect [50] at this initial stage of w-AlN formation, which was also reported in other publications [42,51]. Furthermore, the beneficial effect of the afore-mentioned decreasing domain sizes according to the Hall-Petch relation [50,52,53] will be superimposed. However, for $x > 0.68$, where the w-AlN fraction becomes more significant, the hardness monotonously decreases to 16.0 GPa for $x = 0.74$. As it was discussed earlier for the pure Cr and Al target segment combination, the coating properties in this region with low atom flux (cf. Fig. 7) will additionally suffer from an excessive ion bombardment stemming from the pure Al segment. However, it can be summarized that the hardness behaviour for different compositions and vertical substrate positions can reasonably be explained and corroborated with earlier data from literature.

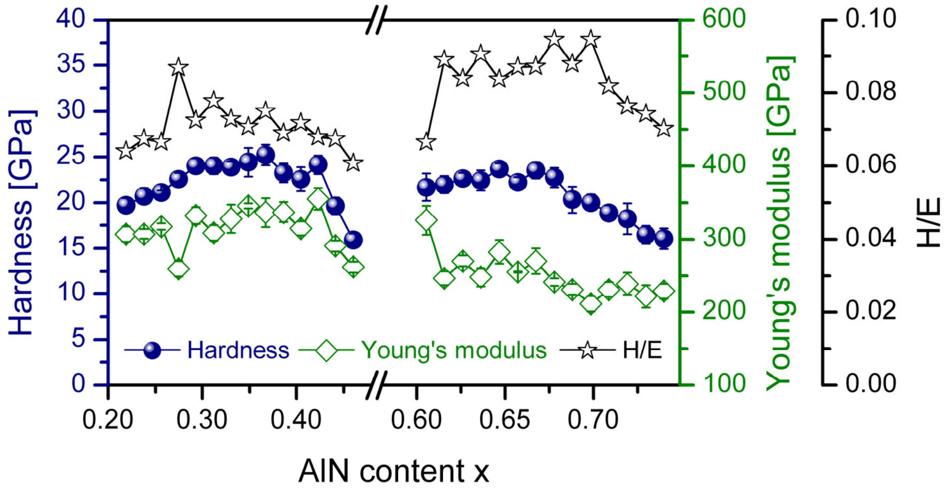

Fig. 9: Hardness, Young's modulus and the resulting H/E ratio of the $Cr_{1-x}Al_xN$ top layers measured by nanoindentation as a function of the respective AlN content x.

The Young's modulus evolution of the $Cr_{1-x}Al_xN$ top layers is similar to that described for the hardness, as can be seen in Fig. 9. For $x \leq 0.42$, the measured values increase with x in the range of 310-360 GPa, followed by a distinct drop to 260 GPa. The $Cr_{1-x}Al_xN$ top layers sputtered from the Cr/Al 50/50 and Al target segment combination exhibit a Young's modulus of almost 330 GPa for an AlN content of slightly below $x = 0.61$, while 240-280 GPa were measured up to $x = 0.68$, i.e. the early dual phase regime as discussed before. This further corroborates that the metastable solubility limit for AlN at the given coating process parameters is located at $x = 0.61$. However, the Young's modulus further decreases slightly to 210-240 GPa for $x > 0.68$, where a higher amount of w-AlN is present.

As the H/E ratio is known to be a suitable parameter for predicting a material's performance e.g. in tribological applications [54-56], its evolution over the AlN content is indicated in Fig. 9 as well. For the lowest AlN contents up to $x = 0.31$ in the $Cr_{1-x}Al_xN$ top layers, H/E shows an increasing trend, indicating increasing coating performance. This can be attributed to the beneficial effect of Al as alloying element in CrN [4,5]. For $0.31 \leq x \leq 0.46$, H/E tends to slightly decrease again. However, in the early dual phase regime, the highest H/E values are reached, with an increasing trend up to $x = 0.70$. Thereafter, where the w-AlN content in the $Cr_{1-x}Al_xN$ top layer gets more pronounced, H/E shows a significant drop, indicating deteriorated coating properties at these high AlN concentrations.

Summarizing the nanoindentation experiments, it can be concluded that the evolutions of hardness, Young's modulus and the resulting H/E ratio indicate promising properties of the investigated coatings for tribological applications.

The residual stress measurements were performed using the substrate curvature method. Therefore, they intrinsically include the TiAlN base layer, which considerably affects the results summarized in Fig. 10. Its effect is on the one hand caused by the higher thickness of the base layer (cf. Fig. 7), which is – according to [22] – more or less stress free, and on the other hand by the higher Young's modulus of the TiAlN base layer (about 400 GPa according to [21]) compared to values in the range of 210-360 GPa measured for the $Cr_{1-x}Al_xN$ top layer depending on the composition. Consequently, only qualitative trends of the residual stresses in the top layer can be derived from Fig. 10, while especially the highest compressive stresses will be significantly underestimated. However, again boundary effects caused by varying ion-to-atom flux ratios are observable. Lower atom flux ratios at the boundaries yield more intense ion bombardment of the growing films, which is known to result in compressive stresses [1,45,57,58]. In the range of $0.24 \leq x \leq 0.27$, slight tensile stresses are visible, which could be a result of the relatively high atom flux mainly stemming from the Cr target segment (cf. Fig. 1), while the coatings are stress free up to $x = 0.40$. For $0.42 \leq x \leq 0.46$, the afore-mentioned higher ion flux from the Al target segments yields a more efficient ion peening effect, shifting the overall residual stresses significantly into the compressive region [1]. As the growth rates of the $Cr_{1-x}Al_xN$ top layers sputtered from Cr/Al 50/50 and Al target segments are in general lower than those from pure Cr and Al segments (cf. Fig. 7), and the ion flux increases with the Al content as discussed before, the ion-to-atom flux ratios for these coatings will be generally higher, resulting in further increased compressive stresses. Moreover, the unit cell volume of w-AlN, which was observed for $x > 0.61$ (cf. Fig. 8), is approximately 20% larger than that of c-AlN [59,60]. However, besides a slight boundary effect, the initial appearance of w-AlN and the increasing atom flux visible in Fig. 7, yielding a reduction of the ion-to-atom flux ratio, seem to compensate each other in the range of $0.60 \leq x \leq 0.64$, where compressive stresses with absolute values of 400-500 MPa were measured. For $x > 0.64$, the compressive stresses in the dual phase structure gradually increase to 600-700 MPa due to the growing fraction of w-AlN as shown in Fig. 8. For the highest AlN contents ($x > 0.72$), compressive residual stresses of 800-1200 MPa were observed, again demonstrating the boundary effect, which is more pronounced at the Al-rich boundaries (the lowest substrate positions) due to the high ion flux stemming from the Al target segments (cf. Fig. 1). In summary, the promising mechanical properties of the investigated coatings are in perfect agreement with the GIXRD results and the coating thickness measurements.

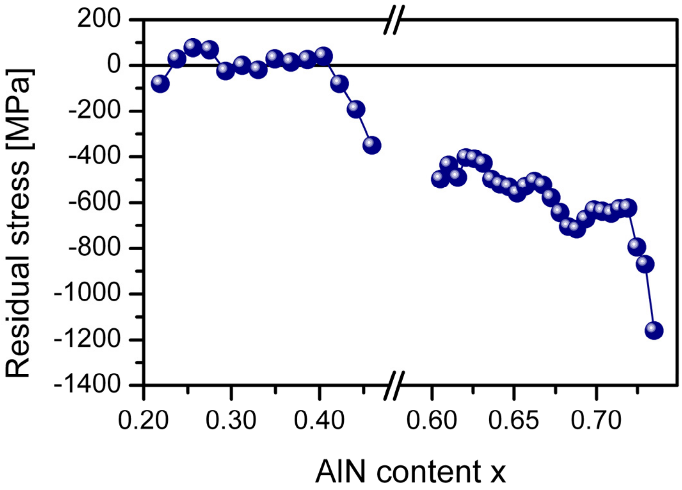

Fig. 10: Residual stresses in the coatings as a function of the AlN content x in the $Cr_{1-x}Al_xN$ top layers on TiAlN base layers deposited on Si substrates.

3.5 Tribological performance

The results of the conducted tribological investigations are summarized in Fig. 11. As the friction curves showed steady-state behaviour after a short running-in period, the first

50 m of the sliding distance were omitted for the calculation of the average friction coefficients μ and the respective standard deviations. The samples coated with $Cr_{1-x}Al_xN$ from pure Cr and Al target segments show low friction with $\mu \approx 0.4$-0.5, which is attributed to their smooth surface as observed by SEM (not shown here) in the course of the EDX investigations. The friction coefficient increases with the AlN content in the $Cr_{1-x}Al_xN$ top layers as they tend to become rougher. The same behaviour was described in Refs. [11,61]. μ increases further to 0.7 at the beginning of the dual phase region ($0.60 \leq x \leq 0.67$). The two $Cr_{1-x}Al_xN$ coatings with the highest AlN contents and consequently a more pronounced dual phase structure exhibit slightly lower friction coefficients of $\mu \approx 0.6$, indicating a change in the tribological behaviour. One possible reason for this can be found in the decreasing hardness of the $Cr_{1-x}Al_xN$ top layer (cf. Fig. 9), yielding a lower resistance against abrasion, which was observed to be the dominating wear mechanism. Consequently, ploughing [62] is slightly easier, reducing the resistance against sliding and thus the energy loss under tribological load, i.e. reduced friction [63]. Furthermore, by investigating the used alumina balls via light microscopy, it was observed that the diameter of the respective wear scars was about three times that of the ball used for tribological testing of the sample with $x = 0.67$ in the $Cr_{1-x}Al_xN$ top layer. Consequently, the nominal as well as the real contact area probably differed significantly.

The tribological investigations in general demonstrate an excellent wear resistance of the coatings. As long as the $Cr_{1-x}Al_xN$ top layers are in the single phase cubic regime ($0.21 \leq x \leq 0.46$), the wear rate K lies in the range of 1.8-$3.2 \cdot 10^{-16}$ m^3/Nm, which is again in perfect agreement with Ding and Zeng [11]. Furthermore, the minimum in wear rate also precisely agrees with the local maximum in the H/E ration depicted in Fig. 9. In the early dual phase regime ($0.60 \leq x \leq 0.67$), K increases to 5.0-$6.0 \cdot 10^{-16}$ m^3/Nm. Although minor fractions of w-AlN are present, these coatings exhibit hardness values of 21.7-23.6 GPa and the highest H/E ratios (cf. Fig. 9). Therefore, the wear rate increase compared to lower AlN contents in the $Cr_{1-x}Al_xN$ top layer is probably attributed to the observed surface roughness increase. The two samples with the highest AlN contents in the top layer, in which a considerable amount of w-AlN is present, reducing the hardness as well as the H/E ratio (cf. Fig. 9) and therefore the tribological load bearing capacity through an increased ploughing tendency [64], showed partial coating failure as indicated in Fig. 11. There, the wear coefficients were evaluated for the portions of the wear tracks which were still intact. As the respective data points in Fig. 11 consequently underestimate the wear rates, different symbols are used, showing increased wear rates of 8.4-$14.4 \cdot 10^{-16}$ m^3/Nm. However, it can be stated that the single phase cubic $Cr_{1-x}Al_xN$

coatings sputtered from segmented targets show superior tribological properties, which are well competitive compared with results on $Cr_{1-x}Al_xN$ coatings published earlier [4,8,11,13,43], corroborating the relevance and potential of the chosen segmented target approach for economical coating material development.

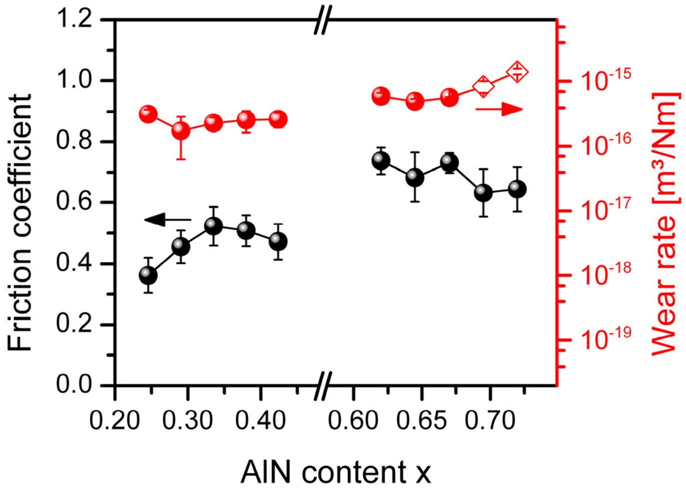

Fig. 11: Friction coefficients and wear rates of the coatings as a function of the AlN content x in the $Cr_{1-x}Al_xN$ top layers. The data points marked by diamonds underestimate the respective wear rates due to partial coating failure, as the wear volumes were measured in the areas where the coatings were still intact.

4. Conclusions

Within this work, it was proved that the use of triangle-like segmented targets is an efficient and economic novel approach in coating material development using industrial-scale magnetron sputtering systems. Cr, Al and Cr/Al 50/50 target segments were successfully developed to synthesize $Cr_{1-x}Al_xN$ coatings with AlN contents in the range of $0.21 \leq x \leq 0.74$ and high compositional resolution on TiAlN base layers in two deposition runs. With the chosen process parameters, the solubility limit of AlN in the metastable c-$Cr_{1-x}Al_xN$ solid solution was detected at $x = 0.61$. A maximum hardness of 25.2 GPa was achieved for $x = 0.37$. In the single phase cubic regime, the investigated coatings showed excellent tribological performance with low friction of $\mu \approx 0.4\text{-}0.5$, due to the smooth coating surfaces obtained, and outstanding wear rates of $1.8\text{-}3.2 \cdot 10^{-16}$ m³/Nm. In conclusion, it can be stated that the presented segmented target approach is an auspicious novel tool for the coating community with a high potential to significantly reduce the workload for coating material developers.

Acknowledgements

This work was done within the Research Studio Austria energy-drive, with financial support from the Österreichische Forschungsförderungsgesellschaft and the Bundesministerium für Wirtschaft, Familie und Jugend. T.W. gratefully acknowledges helpful discussions on the performed TRIM simulations with Dr. J. Neidhardt (Von Ardenne Anlagentechnik GmbH, Dresden, Germany) and S. Grasser (Montanuniversität Leoben, Austria). Furthermore, the authors acknowledge the assistance of C. Sabitzer (Montanuniversität Leoben, Austria) in coating deposition and characterization.

References

[1] P.H. Mayrhofer, G. Tischler, C. Mitterer, Surf. Coat. Technol. 142-144 (2001) 78.

[2] W.D. Münz, J. Vac. Sci. Technol. A 4 (6) (1986) 2717.

[3] S. PalDey, S.C. Deevi, Mater. Sci. Eng. A 342 (1-2) (2003) 58.

[4] Y. Ide, T. Nakamura, K. Kishitake, in: B. Mishra, C. Yamauchi (Eds.), Proceedings of the 2nd International Conference on Processing Materials for Properties, The Minerals, Metals & Materials Society, Warrendale, PA, 2000, pp. 291-296.

[5] A.E. Reiter, V.H. Derflinger, B. Hanselmann, T. Bachmann, B. Sartory, Surf. Coat. Technol. 200 (7) (2005) 2114.

[6] A. Sugishima, H. Kajioka, Y. Makino, Surf. Coat. Technol. 97 (1-3) (1997) 590.

[7] M. Kawate, A. Kimura, T. Suzuki, J. Vac. Sci. Technol. A 20 (2) (2002) 569.

[8] R. Franz, B. Sartory, R. Kaindl, R. Tessadri, A. Reiter, V.H. Derflinger, P. Polcik, C. Mitterer, in: G. Kneringer, P. Rödhammer, H. Wildner (Eds.), Proceedings of the 16th International Plansee Seminar, vol. 2, Plansee Holding AG, Reutte, 2005, pp. 932-945.

[9] N. Bagcivan, K. Bobzin, S. Theiß, Thin Solid Films 528 (2013) 180.

[10] Y. Makino, K. Nogi, Surf. Coat. Technol. 98 (1-3) (1998) 1008.

[11] X.Z. Ding, X.T. Zeng, Surf. Coat. Technol. 200 (5-6) (2005) 1372.

[12] G.S. Kim, S.Y. Lee, Surf. Coat. Technol. 201 (7) (2006) 4361.

[13] J. Lin, B. Mishra, J.J. Moore, W.D. Sproul, Surf. Coat. Technol. 201 (7) (2006) 4329.

[14] DIN Deutsches Institut für Normung e.V., Wendeschneidplatten für Zerspanung - Bezeichnung (DIN ISO 1832:2004), Beuth Verlag, Berlin, 2005.

[15] T. Weirather, A. Fian, B. Sartory, D. Caliskanoglu, W. Kölker, C. Mitterer, Surf. Coat. Technol. 206 (17) (2012) 3601.

[16] H.-R. Stock, A. Schulz, W. Ensinger, J. Güttler, E. Fromm, D. Müller, W.D. Busch, H. Grützner, in: H. Jehn, G. Reiners, N. Siegel (Eds.), DIN Fachbericht 39, Beuth Verlag, Berlin, 1993, pp. 210-234.

[17] M. Birkholz, P.F. Fewster, C. Genzel, Thin Film Analysis by X-ray Scattering, Wiley-VCH, Weinheim, 2006.

[18] W.C. Oliver, G.M. Pharr, J. Mater. Res. 7 (6) (1992) 1564.

[19] G.G. Stoney, Proc. R. Soc. London A 82 (553) (1909) 172.

[20] W.D. Nix, Metall. Trans. A 20 (11) (1989) 2217.

[21] N. Schalk, T. Weirather, C. Polzer, P. Polcik, C. Mitterer, Surf. Coat. Technol. 205 (19) (2011) 4705.

[22] N. Schalk, C. Mitterer, J. Keckes, M. Penoy, C. Michotte, Surf. Coat. Technol. 209 (2012) 190.

[23] E.A. Brandes, Smithells Metals Reference Book, 6th ed., Butterworth Publishers, Stoneham, 1983.

[24] H.H. Andersen, H.L. Bay, in: R. Behrisch (Ed.), Sputtering by Particle Bombardment I: Sputtering of Single Element Solids, Springer, Berlin, 1981, pp. 145-218.

[25] W. Eckstein, in: R. Behrisch, W. Eckstein (Eds.), Sputtering by Particle Bombardment: Experiments and Computer Calculations from Threshold to MeV Energies, Springer, Berlin, 2007, pp. 33-187.

[26] P. Sigmund, Phys. Rev. 184 (2) (1969) 383.

[27] P. Sigmund, Thin Solid Films 520 (19) (2012) 6031.

[28] J. Neidhardt, S. Mráz, J.M. Schneider, E. Strub, W. Bohne, B. Liedke, W. Möller, C. Mitterer, J. Appl. Phys. 104 (6) (2008) 063304.

[29] Cf. www.srim.org for further information.

[30] F. Sanchette, T. Czerwiec, A. Billard, C. Frantz, Surf. Coat. Technol. 96 (2-3) (1997) 184.

[31] T. Ono, T. Kenmotsu, T. Muramoto, in: D. Depla, S. Mahieu (Eds.), Reactive Sputter Deposition, Springer, Berlin, 2008, pp. 1-42.

[32] D. Depla, S. Heirwegh, S. Mahieu, R. De Gryse, J. Phys. D: Appl. Phys. 40 (7) (2007) 1957.

[33] K.S. Fancey, Vacuum 46 (7) (1995) 695.

[34] D. Depla, W.P. Leroy, Thin Solid Films 520 (20) (2012) 6337.

[35] W.D. Westwood, J. Vac. Sci. Technol. 15 (1) (1978) 1.

[36] J.P. Biersack, S. Berg, C. Nender, Nucl. Instrum. Methods Phys. Res., Sect. B 59-60 (1) (1991) 21.

[37] H.C. Barshilia, N. Selvakumar, B. Deepthi, K.S. Rajam, Surf. Coat. Technol. 201 (6) (2006) 2193.

[38] ICDD International Center for Powder Diffraction Data, Powder Diffraction File (Card 03-065-2899 for fcc CrN, Card 00-038-1420 for fcc TiN, Card 00-025-1495 for fcc AlN, Card 00-025-1133 for hexagonal AlN, Card 00-051-0939 for hexagonal WC, Card 00-015-0806 for fcc Co, Card 00-032-1383 for fcc TiC), PDF-2/Release 2007.

[39] M.A. Lieberman, A.J. Lichtenberg, Principles of Plasma Discharges and Materials Processing, 2nd ed., Wiley, Hoboken, NJ, 2005.

[40] D.R. Lide, CRC Handbook of Chemistry and Physics, 85th ed., CRC Press, Boca Raton, FL, 2004.

[41] L. Chen, M. Moser, Y. Du, P.H. Mayrhofer, Thin Solid Films 517 (24) (2009) 6635.

[42] S. Khamseh, M. Nose, T. Kawabata, A. Saiki, K. Matsuda, K. Terayama, S. Ikeno, Mater. Trans. 49 (9) (2008) 2082.

[43] J. Lin, J.J. Moore, B. Mishra, M. Pinkas, W.D. Sproul, J.A. Rees, Surf. Coat. Technol. 202 (8) (2008) 1418.

[44] I.W. Park, D.S. Kang, J.J. Moore, S.C. Kwon, J.J. Rha, K.H. Kim, Surf. Coat. Technol. 201 (9-11) (2007) 5223.

[45] I. Petrov, P.B. Barna, L. Hultman, J.E. Greene, J. Vac. Sci. Technol. A 21 (5) (2003) S117.

[46] L. Hultman, W.D. Münz, J. Musil, S. Kadlec, I. Petrov, J.E. Greene, J. Vac. Sci. Technol. A 9 (3) (1991) 434.

[47] F. Adibi, I. Petrov, J.E. Greene, L. Hultman, J.E. Sundgren, J. Appl. Phys. 73 (12) (1993) 8580.

[48] I. Petrov, F. Adibi, J.E. Greene, L. Hultman, J.E. Sundgren, Appl. Phys. Lett. 63 (1) (1993) 36.

[49] S. Grasser, R. Daniel, C. Mitterer, Surf. Coat. Technol. 206 (22) (2012) 4666.

[50] G. Gottstein, Physikalische Grundlagen der Materialkunde, 2nd ed., Springer, Berlin, 2001.

[51] L. Rogström, J. Ullbrand, J. Almer, L. Hultman, B. Jansson, M. Odén, Thin Solid Films 520 (17) (2012) 5542.

[52] E.O. Hall, Proc. Phys. Soc. London Sect. B 64 (9) (1951) 747.

[53] N.J. Petch, J. Iron Steel Inst. 174 (1953) 25.

[54] A. Leyland, A. Matthews, Surf. Coat. Technol. 177-178 (2004) 317.

[55] A. Leyland, A. Matthews, Wear 246 (1-2) (2000) 1.

[56] T.L. Oberle, J. Met. 3 (1951) 438.

[57] D.S. Rickerby, P.J. Burnett, Thin Solid Films 157 (2) (1988) 195.

[58] Y. Pauleau, Vacuum 61 (2-4) (2001) 175.

[59] Q. Xia, H. Xia, A.L. Ruoff, J. Appl. Phys. 73 (12) (1993) 8198.

[60] P.H. Mayrhofer, A. Hörling, L. Karlsson, J. Sjölén, T. Larsson, C. Mitterer, L. Hultman, Appl. Phys. Lett. 83 (10) (2003) 2049.

[61] S.R. Pulugurtha, D.G. Bhat, M.H. Gordon, J. Shultz, M. Staia, S.V. Joshi, S. Govindarajan, Surf. Coat. Technol. 202 (4-7) (2007) 1160.

[62] N.P. Suh, H.C. Sin, Wear 69 (1) (1981) 91.

[63] K. Holmberg, A. Matthews, Coatings Tribology: Properties, Techniques and Applications in Surface Engineering, Elsevier, Amsterdam, 1994.

[64] A. Matthews, S. Franklin, K. Holmberg, J. Phys. D: Appl. Phys. 40 (18) (2007) 5463.